Decoupled Electrochemical CO_2 Reduction Using Redox Mediators

Mark Potter (MChem)

Department of Chemistry

This thesis is submitted in partial fulfilment of the requirements for the degree of Doctor of Philosophy

September 2025

Abstract

Climate change, caused by the use of fossil fuels for both primary energy and as a source of commodity chemicals, is of growing concern. It is imperative that alternate technologies are developed quickly to meet the internationally agreed emission reduction targets to limit global warming to 1.5 °C above pre-industrial levels. Electrolytic conversion of CO_2 and water for energy storage and chemical synthesis offers a potential solution to this issue, whereby renewable energy is used to drive the otherwise unfavourable reactions. Presently, conventional electrolysers rely on intricate membrane electrode assemblies which pose many chemical and mechanical challenges, resulting in low lifetime and limited activity. As an alternative technique, redox mediators can be used to decouple the chemical reaction from the electrode surface. Through this, charge transfer at the electrode and the electrocatalytic reaction occur effectively independently and can be optimised separately.

A range of redox active molecules were considered as possible mediators. Initially, a novel catalytic response to CO_2 was observed using a dithiolene complex of iron. This was explored further, where it was found that high selectivity towards formate could be achieved using trifluoroethanol as a proton source. Focus was then shifted to aqueous conditions more favourable for CO_2 reduction, where a complex of chromium with 1,3-propanediamine-N,N,N',N'-tetraacetic acid was selected due to its highly negative reduction potential. It was found that the two-electron reduction products CO and formate were both accessible by using optimised catalysts based on gold and bismuth nanomaterials respectively. A brief exploration of homogeneous co-catalysis using the mediator alongside Ni cyclam also found CO and formate to be the main products, with selectivity influenced by the supporting electrolyte. Finally, the reaction was scaled up, where it was found that production rates comparable to state-of-the-art systems are achievable.

Declaration of Authorship

I declare that this thesis has not been submitted in support of another degree at this or any other university and that all work presented is my own, unless specified with direct acknowledgement and reference to other individuals.

Chapter 3 presents work as published in *ChemElectroChem* under the title ‘Exploring the Electrochemistry of Iron Dithiolene and Its Potential for Electrochemical Homogeneous Carbon Dioxide Reduction’. The first author of this paper was Dr Craig Armstrong, and much of the work was completed alongside them as joint investigators. Any work not performed by the author of this thesis has been properly credited throughout the chapter.

Chapter 4 presents work as published in *EES catalysis* under the title ‘Electrochemically Decoupled Reduction of CO_2 to Formate Over a Dispersed Heterogeneous Bismuth Catalyst Enabled via Redox Mediators’. The author of this thesis was the primary investigator and first author of this paper.

Acknowledgements

First and foremost, I would like to offer my deepest thanks to my supervisor, Dr Kathryn Toghill, for her support and guidance throughout my PhD, and for fostering a collaborative and welcoming work environment.

I would also like to extend this thanks to the many fellow members of the research group I have had the pleasure of working with over the years, especially Dr Craig Armstrong for helping me jump straight into the project, and to Dr Luís Pinho and Dr Hamza Annath assistance with experimental work.

Additional thanks go to the technical staff for invaluable assistance in maintaining and providing access to a range of experimental facilities. In particular I would like to thank Dr Nathan Halcovitch for conducting X-ray experiments and assisting with elemental analysis, Dr Sara Baldock and Dr Elisabeth Shaw for providing assistance with SEM and TEM respectively.

The work undertaken was funded by the ERC Horizon 2020 research and innovation programme. All work was conducted at Lancaster University Chemistry Department.

I would also like to thank the Royce institute for generously providing access to their STEM at their Manchester Facility free of charge, and to Dr Matt Smith for providing technical support for the instrument.

Most importantly I would like to thank my family for supporting my choices throughout my education journey.

List of Acronyms and Chemical Abbreviations

Acronyms	Full Name
CO_2R	CO_2 Reduction
ECO_2R	Electrochemical CO_2 Reduction
$DECO_2R$	Decoupled Electrochemical CO_2 Reduction
DWE	Decoupled Water Electrolysis
HER	Hydrogen Evolution Reaction
OER	Oxygen Evolution Reaction
RFB	Redox Flow Battery
GDE	Gas Diffusion Electrode
SHE	Standard Hydrogen Electrode
RHE	Reversible Hydrogen Electrode
GC	Gas Chromatography

Abbreviation	Full Name
TFA	2,2,2-Trifluoroethanol
TEA	Triethanolamine
TiPa	Triisopropanolamine
PDTA	1,3-diaminopropane-N,N,N',N'-tetraacetic acid
DHP	Dihydroxyphenazine
DHPC	Dihydroxyphenazine Carboxylic Acid
TBA	Tetrabutyl Ammonium
PTFE	Poly tetrafluoroethene
PVA	Poly vinylalcohol
mnt	Maleonitriledithiolene

Table of Contents

Table of Figures

Chapter 1: Introduction

1.1 The big picture

Given current trends, global temperatures are expected to continue rising unless significant changes are made to the way we extract energy. This is due to the release of greenhouse gases, primarily carbon dioxide, which is causing a net positive radiative forcing effect by the accumulation of additional energy in the climate system.[1] This has already led to an increase in global average temperature estimated to be in the range of 0.8 °C to 1.3 °C. Downstream effects of this increase include raised sea level, and increased frequency and intensity of extreme weather events. As the world moves away from reliance on fossil fuels as a source of both energy and industrial feedstock, it is becoming increasing important to develop ways of both storing and transforming renewably generated energy.

As a stop-gap measure, a range of carbon sequestration techniques have been suggested. Large scale CO_2 emissions can be captured at the source, and stored geologically by injection into dry oil wells and coal seams, or chemically by mineral carbonation through the formation of carbonate rocks.[2] Carbon can also be sequestered biologically by encouraging photosynthetic processes such as mass reforestation. Ultimately however, the only way to truly close the carbon cycle is to develop carbon neutral processes for the production of all fuels and chemicals. The use of biofuels and biomass is an effective and well-established source of low carbon energy, but it lacks the scalability to fully replace fossil fuels. The only feasible way to close the carbon cycle is to develop efficient and industrially viable processes that utilise renewable energy and CO_2 as a feedstock.

To this end, a wide range of solutions have been proposed. Replacement energy carriers are of particular focus, with many suggested alternatives to petroleum-based fuels. In principle, hydrogen offers to be a promising alternative. It is the ultimate clean fuel, producing only water when oxidised. Despite having excellent gravimetric energy density as the lightest element, as a gas its volumetric energy density is poor. This is compounded by difficulty in storage and transport, resulting in a gravimetric energy density that is considerably lower in practice, where the storage medium makes up most of the mass. Molecules like ammonia and methanol have been suggested as potential hydrogen carriers, however these bring their own complications.

While eliminating carbon from our fuels is in principle a favourable solution to the problem of greenhouse gas emissions, the ubiquity of carbon as the foundation of the

materials on which society relies makes this impractical if not impossible. Hydrocarbons have become integral, from plastics and textiles to medicines and electronics, and while the practice of green synthesis aims to find alternative pathways, some compounds simply cannot be replaced on the necessary scale.

Hydrocarbons can be produced synthetically through gas-to-liquid technologies, such as the Fischer-Tropsch reaction, where a combination of carbon monoxide and hydrogen (syngas) is converted into saturated hydrocarbons.[3] Currently however, the process is primarily used by countries with limited access to crude oil-based petroleum, where the syngas used is sourced from steam methane reforming and coal gasification which emit considerable CO_2. Other processes include the Sabatier reaction in which methane is produced from CO_2 and H_2,[4] and the Mobil process in which methanol is converted to gasoline.[5]

With all this in mind, it is conceivable that the need for fossil fuels can be completely eliminated. To achieve this however, much needs to be changed in the way we extract and utilise energy.

1.2 Harnessing renewable energy

Renewable energy can be readily generated from a wide range of sources. The limitation of the vast majority of these, especially the most accessible ones, is that they are intermittent by nature. Energy needs to be stored during times of production such that it can then be used as needed. The sheer scale of this requirement presents significant technological challenges. Firstly, the timescale over which energy needs to be stored ranges from seconds to months. Secondly, the power output of this storage must be able to efficiently meet the needs ranging from a single lightbulb to an entire grid. Lastly, and most importantly, this storage must meet the required capacity to ensure energy can be supplied uninterrupted in the event that weather conditions do not allow for any to be produced. It is clear that no one solution can meet all of these needs, or would even be capable of meeting one of them, alone.

There already exists a range of widely utilised technologies including mechanical, thermal, chemical, and electrochemical systems. Of particular interest among these to a chemist are chemical and electrochemical systems. Both involve the storage of energy by using it to drive unfavourable chemical processes. Electrochemical energy storage is ubiquitous. Technologies range in scale from miniscule hearing aid batteries, to the rechargeable batteries that power portable devices, to grid scale systems capable of delivering the energy needs of entire cities. The chemistry is itself vast and varied in scope, but always relies on the controlled flow of electrons and ions. The most

widespread of these is the lithium-ion battery, however older technologies such as lead-acid, sodium-sulphur, and vanadium redox flow battery (RBF) also see success.[6]

As fossil fuels are also a source of chemical energy, this is the easiest to adapt to existing systems. Currently, only water electrolysis is commonly used as a method of chemical energy storage via hydrogen, however, due to the previously mentioned issues, it is not widespread. Other chemicals, especially hydrocarbons, are much less accessible via electrolysis. In principle, CO_2 can be electrochemically reduced to a selection of small hydrocarbons ranging from C_1 to C_3. From a thermodynamic perspective, these reactions shouldn't require much more energy than that needed to reduce water to hydrogen. Unfortunately, despite intense research effort over the last 40 years, no industrially viable technique has been developed.

1.3 Electrochemical CO_2 Reduction

To enable electrochemical CO_2 reduction (ECO_2R), there are considerable hurdles which must be overcome. While it is true that when only considering the Gibbs free energy required for the hydrocarbon products, they do not require much more energy than water splitting, they must first pass through an intermediate that requires the breaking of the incredibly strong carbon to oxygen double bond(s). The stability of these bonds, and thus the energy released upon their formation, are what gives hydrocarbons their excellent energy density as fuels, but it also makes it incredibly difficult to reverse the reaction. As shown in Table 1, the initial insertion of an electron into the CO_2 molecule to form a radical, even thermodynamically, requires considerable energy, reflected in a minimum applied potential −1.9 V vs the standard hydrogen electrode (SHE).

Table 1.1 *List of half-cell reactions for the electrochemical reduction of CO_2 with standard potentials calculated from the Gibbs free energy.[7] Adapted to high and low pH using the Nernst equation assuming a first order dependence on $[H^+]$.*

Half-Reaction	**Electrode Potential (V vs SHE)**		
	pH 0	**pH 7**	**pH14**
CO_2 (g) + e^- → *COO^-	-	-1.9	-
CO_2 (g) + 2H^+ + 2e− → HCOOH (l)	-0.197	-0.61	-
CO_2 (g) + H_2O (l) + 2e^- → $HCOO^-$ (aq) + OH^-	-	-0.43	-0.843
CO_2 (g) + 2H^+ + 2e^- → CO (g) + H_2O (l)	-0.117	-0.53	-
CO_2 (g) + H_2O (l) + 2e^- → CO (g) + 2OH^-	-	-0.52	-0.933
CO_2 (g) + 4H^+ + 2e^- → HCHO (l) + H_2O (l)	-0.067	-0.48	-
CO_2 (g) + 3H_2O (l) + 4e^- → HCHO (l) + 4OH^-	-	-0.89	-1.303

CO_2 (g) + $6H^+$ (l) + $6e^-$ → CH_3OH (l) + H_2O (l)	0.033	-0.38	-
CO_2 (g) + $5H_2O$ (l) + $6e^-$ → CH_3OH (l) + $6OH^-$	-	-0.81	-1.223
CO_2 (g) + $8H^+$ + $8e^-$ → CH_4 (g) + $2H_2O$ (l)	0.173	-0.24	-
CO_2 (g) + $6H_2O$ (l) + $8e^-$ → CH_4 (g) + $8OH^-$	-	-0.25	-0.663
$2CO_2$ (g) + $12H^+$ + $12e^-$ → C_2H_4 (g) + $4H_2O$ (l)	0.473	0.06	-
$2CO_2$ (g) + $8H_2O$ (l) + $12e^-$ → C_2H_4 (g) + $12OH^-$	-	-0.34	-0.753
$2CO_2$ (g) + $12H^+$ + $12e^-$ → CH_3CH_2OH (l) + $3H_2O$ (l)	0.493	0.08	-
$2CO_2$ (g) + $9H_2O$ (l) + $12e^-$ → CH_3CH_2OH (l) + $12OH^-$ (l)	-	-0.33	-0.743
$2H^+$ + $2e^-$ → H_2	0	-0.414	-
$2H_2O$ + $2e^-$ → H_2 + $2OH^-$	-		-0.829

Catalysts can be used to stabilise, or even avoid the need entirely for this radical intermediate state. Of the possible products, the 2-electron reductions to either formic acid/formate and carbon monoxide are the most accessible, and are the most commonly reported. It can be expected that all further reduced products will require the same initial intermediate(s), and thus ultimately require a similar applied potential to produce despite the thermodynamics appearing to favour them.

A catalyst is an agent that improves the rate of a given reaction without being consumed in the process. It lowers the activation energy barrier for a reaction by offering an alternate pathway through lower energy intermediates. In electrocatalysis, this is manifested as a reduction in overpotential requirements for a reaction at a given current density. The overpotential is the difference between the theoretical thermodynamic potential for a reaction and the experimental onset potential of said reaction. The catalyst may also be selective to a single product by lowering the energy requirement for only a specific reaction pathway. An electrocatalyst typically works in one of two ways, inner sphere (coordinating) or outer sphere (non-coordinating) electron transfer, and the catalyst may either be heterogeneous or homogeneous in nature.

Outer sphere transfer describes a simple electron transfer process between the catalyst and the reactant without the formation of a bond between them. In this way, the catalyst is only involved in the initial activation of the reaction pathway and exists only as a source of electrons. It is not directly involved in any of the ensuing reaction intermediates, and subsequently catalysts that work this way tend to have little influence on reaction selectivity. By contrast, inner sphere electron transfer proceeds via the formation of a reduced adduct that is coordinated to the catalyst. The catalyst

remains a key part of the reaction pathway after electron transfer and is directly involved in reaction intermediates. In doing so, it is able to influence selectivity by lowering the activation energy for a specific pathway, leading to the formation of a single product.

Broadly, CO_2R catalysts can be arranged into two categories, those that favour formate, and those that favour CO. The outlier to this is copper, which is the only material that reliably produces further reduced products. This is generally explained by how CO_2 interacts with the catalysts as mentioned in the preceding paragraphs.[8] Outer sphere favours formate, whereas inner sphere favours CO, and is also necessary for the further reduced products. In the outer sphere reaction pathway, the first reduction intermediate is stabilised by interactions between the catalyst and oxygen atoms of the reduced CO_2 molecule. This is followed by proton abstraction from the surrounding water and further reduction to formate. For the inner sphere pathway, the first reduction intermediate is stabilised through coordination between the carbon and the catalyst surface. This stops the immediate formation of a carbon-hydrogen bond and allows for carbon monoxide to be produced. If the carbon monoxide remains bound to the catalyst, it can be activated towards further reduction.

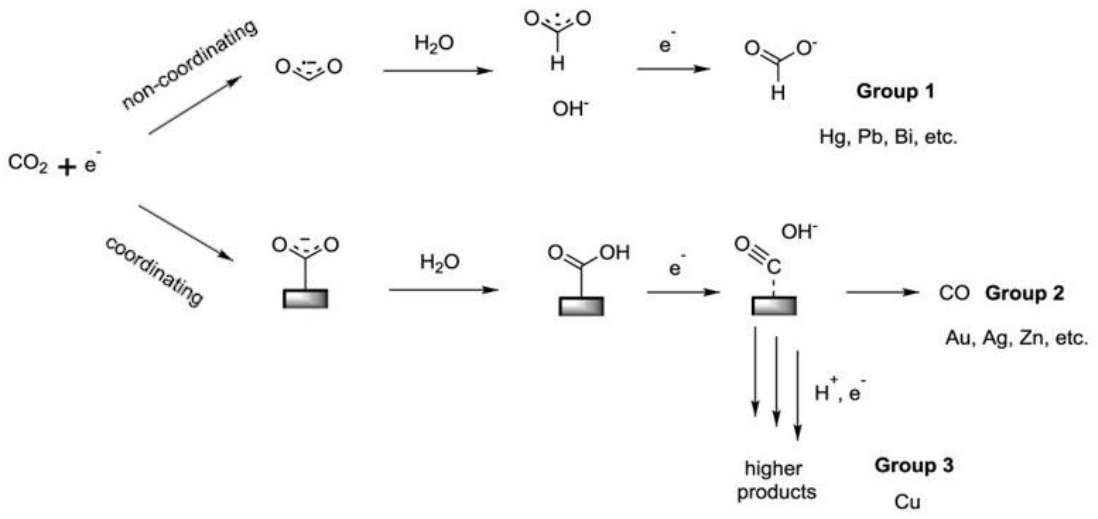

Figure 1.1 *Simplified mechanistic pathways for the electrochemical reduction of CO_2 catalysed by metal electrodes.*[8]

This simplified view is sufficient to explain the observed selectivity of most catalysts without considering individual mechanisms. Many detailed studies have been performed to further elucidate the key intermediates in the formation of different products in the hope of developing highly active and selective catalysts.[9,10] Reviews

discussing ECO_2R towards a variety of products are frequently published,[11–15] especially with regards to copper and the range of further reduced products it enables.[16–18]

1.4 Cell Designs for CO_2R

Beyond the chemistry, there are also significant engineering limitations which further confound the issue. Cell design plays a crucial role in the transport of reactants to the electrodes. The delivery of CO_2 to the electrode surface is typically the most limiting factor in ECO_2R.

The classic two-compartment or 'H-cell' design of the electrochemical cell remains the most widely used in the reporting of new catalyst materials due to its relative simplicity. Each electrode has its own electrolyte reservoir, separated by a salt bridge which allows for the transport of ions between the electrolytes.[19,20] These systems are commonly reported in both stationary and flow configurations, and can operate both closed or open. As an alternative, the three- or four-compartment gas diffusion cell makes use of electrode(s) at the intersection of two compartments, one containing an electrolyte and the other containing a gas.[21–24] This cell is typically only operated in flow to take maximum advantage of the improvements in mass transport.

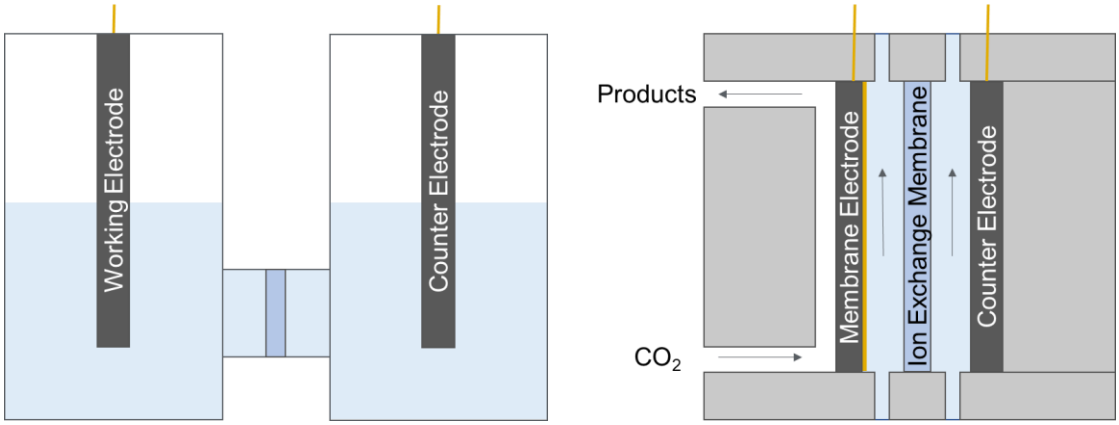

Figure 1.2 *(left) Schematic of a typical H-cell with stationary electrolyte. (right) Schematic of a three-compartment gas diffusion electrode flow cell. Both cell configurations can be modified by the addition of a reference electrode in the working electrode compartment.*

In both systems, the electrode-catalyst is typically deployed as a two-dimensional surface exposed to the electrolyte, immediately facing an ion conducting membrane, opposite to the counter electrode. This is done with the intention of minimising resistance, of which even a small amount can rapidly increase the voltage that must be applied to allow for increased current, lowering the energy efficiency of the system.

1.5 Decoupled Reactions

An emerging strategy in electrochemistry is the idea of decoupled systems. In principle, this is done by adding a reversible redox couple as an intermediate, such that the half-cell reactions for the oxidation and reduction products are no longer intrinsically linked. This can be used to separate the processes spatially and/or temporally by acting as charge transport and/or buffering. Some possible benefits of this include reducing the risk of product crossover, decreasing the operating potential of the cell, or improving resilience in the face of intermittent renewable energy.

The most basic interpretation of this is molecular/homogeneous electrocatalysis, where the electron transfer from electrode to product is mediated directly by the redox active catalyst. While this is a form of mediated catalysis, it does not truly fit the description of the decoupled system, as the rate of product formation is still intrinsically connected to the counter cell half-reaction, and the electroactive material is acting as the catalyst. However, it can be expanded further with the addition of a redox mediator, a second redox active species that is not a catalyst, only taking part in the transfer of charge from the electrode to the molecular catalyst.[25] With this, the system can now be described as truly decoupled. This additional redox active species can act as both a charge transport mechanism, such that the molecular catalyst has access to charge outside the double layer at the electrode surface, and also as a charge buffer if used at concentrations much greater than the catalyst itself, such that the extra potential required for a given current increase would be less. This buffer would still have a finite capacity, but would allow for the system to be more resilient towards intermittent power.

While the research area is still emerging, it takes a lot of inspiration from biological systems where enzymes and co-factors perform similar reactions using electron cascades and proton-coupled mediators. Unsurprisingly, this was applied successfully to the reduction of CO_2 by iron porphyrin derivatives, which themselves are similar to the reaction centres found in many enzymes.[26] Using a proton coupled redox mediator inspired by the ubiquitous biological cofactor nicotinamide adenine dinucleotide, a 13-fold increase in rate was achieved without altering the selectivity of the catalyst. Design of the redox mediator played a crucial role in this instance. Beyond simply matching the reduction potential of the catalyst, the mediator's structure can be optimised to facilitate the transition state.

The redox mediator does not need to be proton coupled to enhance the rate of reaction however. Another example is the use of aromatic sulphone derivatives to improve the performance of a chromium centred catalyst.[27,28] Further, the presence of this redox

mediator opened an additional reaction pathway such that CO_2R was now possible without the need for a proton source, instead resulting in the disproportionation of CO_2 to CO and CO_3^{2-}.

Redox mediators can also be used alongside heterogeneous catalysts in two main ways. The first of these is solely as a charge storage buffer, whereby the two half-cell reactions of a process such as water electrolysis are separated into two steps, each mediated by the reversible redox species. In this case, the hydrogen evolution reaction (HER) and oxygen evolution reaction (OER) no-longer occur simultaneously. Instead, the electrolyser will alternate between the two reactions, coupled to either oxidation or reduction of the mediator respectively. As only one product is being formed at any given time, the purity of the gas stream is very high, with no risk of crossover of incompatible products. Further, the redox potential of the mediator can be positioned such that the potential requirement at any given time is lower, or such that one of the reactions will occur spontaneously without the need for a driving potential at all. This has been achieved using a variety of mediators such as polyoxometalates,[29–31] polysulphides,[32] and metal oxyhydroxides.[33–35] In this case, the HER and OER are still occurring on the electrode surface.

Alternately, the redox mediator can instead be used to shuttle charge (and possibly protons) between an electrode and a catalyst. Rather than switching between HER and OER modes, we now have a series of coupled half-cell reactions operating simultaneously. This is in essence the truest combination of flow batteries and chemical synthesis. Mediators are used to drive one of or both HER and OER through spontaneous processes when they are introduced to suitable catalysts. Successful examples of this include adaption of a vanadium-cerium RFB[36], a vanadium-manganese RFB,[37] and a phenazine-iron RFB.[38]

In both cases, the relative simplicity of water electrolysis has allowed for a wide range of chemistries to be employed. Systems making use of both acidic and basic environments have been explored, and a range of mediators and catalysts have been used without worry of competing reactions. To date however, neither of these designs have been extended beyond water electrolysis. While the previously discussed molecular catalyst approach enabled high selectivity due to the specificity of the mechanisms, as well as the non-aqueous environment eliminating competition from HER, attempting CO_2R on conventional heterogeneous catalysts using redox mediators invokes many complications.

1.6 Decoupled Water Electrolysis

While still an emerging technique, a series of recent reviews have highlighted the rapid growth of the field, as displayed in Figure 1.3.[39–43] As mentioned, contemporary systems for decoupled water electrolysis (DWE) can broadly be categorised into two main types based on whether the mediator is used to decouple HER and OER temporally or spatially. Further distinction can be made based on whether the mediator is solid or electrolyte-borne, and whether the process is solely electrochemical or follows an electrochemical-chemical cycle.

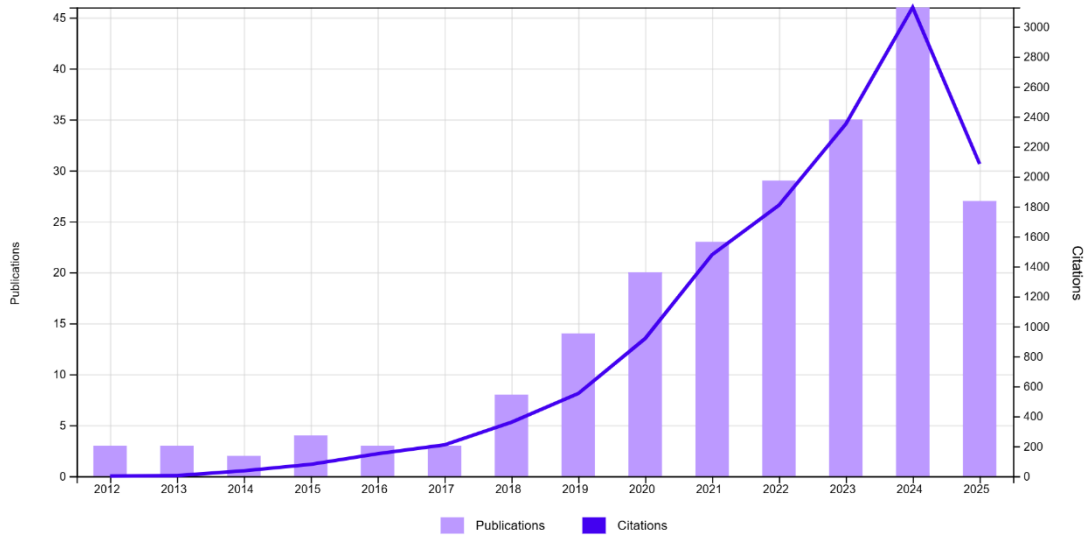

Figure 1.3 *Graph of publications and citations by year for the search terms 'decoupled water electrolysis' on Web of Science™.*

The seminal paper on DWE, published in 2013 by Symes and Cronin, reported the first instance of temporally separated DWE.[29] Utilising the polyoxometalate phosphomolybdic acid ($H_3PMo_{12}O_{40}$) in a phosphoric acid electrolyte as a proton-coupled charge buffer, HER and OER were separated into two distinct steps. Initially, water was oxidised at the working electrode (defined as the electrode at which either OER or HER is occurring depending on whether current is positive or negative respectively) and the mediator was reduced at the counter electrode. Reduction of the mediator is coupled with protonation, balancing the pH of the solution with protons released from the oxidation of water. Upon switching the direction of the current, proton reduction is now occurring at the working electrode and the mediator is oxidised at the counter electrode. Again, pH is maintained as protons are released by the oxidised mediator.

Decoupling the process in this way has two main benefits as compared to conventional electrolysis. The first is that because H_2 and O_2 are produced in sequence rather than simultaneously, product purity is much higher and the risk of product crossover is eliminated. Secondly, because the half reactions for HER and OER are decoupled from each other (and instead tied to the redox potential of the mediator) the cell potential required for a given rate of production will be less than for direct water electrolysis. For example, the phosphomolybdic acid mediated system performed water oxidation at a rate 100 mA cm^{-2} with a potential of 1.71 V, and performed proton reduction at the same rate with a potential of 1.23 V. To achieve the same rate of water splitting directly, a potential of 2.55 V was required. While less energy was needed at any given time, the overall potential of DWE was higher at 1.71 + 1.23 = 2.94 V. This was expanded to other polyoxometalates such as silicotungstic acid,[44] as well as polysulphides,[32] and quinones.[45]

While the mediators discussed thus far have been electrolyte borne, it is also possible to use a solid redox mediator for purely electrochemical, temporally decoupled DWE. The first example of such as system utilised nickel hydroxide as a mediator.[34,35] Initially, HER occurs at the working electrode, while a nickel hydroxide counter electrode is oxidised to nickel oxyhydroxide. When the direction of current is switched, OER occurs on the working electrode and the nickel oxyhydroxide is converted back to nickel hydroxide. Compared to systems where the mediator is electrolyte borne, this has the added advantage of not requiring an ion conductive membrane to separate the electrodes, which are typically expensive, delicate and add considerable resistance to the cell, as there is no opportunity for the solid mediator to interact with the working electrode where the redox process could short-circuit. The system is however limited by the redox mediator capacity being dependent on electrode area rather than electrolyte concentration and volume. The energy efficiency of the system was again found to be slightly worse than direct water electrolysis at the same rate, requiring cell potentials of 1.6 V to drive HER and 0.4 V to drive OER respectively, for a total of 2.0 V compared to the 1.83 V required for direct water electrolysis.

Simultaneously, the concept of spatially separated DWE was being developed by the Girault group, first publishing in 2014.[36] Here, spatial decoupling was achieved using a pair of mediators with redox potentials situated negative of HER on one side and positive of OER on the other. The mediators, vanadium on the negative side and cerium on the positive side, were charged during an electrochemical step then discharged chemically over electrocatalytic material. The vanadium(II)/(III) couple has a redox potential of −0.26 V vs SHE and high solubility in the sulphuric acid electrolyte.

When exposed to HER catalysts such as platinum and molybdenum carbide (Mo_2C), vanadium(II) is spontaneously oxidised to vanadium(III) and hydrogen is evolved at the catalyst surface. The cerium(III)/(IV) couple has a redox potential of 1.48 V vs SHE, providing a small overpotential for OER, allowing it to spontaneously react with a ruthenium oxide catalyst to evolve oxygen. Compared to temporally decoupled DWE, this has the added advantage of being able to act as both a conventional redox flow battery and as an electrolyser, creating a flexible system to store, release and transform the intermittent energy provided by renewables.

The initial design was limited by the poor performance of the cerium redox couple, resulting in a cell with low voltage efficiency. Formally, the pair of redox couples should create a cell with a potential of 1.7 V. However, respective charge and discharge potentials of 2.5 and 0.7 V resulted in a round trip efficiency of just 28%. Energy efficiency towards water splitting was better, at 49%, however this was still quite poor compared to conventional systems. Replacing the cerium with the much more favourable Mn(II)/(III) couple improved efficiency considerably, up to 66%.[37] The spatial decoupling of HER and OER in this manner allows for the collection of highly pure products, as there is no risk of crossover when products are evolved in separate catalyst beds. A range of systems where either one or both reactions are decoupled into separate electrochemical and chemical steps have been reported, including the use of polyoxometalates for HER,[46–49] iron triethanolamine for HER,[50] bromide-bromate for OER,[51] and a combined system of dihydroxyphenazines and ferri/ferrocyanide for both HER and OER respectively.[38]

Beyond this, spatial decoupling can also be achieved by operating separate HER and OER cells both coupled to a single redox mediator. In one cell, HER occurs and the mediator is oxidised, while in the other OER occurs and the mediator is reduced. The mediator can either be pumped between the two cells, or the cells can be connected electrically so the mediator oxidation state can equilibrate. A series of mediators have been reported for DWE of this style, such as ferri/ferrocyanide,[52] quinones,[53,54] and polyoxometalates.[55]

The efficiency of such processes can be understood by considering the redox potentials of all the steps involved. Generally, the purely electrochemical, temporally decoupled design can be considered more efficient because the overall cell voltage is still defined by the potentials of HER and OER (Figure 1.4A). This is compared the electrochemical-chemical system, where the cell voltage is defined by the redox potentials of the mediators (Figure 1.4B), which must be positioned above and below

OER and HER respectively to provide a thermodynamic driving force for the chemical step. However, due to the way it is designed, the purely electrochemical system requires two separate cell reactions. Kinetic losses in the form of overpotential are unavoidable at practical current densities, and each electrochemical process will contribute an overpotential to the overall voltage. The overall voltage of purely electrochemical, temporally decoupled DWE thus has four overpotential contributions.

$$E_{cell\ HER} = E_{med\ ox} - E_{HER} + \eta_{med\ ox} + \eta_{HER}$$

$$E_{cell\ OER} = E_{OER} - E_{med\ red} + \eta_{med\ red} + \eta_{OER}$$

$$E_{DWE} = E_{cell\ HER} + E_{cell\ OER}$$

Conversely, the electrochemical-chemical system only has a single cell, and its voltage is determined by the redox potentials of the two mediators and the overpotential for their respective reduction and oxidation.

$$E_{DWE} = E_{cell} = E_{med\ OER\ ox} - E_{med\ HER\ red} + \eta_{med\ OER\ ox} + \eta_{med\ HER\ red}$$

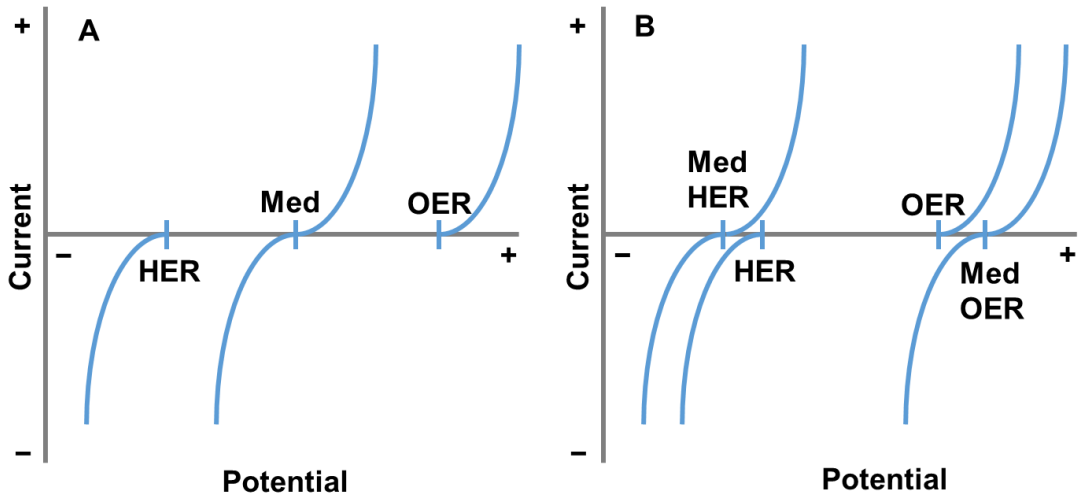

Figure 1.4 *Graphs of the relative redox potentials for HER, OER and mediator in a DWE process for systems with (A) purely electrochemical steps and a (B) sequential electrochemical-chemical steps.*

1.7 Is Decoupled ECO_2R Feasible?

Over the course of this work, many factors were considered while selecting suitable mediators and catalysts for decoupled electrochemical CO_2 reduction ($DECO_2R$), finding a compatible pairing is crucial. When developing DWE, a range of

commercialised catalyst materials are available suitable for any desired pH. Choosing a catalyst for DECO_2R on the other hand is much less obvious.

The operating pH of the mediator is often crucial to its stability, solubility, and electrochemical properties such as redox potentials and reversibility. It also plays a role in CO_2 solubility. Basic conditions would trap dissolved CO_2 as carbonate, while acidic conditions would limit its solubility and facilitate HER. For this reason, it is preferable to use a neutral to mildly basic pH in the range of 7-9. Unfortunately, RFB electrolytes typically work best at one extreme or the other, with only limited examples around neutral pH.

Non-aqueous ECO_2R is often very poor in terms of energy efficiency requiring a large overpotential, while using water as the solvent limits the potential window and invites competition from HER by direct reduction of the solvent at the electrode. Indeed, the small solvent window of water remains a major concern to all CO_2R catalysts despite its popularity as a medium. As summarised in Table 1. 2, typical operating potentials for CO_2R catalysts are more negative than the onset of hydrogen evolution at around −0.8 V vs RHE observed on the carbon electrode materials used in RFBs and electrolysers. Clearly, finding catalyst materials with minimal overpotential will be key in enabling DECO_2R. As such, each chapter begin with a brief review of the class of CO_2R catalyst on which it focuses.

Table 1.2 *Sample of CO_2R catalysts reported by Hori, indicating electrode potential required to pass a current of 5.0 mA cm^{-2} in aqueous 0.1 M $KHCO_3$ electrolyte.*[56]

Metal Catalyst	Potential vs RHE / V	Major Product(s)
Gold	−0.65	CO
Silver	−0.98	CO
Tin	−1.09	HCOOH
Lead	−1.24	HCOOH
Copper	−1.05	CH_4, C_2H_4

1.8 Thesis Aims and Overview

The overarching goal of this work is to determine whether it is feasible to electrochemically decouple the reduction of CO_2 to high value products, through the use of redox mediators as charge transfer vectors.

Chapter 2

This chapter details the electrochemical theory underlying the work completed herein, along with an overview of many of the experimental techniques utilised. Experimental design is explained along with justification of design choices. A detailed description of how products were accurately quantified including how equipment was calibrated is also included.

Chapter 3

In this experimental chapter, the electrochemical behaviour of the complex of Fe with maleonitriledithiolate was explored. A detailed study of the electrochemical response is characterised by cyclic voltammetry under various reaction conditions, exploring the novel homogeneous catalytic reaction with dissolved CO_2 following 2 one-electron reduction steps. The products of this reduction under various conditions were quantified following bulk electrolysis reactions, and the catalytic turnover was estimated from analysis of the cyclic voltammogram. A series of mechanisms for the observed products are discussed following density functional theory modelling. This work was published as part of an article in the journal *ChemElectroChem* in 2022.[57]

Chapter 4

This chapter begins by exploring potential molecules to act as redox mediators for decoupled electrochemical CO_2R. Having found a standout molecule (Cr PDTA), an initial screening of simple metal powders as heterogenous electrocatalysts was performed to determine which CO_2R products can be produced. It was found that formate was the only readily accessible CO_2R product, only when utilising bismuth metal. Selectivity was enhanced by synthesising bismuth nanomaterials with defined size and shape. This work was published as part of an article in the journal *EES Catalysis* in 2024.[58]

Chapter 5

Building on the work in Chapter 4 using Cr PDTA as a redox mediator, catalyst scope was extended with the intention of producing a gaseous product. Gold nanomaterials were utilised to successfully produce CO as a major product. The amount of polymer

capping agent was varied, resulting in the production of a series of CO/H_2 gas mixtures. The mediator concentration was scaled up to allow for long duration experiments where the formation of reduction products was measured continuously via online gas analysis.

Chapter 6

Returning to themes of homogeneous catalysis described in Chapter 3, the Cr PDTA mediator was utilised alongside a nickel cyclam catalyst, resulting in almost exclusive selectivity towards the CO_2R products CO and HCOO(H) with minimal contribution of HER. A brief study on the effect of the supporting electrolytes KCl and $KHCO_3$ was conducted.

Chapter 7

This final chapter presents conclusions on the work completed herein and describes the future work which would build upon it. Key results are summarised and their significance with regard to the greater research area are discussed.

1.9 References

1 IPCC, *Summary for Policymakers. In: Climate Change 2021: The Physical Science Basis. Contribution of Working Group I to the Sixth Assessment Report of the Intergovernmental Panel on Climate Change*, Cambridge University Press, 2021.

2 R. Lal, *Philos. Trans. R. Soc. B Biol. Sci.*, 2008, **363**, 815–830.

3 R. B. Anderson, *Fischer-Tropsch synthesis*, 1984.

4 C. Vogt, M. Monai, G. J. Kramer and B. M. Weckhuysen, *Nat. Catal.*, 2019, **2**, 188–197.

5 F. J. Keil, *Microporous Mesoporous Mater.*, 1999, **29**, 49–66.

6 X. Fan, B. Liu, J. Liu, J. Ding, X. Han, Y. Deng, X. Lv, Y. Xie, B. Chen, W. Hu and C. Zhong, *Trans. Tianjin Univ.*, 2020, **26**, 92–103.

7 W. Zhang, Y. Hu, L. Ma, G. Zhu, Y. Wang, X. Xue, R. Chen, S. Yang and Z. Jin, *Adv. Sci.*, 2017, 170275.

8 J. P. Jones, G. K. S. Prakash and G. A. Olah, *Isr. J. Chem.*, 2014, **54**, 1451–1466.

9 J. T. Feaster, C. Shi, E. R. Cave, T. Hatsukade, D. N. Abram, K. P. Kuhl, C. Hahn, J. K. Nørskov and T. F. Jaramillo, *ACS Catal.*, 2017, **7**, 4822–4827.

10 A. Bagger, W. Ju, A. S. Varela, P. Strasser and J. Rossmeisl, *ChemPhysChem*, 2017, **18**, 3266–3273.

11 S. Zhao, R. Jin and R. Jin, *ACS Energy Lett.*, 2018, **3**, 452–462.

12 F. Y. Gao, R. C. Bao, M. R. Gao and S. H. Yu, *J. Mater. Chem. A*, 2020, **8**, 15458–15478.

13 X. Du Liang, N. Tian, S. N. Hu, Z. Y. Zhou and S. G. Sun, *Mater. Reports Energy*, 2023, **3**, 100191.

14 S. Zhao, S. Li, T. Guo, S. Zhang, J. Wang, Y. Wu and Y. Chen, *Nano-Micro Lett.*, 2019, **11**, 1–19.

15 X. Li, X. Wu, X. Lv, J. Wang and H. Bin Wu, *Chem Catal.*, 2022, **2**, 262–291.

16 S. Nitopi, E. Bertheussen, S. B. Scott, X. Liu, A. K. Engstfeld, S. Horch, B. Seger, I. E. L. Stephens, K. Chan, C. Hahn, J. K. Nørskov, T. F. Jaramillo and I. Chorkendorff, *Chem. Rev.*, 2019, **119**, 7610–7672.

17 Y. Hori, I. Takahashi, O. Koga and N. Hoshi, *J. Mol. Catal. A Chem.*, 2003, **199**, 39–47.

18 J. Yu, J. Wang, Y. Ma, J. Zhou, Y. Wang, P. Lu, J. Yin, R. Ye, Z. Zhu and Z. Fan, *Adv. Funct. Mater.*, 2021, **31**, 1–28.

19 R. A. Tufa, D. Chanda, M. Ma, D. Aili, T. B. Demissie, J. Vaes, Q. Li, S. Liu and D. Pant, *Appl. Energy*, 2020, **277**, 115557.

20 C. Ampelli, F. Tavella, D. Giusi, A. M. Ronsisvalle, S. Perathoner and G. Centi, *Catal. Today*, 2023, **421**, 114217.

21 D. Higgins, C. Hahn, C. Xiang, T. F. Jaramillo and A. Z. Weber, *ACS Energy Lett.*, 2019, **4**, 317–324.

22 H. Rabiee, L. Ge, X. Zhang, S. Hu, M. Li and Z. Yuan, *Energy Environ. Sci.*, 2021, **14**, 1959–2008.

23 E. W. Lees, B. A. W. Mowbray, F. G. L. Parlane and C. P. Berlinguette, *Nat. Rev. Mater.*, 2022, **7**, 55–64.

24 T. N. Nguyen and C. T. Dinh, *Chem. Soc. Rev.*, 2020, **49**, 7488–7504.

25 A. G. Reid and C. W. Machan, *J. Am. Chem. Soc.*, 2023, **145**, 2013–2027.

26 P. T. Smith, S. Weng and C. J. Chang, *Inorg. Chem.*, 2020, **59**, 9270–9278.

27 S. L. Hooe, J. J. Moreno, A. G. Reid, E. N. Cook and C. W. Machan, *Angew. Chemie - Int. Ed.*, 2022, **61**, e202109645.

28 A. G. Reid, J. J. Moreno, S. L. Hooe, K. R. Baugh, I. H. Thomas, D. A. Dickie and C. W. Machan, *Chem. Sci.*, 2022, **13**, 9595–9606.

29 M. D. Symes and L. Cronin, *Nat. Chem.*, 2013, **5**, 403–409.

30 J.-J. Chen, M. D. Symes and L. Cronin, *Nat. Chem.*, 2018, **10**, 1042–1047.

31 J. Lei, J. J. Yang, T. Liu, R. M. Yuan, D. R. Deng, M. Sen Zheng, J. J. Chen, L. Cronin and Q. F. Dong, *Chem. - A Eur. J.*, 2019, **25**, 11432–11436.

32 M. Zhang, J. Guan, Y. Tu, S. Wang and D. Deng, *Innovation(China)*, 2021, **2**, 100144.

33 R. Palumbo, R. B. Diver, C. Larson, E. N. Coker, J. E. Miller, J. Guertin, J. Schoer, M. Meyer and N. P. Siegel, *Chem. Eng. Sci.*, 2012, **84**, 372–380.

34 L. Chen, X. Dong, Y. Wang and Y. Xia, *Nat. Commun.*, 2016, **7**, 11741.

35 J. Wei, Y. Shao, J. Xu, F. Yin, Z. Li, H. Qian, Y. Wei, L. Chang, Y. Han, J. Li and L. Gan, *Nat. Commun.*, 2024, **15**, 9012.

36 V. Amstutz, K. E. Toghill, F. Powlesland, H. Vrubel, C. Comninellis, X. Hu and H. H. Girault, *Energy Environ. Sci.*, 2014, **7**, 2350–2358.

37 D. Reynard and H. Girault, *Cell Reports Phys. Sci.*, 2021, **2**, 100556.

38 F. Zhang, H. Zhang, M. Salla, N. Qin, M. Gao, Y. Ji, S. Huang, S. Wu, R. Zhang, Z. Lu and Q. Wang, *J. Am. Chem. Soc.*, 2021, **143**, 223–231.

39 P. J. McHugh, A. D. Stergiou and M. D. Symes, *Adv. Energy Mater.*, 2020, **10**, 2002453.

40 A. Paul and M. D. Symes, *Curr. Opin. Green Sustain. Chem.*, 2021, **29**, 100453.

41 Z. P. Ifkovits, J. M. Evans, M. C. Meier, K. M. Papadantonakis and N. S. Lewis, *Energy Environ. Sci.*, 2021, **14**, 4740–4759.

42 K. Zhou, J. Huang, D. Xiang, A. Deng, J. Du and H. Liu, *J. Energy Chem.*, 2024, **94**, 340–356.

43 G. Ruan, F. Todman, G. Yogev, R. Arad, T. Smolinka, J. O. Jensen, M. D. Symes and A. Rothschild, *Nat. Rev. Clean Technol.*, 2025, **1**, 380–395.

44 G. Chisholm, L. Cronin and M. D. Symes, *Electrochim. Acta*, 2020, **331**, 135255.

45 B. Rausch, M. D. Symes and L. Cronin, *J. Am. Chem. Soc.*, 2013, **135**, 13656–13659.

46 W. Wu, X. Y. Wu, S. S. Wang and C. Z. Lu, *J. Catal.*, 2019, **378**, 376–381.

47 L. MacDonald, J. C. McGlynn, N. Irvine, I. Alshibane, L. G. Bloor, B. Rausch, J. S. J. Hargreaves and L. Cronin, *Sustain. Energy Fuels*, 2017, **1**, 1782–1787.

48 J. Lei, J. J. Yang, T. Liu, R. M. Yuan, D. R. Deng, M. Sen Zheng, J. J. Chen, L. Cronin and Q. F. Dong, *Chem. - A Eur. J.*, 2019, **25**, 11432–11436.

49 B. Rausch, M. D. Symes, G. Chisholm and L. Cronin, *Science (80-.).*, 2014, **345**, 1326–1330.

50 Y. Ji, F. Zhang, M. Zhou, J. Yu and Q. Wang, *Int. J. Hydrogen Energy*, 2020, **45**, 18888–18894.

51 I. Slobodkin, E. Davydova, M. Sananis, A. Breytus and A. Rothschild, *Nat.*

Mater., 2024, **23**, 398–405.

52 S. Goodwin and D. A. Walsh, *ACS Appl. Mater. Interfaces*, 2017, **9**, 23654–23661.

53 N. Kirkaldy, G. Chisholm, J. J. Chen and L. Cronin, *Chem. Sci.*, 2018, **9**, 1621–1626.

54 F. Wang, H. Sheng, W. Li, J. B. Gerken, S. Jin and S. S. Stahl, *ACS Energy Lett.*, 2021, **6**, 1533–1539.

55 O. Mbang Eze, Z. Ertekin and M. D. Symes, *Energy and Fuels*, 2025, **39**, 7129–7136.

56 Y. Hori, *Mod. Asp. Electrochem.*, 2008, 89–189.

57 C. G. Armstrong, M. Potter, T. Malcomson, R. W. Hogue, S. M. Armstrong, A. Kerridge and K. E. Toghill, *ChemElectroChem*, 2022, **9**, e202200610.

58 M. Potter, D. E. Smith, C. G. Armstrong and K. E. Toghill, *EES Catal.*, 2024, **2**, 379–388.

Chapter 2: Experimental Techniques and Method Development

2.1 Electrochemical principles

Electrochemistry, as a branch of physical chemistry, concerns chemical changes as a result of charge transfer, typically at a polarised interface. If this process occurs spontaneously it is referred to as being galvanic, where chemical energy is converted to electrical energy allowing work to be extracted from the system. If this process is not spontaneous, it is referred to as being electrolytic and requires external work in the form of electrical energy to occur.[1] Every electrochemical process can be split into two effectively independent half reactions, in principle allowing any two half-reactions to be combined into a functioning cell. Each half-reaction occurs at its own specific potential. The reduction of protons to hydrogen under standard conditions, *that is all activities are equal to 1 at 25°C under 1 atmosphere of pressure*, is set as 0 V and is used as the standard to which all other half reactions are compared, *the so-called Standard Hydrogen Electrode (SHE)*.[1] Using these values, the cell potential E_{cell} (V) of any cell can be calculated. Due to the complexity of the SHE, it is more common for real world experiments to use other reference standards such as Ag/AgCl or Hg/Hg_2Cl_2 (saturated calomel, SCE), which are more practical. Further, formal reporting of potentials throughout this work is typically refenced to the *reversible hydrogen electrode* (RHE), which is a pH corrected variant of the SHE accounting for the shift in potential caused by the change in proton activity.

$$E\ vs\ RHE = E\ vs\ SHE + 0.0592(pH)$$

Faraday's law of electrolysis directly relates the transfer of charge which occurs in an electrochemical reaction:

$$Q = nFN$$

Where the total charge passed *Q (in coulombs, C)* is equal to the Faraday constant *F* $(C\ mol^{-1})$ multiplied by the number of moles *N (mol)* undergoing reaction. The further factor *n* describes the number of electrons transferred per molecule in the reaction.[2] Being able to equate charge transfer to number of molecules allows electrochemistry to explore the kinetics of any half-cell reaction.

Further, the aforementioned standard potential can be related to the Gibb's free energy $(J\ mol^{-1})$ mol of the reaction by:

$$\Delta G_{cell} = -nFE_{cell}$$

Allowing for electrochemistry to explore and predict the thermodynamics of any half-cell reaction.[2]

Of course, reactions are not always occurring under standard conditions, and as such it is important to be able to compare an experimentally observed potential to the expected standard potential. The Nernst equation can be used to predict the observed potential by comparing the activity of the reduced and oxidised forms of the interested species:

$$E = E^o - \frac{RT}{nF} ln \frac{\alpha_{red}}{\alpha_{ox}}$$

Where *R* is the ideal gas constant *(J K^{-1} mol^{-1})* and *T* is the absolute temperature in Kelvin (*K*). This holds true only for fully kinetically reversible reactions, and can be simplified to a potential shift of – 0.0592 V per magnitude difference in α_{red}/α_{ox} at standard temperature and pressure. An electrochemically reversible reaction is one that has minimal energy barrier to electron transfer and thus a high electrochemical rate constant (discussed in section 2.2).

The construction of an electrochemical cell requires that the half reactions be separated onto two electrodes, connected via an external circuit and also by a shared interface able to freely conduct ionic charge. In the vast majority of cases, this interface is provided by a solution of dissolved and dissociated ionic species. The interaction between the electrode and the solution at this boundary is known as the electrical double layer.[1] When the electrode is exposed to the solution (represented in Figure 2.1), ions in the solution rapidly and spontaneously arrange to balance the electrochemical potential at the interface. The *inner Helmholtz plane* (IHP) consist of solvent molecules and ions specifically adsorbed onto the electrode surface, while the *outer Helmholtz plane* (OHP) consists of solvated ions attracted by long range electrostatic forces. The OHP is defined as the closest point the solvated ions can approach the surface while not specifically adsorbed. The region from the OHP to the bulk solution is called the *diffuse layer*, and is characterised by an excess charge density relative to the bulk solution. Any shift in externally applied potential during an experiment will result in a shift in this balance, and as such charge moves without a chemical reaction occurring. This intrinsic property is called capacitance and is seen as a non-Faradaic charging current during polarisation of the electrode, which must be taken into account when measuring the current of a Faradaic process of interest.

Essentially all measured electrochemical interaction happens within this double layer, as the potential experienced by an analyte of interest drops off rapidly as you move from the electrode surface towards the bulk solution. The thickness of this layer depends on the concentration of ionic species present, with a higher concentration resulting in a thinner double layer. Because a non-adsorbing analyte cannot approach past the specifically adsorbed layer, the maximum potential it can experience will be less than the applied potential, and this loss must be taken into account.

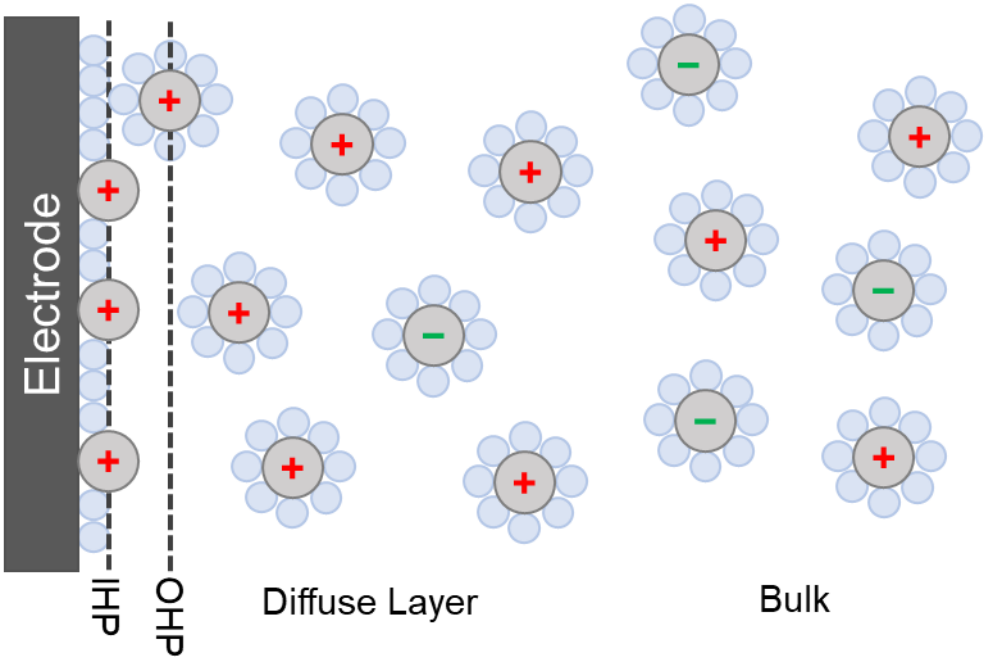

Figure 2.1 *Schematic representation of the double layer at a negatively polarised electrode submerged in an electrolyte, indicating the IHP, OHP, diffuse layer and bulk layer.*

2.2 Electrochemical techniques

Electrochemical techniques can broadly be separated into galvanostatic and potentiostatic, that is those that have a controlled current and measure potential, and those that control potential and measure current. The simplest experiments, chronopotentiometry and chronoamperometry, hold one of these variables and observe how the other changes over time. This can give useful information about how a reaction unfolds over time, such as how rate changes as reactant is consumed, or how the products of the reaction change depending on the energy being supplied per electron.

While these techniques form the basis of continuous electrochemical processes, the amount of useful data that can be acquired from a single experiment is limited. More

advanced techniques in which the controlled variable is altered during the experiment can allow for the rapid collection of experimental data. Voltammetry encompasses a range of techniques in which an applied voltage is shifted at a continuous rate and the effect on current is measured. By far the most popular technique for exploring redox electrochemistry is cyclic voltammetry. An applied potential is swept from one vertex to another, then the direction is reversed, and the potential is swept back to the first vertex, while the current is continuously measured. The profile of this current response (shown in Figure 2.2) can be used to determine a great deal about the nature of the electrochemical process under examination.

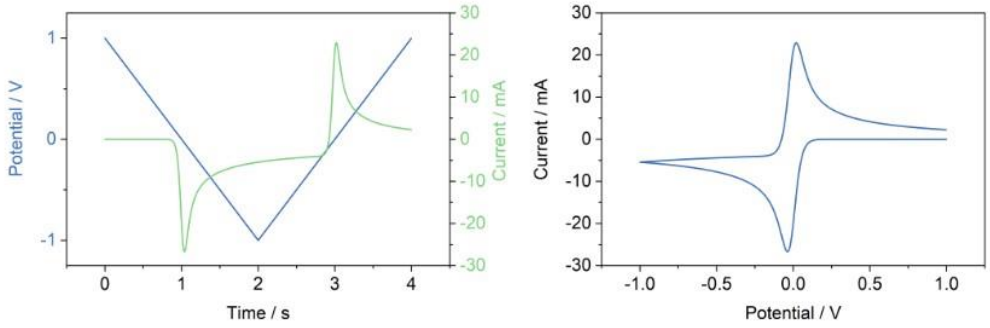

Figure 2. 2 *Simulated cyclic voltammogram. (Left) Plots of voltage vs time and current vs time for a hypothetical redox process as potential is scanned from 1.0 V to −1.0 V, then back to 1.0 V at a rate of 1 V s⁻¹. (Right) Plot of current as a function of voltage for the hypothetical redox process, a voltammogram.*

Depending on the form of the species of interest, a range of responses are possible. Many factors can affect this response including transport effects (diffusion, convection), the aforementioned electron transfer kinetics, electrode area, and analyte concentration. For the ideal case of a highly reversible species under a diffusion-controlled regime, the response will follow the Randles-Sevcik equation:

$$i_p = 0.4463\, nFAC\left(\frac{nFvD}{RT}\right)^{0.5}$$

Or

$$i_p = 2.69 \times 10^5\, n^{1.5} AC(Dv)^{0.5}$$

At 25°C

Where *n* is the number of electrons transferred per molecule, *A* is the area of the electrode in cm^2, *F* is the faraday constant, *C* is the concentration of the analyte in mol cm^{-2}, *v* is the scan rate in V s^{-1}, *D* is the diffusion coefficient in $cm^2\, s^{-1}$, R is the ideal gas constant, and T is the absolute temperature.[3]

A reaction is considered electrochemically reversible when the rate of electron transfer is much greater than the rate of diffusion, while it is considered irreversible when the rate of electron transfer is slow compared to the rate of diffusion. This is reflected in the voltammogram as shown in Figure 2.3. Slow electron transfer kinetics often result from molecules that undergo structural rearrangement upon charge transfer. The key features of a cyclic voltammogram are the anodic and cathodic peak currents and potentials, and the half wave potentials. In a reversible voltammogram, the peak anodic and cathodic current should be equal in magnitude and opposite in sign, and the difference in the peak potentials should be 59 mV for a one-electron process. The midpoint of the two peak potentials should be equal to the standard potential of the half-reaction assuming the diffusion coefficient does not change between the reduced and oxidised forms.

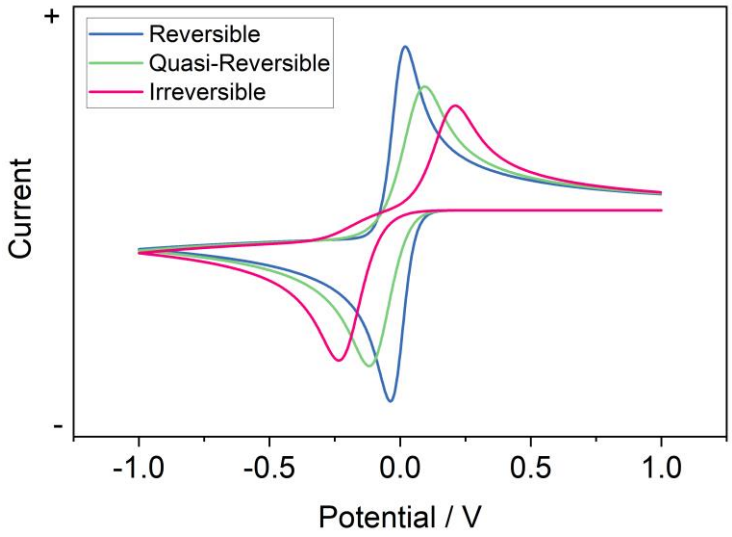

Figure 2.3 *Simulated cyclic voltammograms indicating examples of reversible (blue), quasi-reversible (green) and irreversible (pink) kinetics.*

Under reversible conditions, the difference in peak potentials should remain constant as scan rate is increased, while peak current should increase linearly with the square of scan rate. In irreversible systems, the peak separation will increase as a function of scan rate, while the current also increases proportionally to scan rate. Systems that display peak potential separations of > 59 mV are described as quasi-reversible, where peak potential separation and peak current increase with scan rate but do not follow a fixed trend. The peak current of the reverse scan will also be diminished as compared to the forward scan. Ultimately, all systems will tend toward irreversible kinetics as scan rate is increased due to shrinking of the diffusion layer (as less time is allowed for it to

develop), which increases the concentration gradient at the electrode surface and thus the impact of diffusion.[2]

Beyond this, reversibility can also be lost as a result of chemical transformation after electron transfer. In the simplest case, electron transfer activates the molecule towards a rapid chemical reaction, the product of which is not electrochemically active, so no reverse peak is observed. If the chemical reaction is comparatively slow, a partial loss of the reverse peak may be observed. In the case of fast catalytic reaction where the electrochemically active molecule is not consumed, a large increase in forward current will be observed along with the loss of the reverse peak.

Voltammetry of more complex systems, such as cases of heterogeneous electrocatalysis, can be harder to interpret. The electroactive catalyst is unlikely to undergo its own faradaic process, instead displaying only capacitance in the form of charging current. Meanwhile, the process it is catalysing is unlikely to be reversible (otherwise a catalyst would not be necessary), and as such is unlikely to follow any ideal behaviour. Voltammetry is still popular in the analysis of these materials; however, it is used primarily as a tool of comparison between different experimental conditions, such as shifts in onset potential of the faradaic process and changes in gradient of the current wave indicating a change in activation energy or rate respectively.

2.3 Electrochemical Cells

Two primary cell configurations are used within this work, comprising two-electrode and three-electrode setups respectively. A typical potentiostat consists of a collection of parallel circuits that allow for the measurement of both potential and current across the cell simultaneously.[4] A voltage measurement is taken between the working electrode and the reference electrode, while a current measurement is taken between the working electrode and the counter electrode. In a two-electrode setup, the counter and reference are connected to the same electrode in parallel circuits, whereas in a three-electrode setup, the counter and reference are maintained as separate electrodes. Both configurations have advantages suitable for different applications.

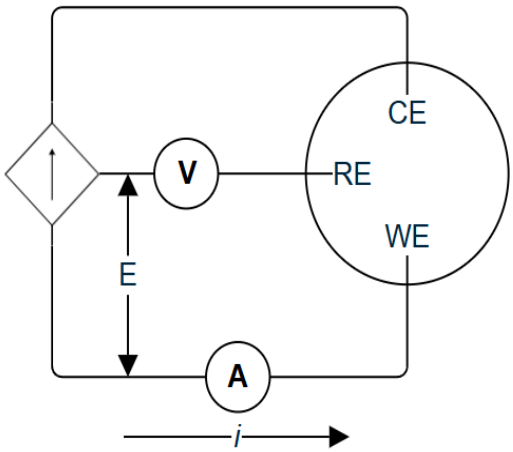

Figure 2.4 *Simplified circuit diagram of a typical three-electrode cell.*

Two-electrode setups are simpler by virtue of having fewer cell components. This makes cell construction less complicated, however less information can be gathered from a single experiment. Potential or current can be interchanged as the independent and dependent variable respectively, however the contribution of the working and counter electrode reactions to overall potential cannot be disentangled. This technique is usually employed for current controlled experiments of cells and electrolysers as examples of realistic operating conditions, where overall efficiency is the main concern.

Three-electrode setups are by comparison more complex. The experiment now relies on three distinct electrodes, each with their own redox process. The two parallel circuits now encompass distinct pairs of half-reactions rather than sharing the same two. This allows potential of the working electrode to be controlled with regard to a fixed and true reference standard. As the circuit passes essentially zero current, the equilibrium at the reference electrode surface is maintained and thus its potential should not change. Meanwhile, the circuit between the working and the counter electrode exists to enable and measure a flow of current as a result of the potential at which the working electrode is being held relative to its environment. The potential between the working and the counter electrode (the compliance voltage) can still be measured to give an idea of overall cell efficiency as in a two-electrode setup.

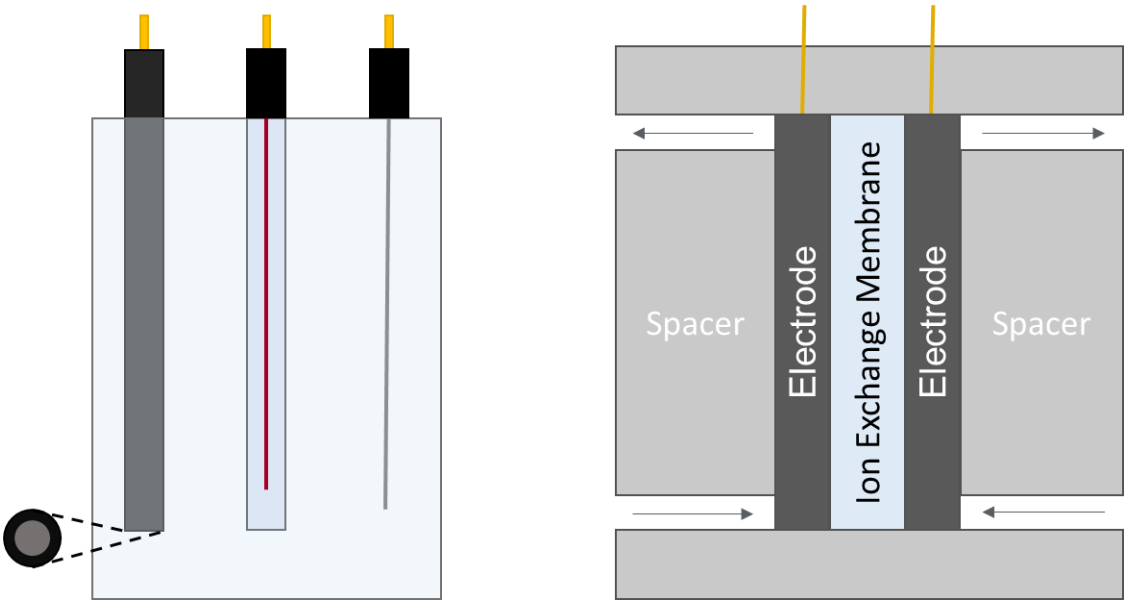

Figure 2.5 *(left) Schematic of a three-electrode voltammetry cell. (right) Schematic of a two-electrode flow cell.*

2.4 Characterisation techniques

2.4.1 Electron Imaging

Electron imaging is a popular technique to explore the surfaces of nano-scale materials. Electrons, having a de Broglie wavelength much smaller than the wavelength of visible light, allow for images with much higher resolution than traditional optical microscopes.[5] Surface structure and shape can be examined to scales below 1 nm, and for samples with good contrast, atomic layering and even individual atoms can be observed. Such techniques are highly valuable in studying electrocatalytic materials, as surface structure plays a huge role in catalyst activity and selectivity. This is usually coupled with spectroscopic techniques such as *energy-dispersive x-ray spectroscopy* (EDX) which allows for synchronous determining of elemental composition within the sample.

A focussed beam of electrons is incident on the surface of the sample, and depending on how they are measured, different types of images are possible. *Scanning electron microscopy* (SEM) detects scattered electrons, while *transmission electron microscopy* (TEM) detects transmitted electrons.[6] This makes them suited for determining different structural properties, with SEM excellent at exploring surface topography while TEM is more suited for inner structure.

2.4.2 Spectroscopy

UV/vis spectroscopy can be a powerful tool when analysing complexes in their solution state. Many transition metal complexes are strongly coloured due to their absorbance of visible wavelength light, resulting from energy transitions within their partially filled outer d-electron shell, as well as charge transfer to and from ligands. This intrinsic property can be exploited to determine solution concentrations using the Beer-Lambert law:

$$A = \varepsilon \cdot c \cdot l$$

Where the predicted absorbance *A* (arbitrary units) is the product of the extinction coefficient for the energy transition ε (M^{-1} cm^{-1}) multiplied by the solution concentration *c* (M) and the path length *l* (cm).[5]

2.4.3 X-ray

X-ray diffraction (XRD) is a useful technique to determine the phase structure of an ordered material. Due to the intrinsic lattice spacing of the material, x-rays reflected by elastic scattering will undergo constructive interference only when irradiated at specific angles.[5] Bragg's law can be used to relate this angle to the lattice spacing of the material for a given wavelength of radiation:

$$n\lambda = 2d \sin\theta$$

XRD can be especially powerful for crystalline material as it allows for the full structural determination, however even for amorphous or metallic materials it is useful as a fingerprint technique, as each lattice plane of the material will have unique spacing, resulting in a characteristic diffractogram with peaks corresponding to each unique lattice spacing.

X-ray fluorescence (XRF) is spectroscopic technique that can be used to determine the elemental composition of a sample.[7] X-rays are used to displace electrons from the inner shell of an atom, which results in an electron from the outer shell moving to the now vacant lower energy level and releasing a fluorescent x-ray of a fixed energy. These spectral lines are intrinsic to each element and can be used to determine the composition of a sample. This technique typically works better the heavier the element of interest, as lighter elements are less likely to interact with the high energy x-rays.

2.4.4 Elemental Analysis

Elemental analysis, performed using a combustion analyser, can be used to determine the percentage composition of a sample's mass contributed by the elements carbon, hydrogen, nitrogen, and sulphur. This information can be useful tool when determining the purity of a compound, especially for paramagnetic and ferromagnetic compounds which are unsuitable for quantitative NMR experiments.

2.5 Equipment List

Electrochemical experiments were performed using a Biologic SP300 potentiostat. Voltammetry was performed in a small glass cell of approximately 20 mL volume, using a 3 mm diameter glassy carbon working electrode unless otherwise stated. For aqueous experiments, the reference electrode was typically Ag/AgCl, using either 1 M KCl or 3 M NaCl inner solution. The potentials of the reference electrodes were periodically checked against a saturated calomel reference electrode to compensate for any potential drift over time, and all potentials reported against RHE throughout the work were calculated rated to this. For non-aqueous work, electrochemical experiments were referenced with either a bare silver wire or a silver wire isolated in a fritted tube containing 10 mM $AgNO_3$ and 0.1 M NBu_4 ClO_4. At the end of each experiment, a small amount of ferrocene (Fc) was added as an internal reference standard. All voltammetry experiments used a platinum wire counter electrode.

Electron imaging within the university was performed using a JEOL JSM-7800F SEM and a JEOL JEM-1010 TEM. Access to a Titan G2 80-200 S/TEM ChemiSTEM was provided by the Royce Institute at Manchester University. UV/vis spectroscopy was obtained using an Agilent Cary 60 spectrometer. XRD was performed using a Rigaku SmartLab diffractometer. XRF was performed using a Shimadzu EDX 8000. NMR was performed using a Bruker AVANCE III 400.

2.6 Redox Flow Cell Design

To access the charged state of the mediator, a large electrochemical flow cell with geometric electrode areas of 16 cm^2 was used to charge the electrolytes for decoupled CO_2 reduction and to test performance of the electrolytes as a cell. The cell was constructed from an outer frame of steel, polypropylene electrolyte diffusers, brass current collectors, graphite composite electrode plates, graphite felt electrodes, EPDM gaskets, Fumatek Fumapem F-930 cation exchange membrane. A detailed schematic can be found in the Appendix. During the work, stainless steel tubing connection fittings were replaced with plastic after poor battery cycling efficiency was recorded.

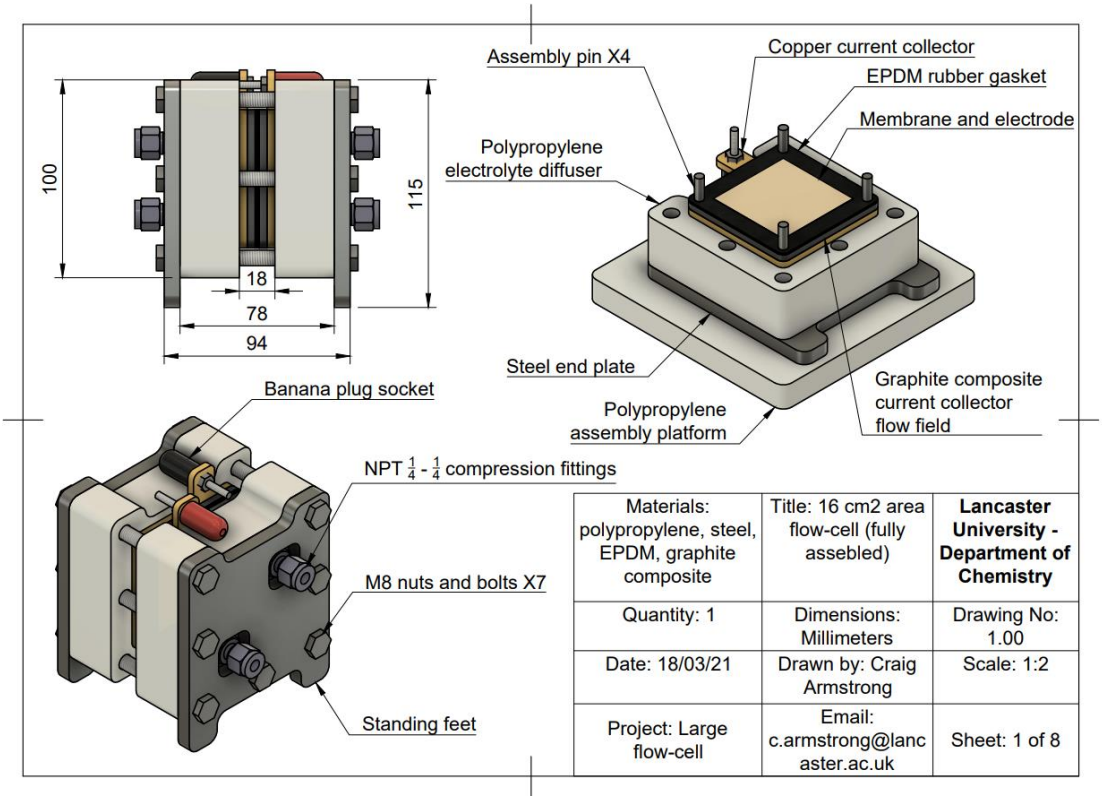

Figure 2.6 *Schematic representation of the 16 cm² geometric area flow cell used to access the charged state of the mediator, designed by Dr Craig Armstrong for the group.*

2.6.1 H-cell

For conventional electrolysis using homogeneous and heterogeneous electrocatalysts, a glass H-cell was employed. The working and counter compartment were separated by an ionically conductive membrane. For homogeneous catalysis, the working electrode was a graphite rod, while for heterogeneous catalysis the working electrode was a glassy carbon plate with an exposed geometric surface area of 1.44 cm^2.

2.6.2 Reactor design (batch)

A Schlenk flask under a CO_2 (or N_2 for controls) atmosphere was used as a reaction vessel. The atmosphere was achieved by reducing the pressure in the flask to < 1mBar by applying vacuum, followed by refilling with the desired gas from a manifold. This was repeated 5 times to eliminate as much oxygen as reasonably possible. To this, a fixed aliquot of charged mediator at a known concentration, and thus known total charge, was added to the flask also containing the desired catalyst. Discharge occurred spontaneously, and the products were quantified by gas and ion chromatography. Experiments were completed in triplicate simultaneously, in which the three aliquots of

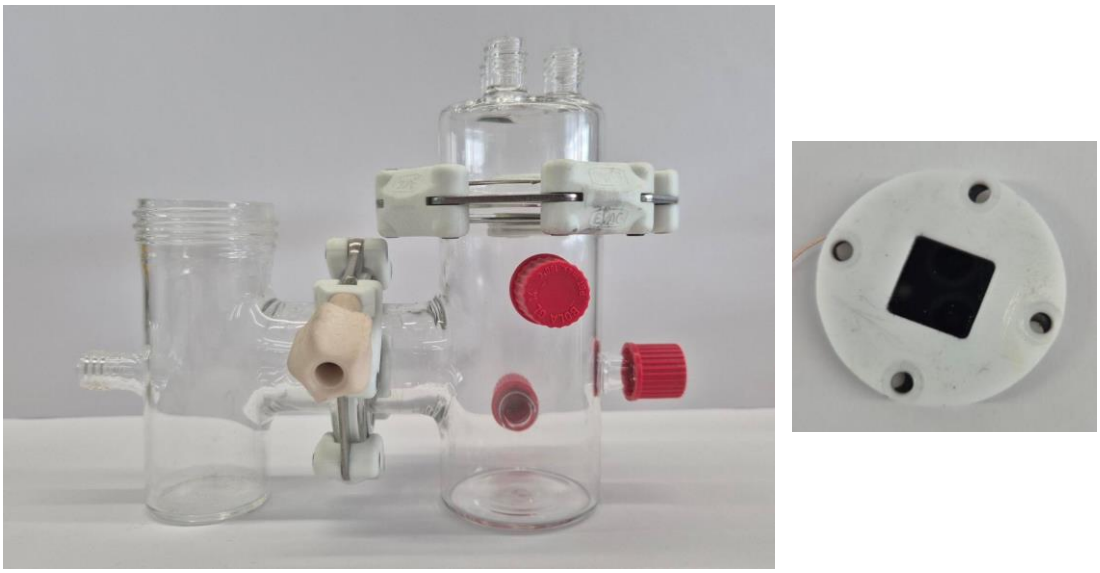

Figure 2.7 *H-Cell used in conventional electrolysis experiments and the glassy carbon plate electrode used for testing heterogeneous catalysts.*

mediator were charged together before being added to the vessels. Analysis of the headspace gas was delayed by 30-50 minutes from the first to last sample due to the time delay of running each sample through the GC (15-25 minute separations). As a result, all the flasks were left until no-visible reaction was occurring before sampling, so no kinetic data was obtained beyond a rough estimate of discharge time. Analysis of the liquid products was performed only after satisfactory gas chromatograms were obtained for all three vessels.

A Schlenk flask was chosen as a reaction vessel specifically because they are designed for work under an inert atmosphere. The tapped side port facilitates the transfer of gasses, while the top joint allows for the use of disposable septa which can be pierced by needle to allow for the injection of the mediator while maintaining easy cleaning of the flask between experiments. The volume of flask, along with mediator volume and concentration was chosen such that minimal change in pressure occurred as a result of the reaction, and that the resulting products could be brought within the concentration ranges of the calibration with a sensible degree of dilution. Some dilution was necessary to achieve the sample volume needed for injection (at least 30 mL) without altering the pressure within the flask during extraction. The typical volume of the flasks was 150-170 mL, with each flask individually measured to the nearest 0.01 cm^3 by measuring the mass of the flasks empty and completely filled with water.

Figure 2.8 *Experimental setup used for the batch screening of catalyst materials for DECO_2R.*

2.6.3 Reactor design (flow)

As an initial design, a three necked round bottom flask was used as a makeshift flow reactor. In this instance, only the gas was flowing. CO_2 was injected through one arm of the flask by a needle submerged below the electrolyte surface. A second needle in the other arm allowed headspace gas to flow out of the flask and through the injection loop of the GC where its composition was analysed every 15-20 minutes. Mediator and catalyst were added by the same manner as described for the batch reactor design. This allowed for the collection of semi-quantitative rate data, as the composition of the outflowing gas reflected the rate of production. The volume of the flask was measured to be 163.15 cm^3.

2.7 Product quantification

To separate the products for quantification, gas and ion chromatography were utilised. Chromatography allows for the separation of compounds based on their relative affinity to the stationary phase within a column and mobile phase (eluent) used to move the

sample through the column. A signal is measured by a detector at the end of the column, and as the compounds leave, they are detected by a change in the signal response relative to the signal given by the pure eluent. In a successful separation, each compound will move through the column at a different rate, referred to as retention time, such that they are fully resolved and the change in signal at the detector is due to the presence of only one compound at a time.

2.7.1 Gas products

Calibrations were prepared to allow for the quantification of the products H_2, CO, CH_4, and C_2H_4. The gases were analysed on a Shimadzu 2030 GC system equipped with a ResTek ShinCarbon ST 80/100 column and barrier ionisation discharge (BID) detector,

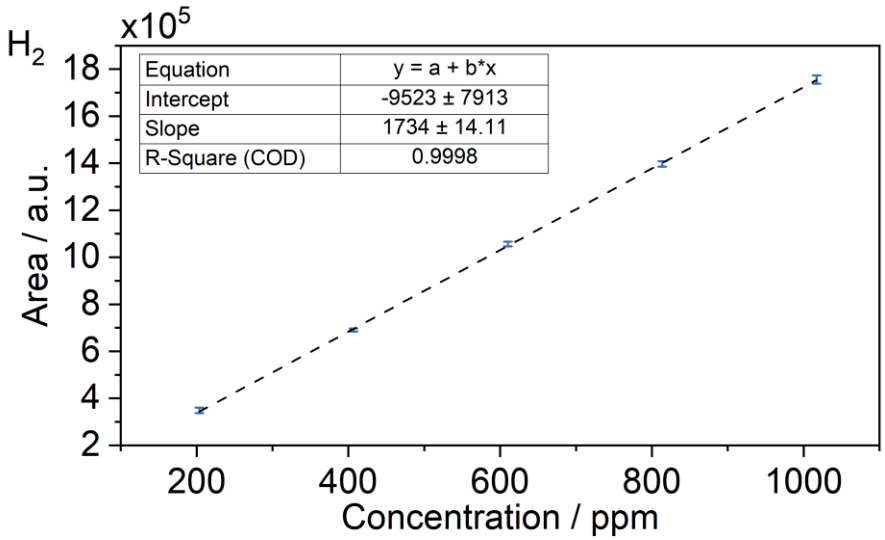

Figure 2.9 *Calibration plot for H_2 quantification in the range 200-1,000 ppm.*

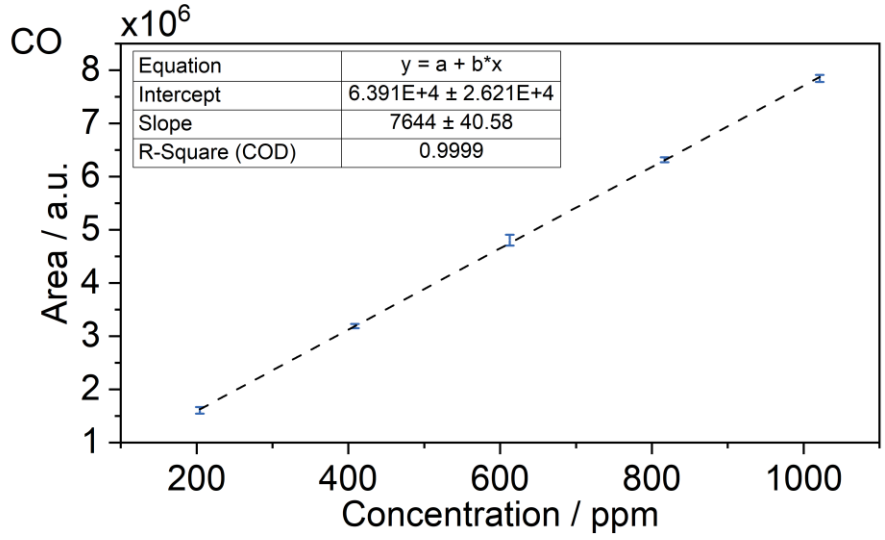

Figure 2.10 *Calibration plot for CO quantification in the range 200-1,000 ppm.*

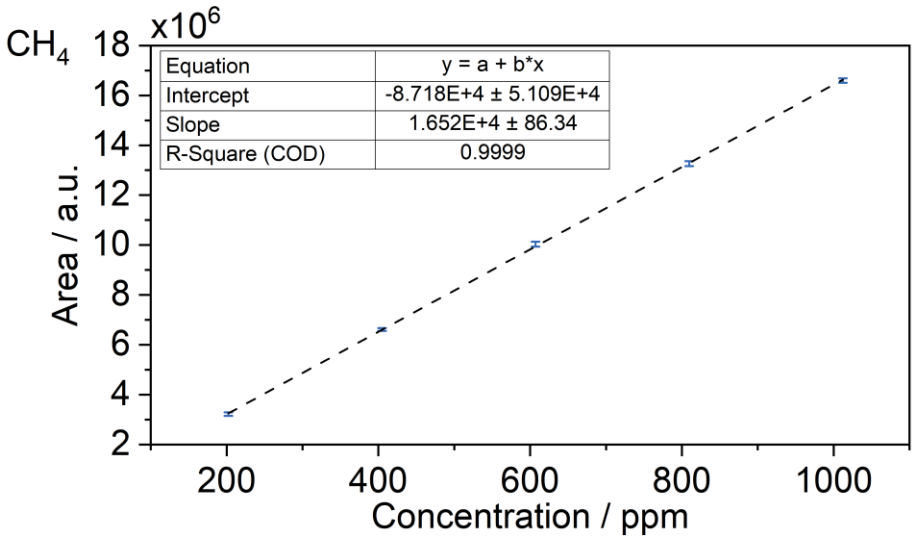

Figure 2.11 *Calibration plot for CH_4 quantification in the range 200-1,000 ppm.*

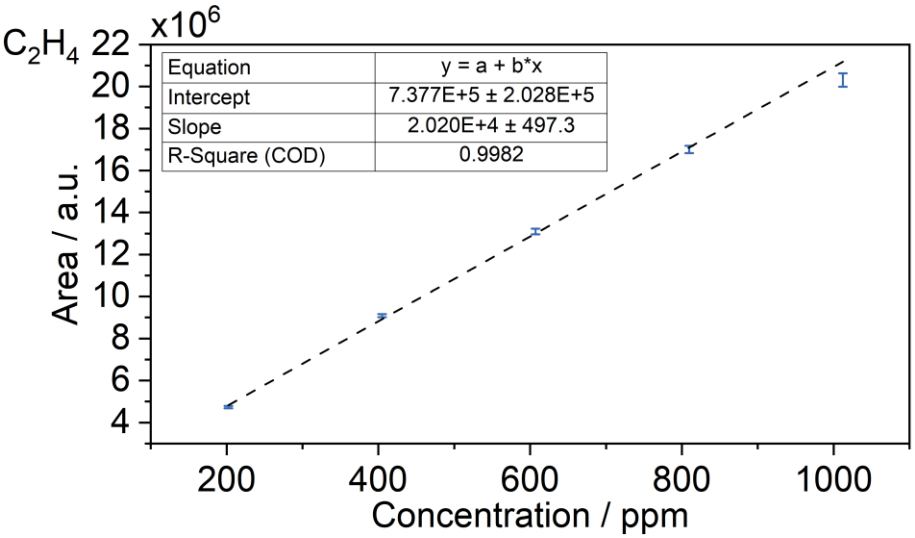

Figure 2.12 *Calibration plot for C_2H_4 quantification in the range 200-1,000 ppm.*

using helium as the eluent gas. Linear calibrations in the range 200-1,000 ppm were prepared for all four gases, with further curved calibrations in the range 2,000-100,000 prepared for H_2 and CO. Certified calibration gas standards were purchased from BOC ltd. The range of concentrations were prepared by dilution of these standards with CO_2 by the use of two gas tight syringes. As an example, a 5-fold dilution was achieved by taking 10 mL of sample into the first syringe and 40 mL of CO_2 into the second, after which the gases were transferred between the syringes 5 times to ensure thorough mixing. Over the course of this work, several iterations of the calibrations were used as changes were made to the instrument. The confidence of the linear calibration is high, with R^2 values >0.99 in the 200-1,000 ppm range for all gases.

The high ppm (2,000-100,000 ppm) calibrations were fitted to a curve approximated by a one phase association:

$$y = y_0 + (Plateau - y_0)(1 - e^{-kx^a})$$

Where *plateau* corresponds to the maximum y value, y_0 corresponds to the intercept, and the values of the constants *k* and *a* were optimised to minimise the error calculated from the sum of the square of the difference between real and predicted *y* values for each concentration point.

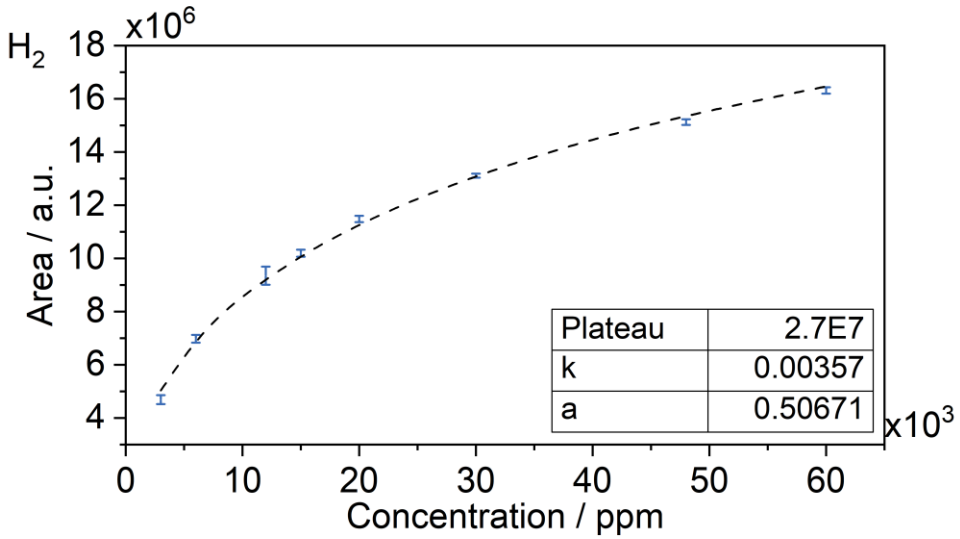

Figure 2.13 *Calibration plot for H_2 quantification in the range 3,000-60,000 ppm.*

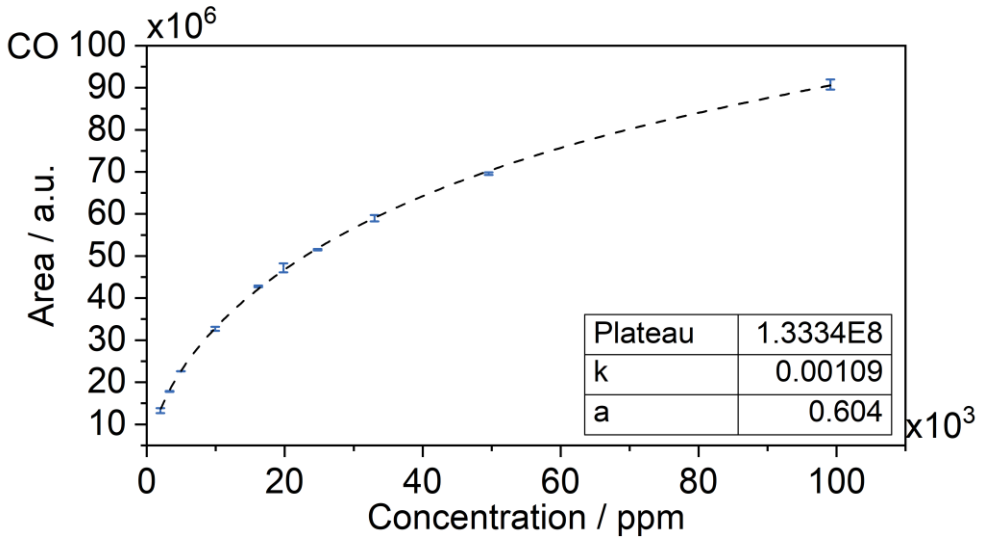

Figure 2.14 *Calibration plot for CO quantification in the range 2,000-100,000 ppm.*

With these calibrations, the concentration of the product gases in the headspace of the reaction vessel were measured. Knowing the total volume of each reactor and the

volume of electrolyte within, the total amount of products formed can be estimated. It was assumed that the amount of each product dissolved in the electrolyte was negligible as they are all sparingly soluble.

From this, the faradaic efficiency for each product was determined.

The amount of each gaseous product in moles within the headspace was estimated;

$$\textit{Moles product [mol]} =$$

$$\frac{\textit{Headspace concentration [ppm]}}{10^6} \times \textit{Moles of gas in headspace [mol]}$$

where the ideal gas law was used to determine the total number of moles within the headspace;

$$\textit{Total moles of gas in headspace} =$$

$$\frac{\textit{Headspace pressure [Pa]} \times \textit{Headspace volume [m}^3\textit{]}}{\textit{Ideal gas constant [J K}^{-1}\ \textit{mol}^{-1}\textit{]} \times \textit{Temperature [K]}}$$

By considering the electron stoichiometry, the amount of charge needed to form each product can be calculated;

$$\textit{Charge required [C]} =$$

$$\textit{Moles product [mol]} \times \textit{Electron stoichiometry} \times \textit{Faraday constant [C mol}^{-1}\textit{]}$$

which can then be compared to the total charge passed;

$$\textit{Charge passed [C]} =$$

$$\textit{Moles of mediator [mol]} \times \textit{Electron stoichiometry} \times \textit{Faraday constant [C mol}^{-1}\textit{]}$$

to determine the faradaic efficiency as a quantum yield;

$$\textit{Faradaic efficiency} = \frac{\textit{Charge required [C]}}{\textit{Charge passed [C]}} \times 100$$

Figure 2.15 *Gas syringes used to prepare sample dilutions.*

2.7.2 Liquid Products

The same approach was employed for the liquid phase product HCOO(H), with the product moles calculated assuming a sample density of 1 kg L^{-1}

$$\text{Moles product [mol]} = \frac{\text{Measured Concentration [ppm]}}{\text{Molecular mass } [\text{Kg mol}^{-1}]} \times \text{Total volume of electrolyte [L]}$$

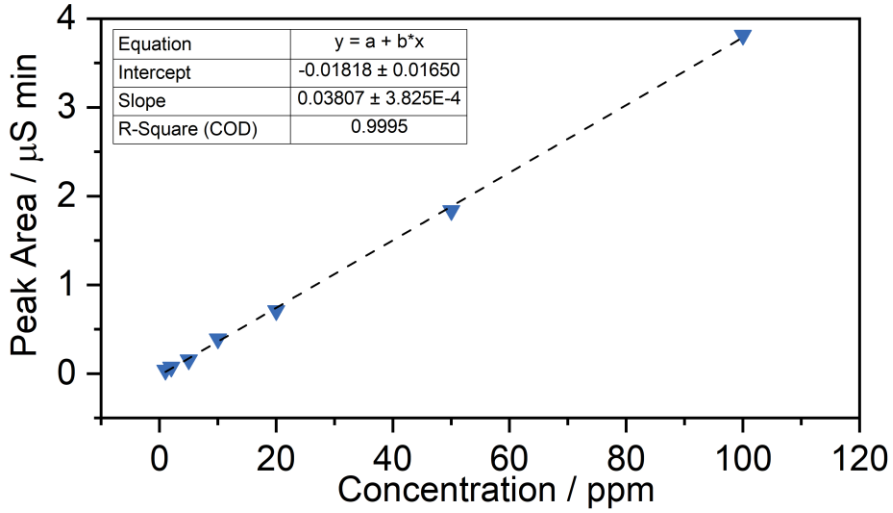

Figure 2.16 *Calibration plot for HCOO(H) quantification in the range 1-100 ppm.*

2.8 References

1 A. J. Bard and L. R. Faulkner, *Electrochemical Methods: Fundamentals and Applications*, John Wiley & Sons, Ltd, 2nd edn., 2001.

2 O. Simoska and S. D. Minteer, *Techniques in Electroanalytical Chemistry*, American Chemical Society, Washington, DC, USA, 2022.

3 R. G. Compton and C. E. Banks, *Understanding voltammetry*, Imperial College Press, London, 2nd ed., 2011.

4 A. W. Colburn, K. J. Levey, D. O'Hare and J. V. Macpherson, *Phys. Chem. Chem. Phys.*, 2021, **23**, 8100–8117.

5 P. W. Atkins and J. de Paula, *Atkins' Physical Chemistry*, Oxford University Press, Oxford, 14th edn., 2014.

6 ThermoFisher, Transmission Electron Microscopy vs Scanning Electron Microscopy, https://www.thermofisher.com/uk/en/home/materials-science/learning-center/applications/sem-tem-difference.html, (accessed 7 May 2025).

7 ThermoFisher, What is XRF (X-ray Fluorescence) and How Does it Work?, https://www.thermofisher.com/blog/ask-a-scientist/what-is-xrf-x-ray-fluorescence-and-how-does-it-work/, (accessed 7 May 2025).

Chapter 3: Redox Active Molecules for Energy Storage and Catalysis

The work presented in this chapter was published under the title 'Exploring the Electrochemistry of Iron Dithiolene and Its Potential for Electrochemical Homogeneous Carbon Dioxide Reduction' in the journal *ChemElectroChem* in 2022.[1]

Some of this work was completed as a join investigator alongside Dr Craig Armstrong. This includes: part of section 3.3.2 *Voltammetric Characterisation of Fe mnt*, section 3.3.4 *CO_2 Electrolysis Studies*, section 3.3.5 Catalyst Stability, section 3.3.6 *Mechanistic Insights*, as well as the single crystal XRD work in section 3.2.1 *Synthesis*, alongside collaborators of the published work.

3.1 Introduction

The search for redox active molecules suitable for $DECO_2R$ began with molecules the group was already familiar with. The complexes of maleonitriledithiolene (mnt) with the transition metals V, Fe, Co, Ni, and Cu were evaluated as electrolytes for single species symmetric non-aqueous redox flow batteries by Dr Ross Hogue, and Dr Craig Armstrong as part of his thesis, and was published in *ChemSusChem* in 2019.[2] It was found that these molecules each exhibit multiple reversible redox events within the stability window of the acetonitrile solvent. Redox flow batteries (RFB) were assembled from the complexes of V, Co, Ni, and Cu, while the Fe complex displayed limited solubility (<0.03 M) and thus was not considered suitable as a battery electrolyte. Battery performance was mixed, with the complexes of V, Co and Cu exhibiting moderate efficiency but relatively poor capacity retention. The complex of Ni however displayed rapid capacity fade and poor efficiency. Single redox couple battery cycling indicated that the more negative redox couple was the larger contributor to instability for all complexes with the exception of the V complex. This is despite the appearance that all oxidation states utilised were stable on the timescale of cyclic voltammetry.

Despite the limited performance of these complexes as flow battery electrolytes, they were briefly considered as redox mediators for the ECO_2R. The complexes of Fe, Co, Ni and Cu were explored under CO_2R conditions to determine if they were sufficiently stable. Initial results indicated a homogeneous catalytic reaction between the reduced form of the Fe mnt complex and CO_2, and as such this chapter presents an exploration of this process.

Many transition metal complexes have been reported as homogeneous catalysts for the electroreduction of CO_2, particularly in non-aqueous environments.[3] The highest performing catalysts are typically complexes of noble metals such as rhenium,[4,5] rhodium[6] and ruthenium[7,8] featuring carbonyl and polypyridyl ligands. More earth abundant metals have however been utilised to much success, such as porphyrin complexes of iron[9,10] and cobalt,[11,12] cyclam complexes of nickel,[13,14] and pyridine complexes of manganese.[15] The porphyrin complexes of iron are of particular note due to their similarity to active sites in many enzymes.[16] Pioneered by the Savéant research group, these catalysts have become a model for exploring the kinetics of homogeneous ECO_2R. Being derived only from earth abundant elements further adds to their appeal, making the catalyst more accessible and reducing cost.

While reports concerning dithiolene complexes are relatively common, this is primarily due to the unusual electronic behaviour that these non-innocent ligands enable, resulting in novel complexes with interesting intrinsic optical and magnetic properties.[17] It is less common for these molecules to be reported based on catalytic function, however a few examples do exist. The non-innocent ligand interactions with the metal centre allow for interesting redox processes to occur. One such process is olefin purification by its reversible addition to the sulphur-metal core.[18] There are also a number of complexes reported for the electro- and photo-catalytic reduction of water to hydrogen. These primarily utilise nickel or cobalt, however examples using molybdenum and iron are similarly reported.

For CO_2R however, only limited examples exist. A class of complexes utilising bio-inspired molybdopterin-like ligands with a nickel metal centre were first reported Fogeron *et al* in 2018.[19,20] They found that formate was the most accessible product, with faradaic efficiency in the 50-60% range, with CO and H_2 also observed in the 15% and 10% range respectively. It is worth noting the use of mercury working electrodes in these reports, which have the advantage of further suppressing hydrogen evolution compared to carbon-based electrodes. Additionally, such complex ligands rely on complicated synthetic procedure, making large scale production costly. Given the commonality of metal-sulphur cores in many enzymes,[21,22] and more specifically the importance of iron-sulphur cores in electron transport chains,[23] it is unsurprising that these complexes are capable of catalysing electrochemical reduction reactions.

Of the complexes explored herein, those with cobalt and iron centres have previously been reported as catalysts for the reduction of protons, photocatalytically for Co mnt,[24] and electrochemically for Fe mnt.[25] However, no reports have been published

indicating the reactivity of any of the mnt complexes discussed herein with CO_2 before this work.

In this work, the suitability of the maleonitriledithiolate complexes of iron, cobalt, nickel, and copper as homogeneous catalysts for ECO_2R in acetonitrile solvent are discussed, specifically with regard to the iron complex which initially appeared highly responsive to the presence of CO_2 and as such was explored in detail.

3.2 Experimental

3.2.1 Synthesis

Initial samples of the metal-mnt complexes were provided from the synthesis performed for the previously reported work. As part of this work, only the Fe mnt complex was synthesised. The following procedure represents a typical run through of the synthesis.

To begin, the ligand is synthesised by a two-step reaction. A suspension of NaOH (9.54 g, 238 mmol) in DMF (30 mL) was initially prepared by reducing the NaOH to a fine powder using a pestle and mortar. To this, sulphur (7.65 g, 238 mmol) was slowly added over 5 min. The mixture was then stirred for 30 min at 100 °C, before cooling to 15 °C. Once cool, a solution of chloroacetonitrile (6.05 g, 80 mmol) in DMF (6mL) was added dropwise over 20 min. The tan-brown reaction mixture was warmed to room temperature and was stirred for 1 h. Isobutanol (50 mL) was added and the reaction warmed to ~60°C, hot filtered, and washed with 200 mL of boiling isobutanol until a clear filtrate was obtained. The filtrate was allowed to cool, after which diethyl ether (100 mL) as added. The solution was cooled to -20°C, and crystallisation of the intermediate was initiated by scratching the flask with a spatula. The crystals were collected by filtration and washed with further diethyl ether (100 mL) and was isolated as $NCCS_2Na{\cdot}2.5DMF$ (7.67 g, 31 %).

The $NCCS_2Na{\cdot}2.5DMF$ intermediate was then dissolved in H_2O (60 mL) to give a brown solution which was stirred for 48 h, during which dimerization occurred, resulting in a light brown solution with a sulphur precipitate. The mixture was filtered through celite funnel and washed with H_2O (30 mL), removing the sulphur. The light brown filtrate was dried to a brown oil by rotary evaporator, mixed with EtOH (200 mL) and again evaporated to give an orange paste. The paste was redissolved in boiling EtOH (40 mL) and hot-filtered using further boiling EtOH (100 mL) to wash the filtered solid. The filtrate was reduced in volume by 75% through use of rotary evaporation, to which diethyl ether (60 mL) was added, resulting in a yellow/orange precipitate. The mixture

was stirred at 0 °C for 30 min and then filtered to give a yellow/green powder which was dried under high-vacuum at 60 °C for 1 h, to yield $Na_2mnt{\cdot}3H_2O$ (1.2 g, 21 %). ^{13}C NMR (D_2O, 100 MHz): δ = 126.30, 122.74. Anal calculated. for $C_4N_2Na_2S_2{\cdot}3H_2O$: C 20.00, H 2.52, N 11.66, S 26.70 %; found: C 19.89, H 2.15, N 9.67, S 22.05 %. ^{13}C NMR data was consistent with the previously reported work.

The Fe mnt complex was then synthesised by the reacting the isolated $Na_2mnt{\cdot}3H_2O$ (800 mg, 4.30 mmol) dissolved in 1:1 H_2O/EtOH (20 mL) with a solution of $FeCl_3$ (341 mg, 2.10 mmol) in H_2O (6 mL) resulting immediately in a dark brown-red solution. The reaction was stirred for 30 min, after which it was filtered through a celite funnel and washed with 1:1 H_2O/EtOH (10 mL). The filtrate was collected and a solution of Et_4NCl (670 mg, 4.30 mmol) dissolved in EtOH (8 mL) was added dropwise to give a dark precipitate. After stirring for 30 min, the sticky black solid was filtered, washed with water (10 mL), then ice cold 1:1 H_2O/EtOH (10 mL), then recrystalised by dissolving in hot acetone (15 mL), adding 20 mL hot isopropanol then reducing the volume to 20 mL by heating, and cooling to 0°C. The resulting black microcrystalline solid was filtered, washed with ice cold isopropanol (20 mL), and dried to yield $(Et_4N)[Fe(mnt)_2]{\cdot}2H_2O$ (662 mg, 66 %). Anal calculated. for $C_{16}H_{20}FeN_5S_4{\cdot}2H_2O$: C 38.24, H 4.81, N 11.15, S 25.52 %; found: C 38.68, H 4.37, N 15.04, S 25.68 %; HRMS (ESI^-): m/z = 335.8354 $[Fe(mnt)_2]^-$ (calculated = 335.8361). UV-vis: λ_{max} / cm (ε / L mol^{-1} cm^{-1}) = 241.0 (19904), 270.0 (26699), 300.0 (15561), 358.5 (12060), 451.0 (9118).

Single crystal analysis performed by Dr Craig Armstrong, shown in Figure 3.1, indicated that the $Fe(mnt)_2$ catalyst exists as the binuclear dimer $[Fe_2(mnt)_4]^{2-}$ in the solid phase whereby each Fe centre adopts a square pyramidal coordination with five sulphur donors, giving a biologically relevant Fe_2S_8 core.

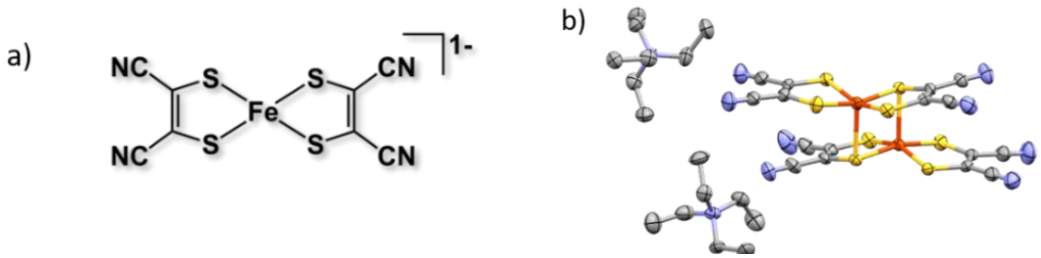

Figure 3.1 *a) Structure of the iron(III) bis-maleonitriledithiolene complex $Fe(mnt)_2^{1-}$. b) Crystal structure of $(Et_4N)_2[Fe_2(mnt)_4]$ obtained from single crystal XRD analysis; ellipsoids set at 50 % probability. Hydrogen atoms have been omitted for clarity. A table of X-ray data can be found in the supplementary information of the published paper (doi.org/10.1002/celc.202200610).*

3.3 Results and Discussion

3.3.1 Initial Screening

The response of the metal complexes to the presence of both water and CO_2 was analysed by cyclic voltammetry to determine their suitability as redox mediators for ECO_2R. The presence of water was included as a proton source for the reduction of CO_2, as this is typically required.

As mentioned in the introduction, the Fe mnt complex displayed interesting reactivity with CO_2 under reducing conditions. As shown in Figure 3.2, the cyclic voltammetry under fully inert conditions gave the expected response, with two consecutive reductions at −0.69 and −2.11 V vs ferrocene (Fc) respectively. When the electrolyte is sparged with CO_2 and the voltammetry is repeated however, all reversibility of the second reduction is lost, instead appearing as an irreversible EC mechanism. It is suspected that the doubly reduced complex undergoes rapid reaction with the dissolved CO_2 to form an electrochemically inactive complex adduct. A minor increase in peak current is noted however this was considered catalytically negligible.

Introducing a proton source in the form of water however resulted in further change in the behaviour of the doubly reduced complex. As seen in Figure 3.3, even under a nitrogen atmosphere the second reduction is no longer fully reversible, although some

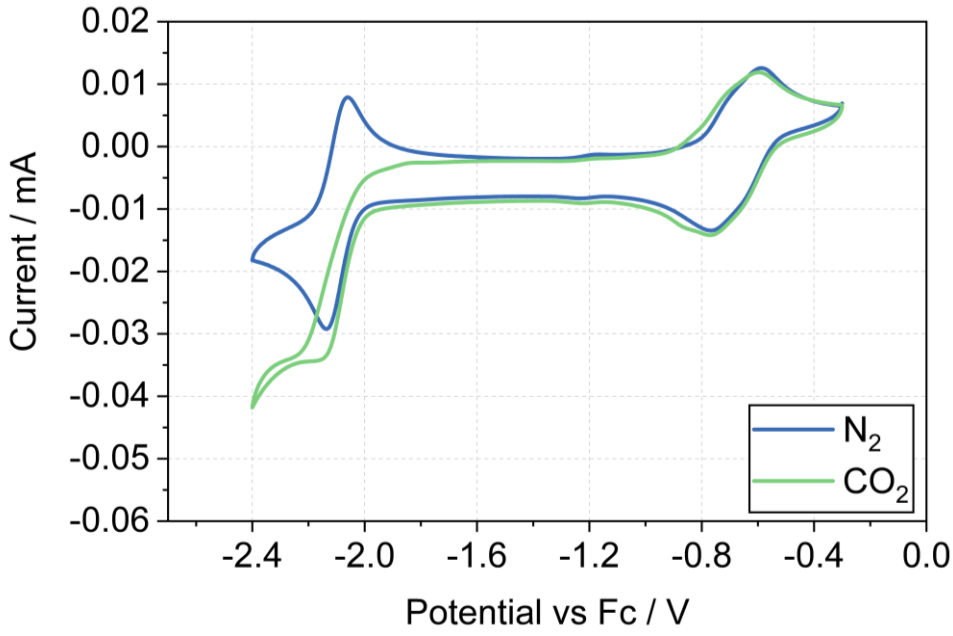

Figure 3.2 *Cyclic voltammetry of $Fe(mnt)_2^{1-}$ at a glassy-carbon (GC) electrode under N_2 and CO_2 in the absence of a proton source (100 mV s^{-1}, second scans shown). The electrolyte was composed of 1 mM $(Et_4N)[Fe(mnt)_2]$ with 100 mM tetrabutylammonium hexafluorophosphate ($TBAPF_6$) supporting electrolyte in acetonitrile (MeCN) solvent.*

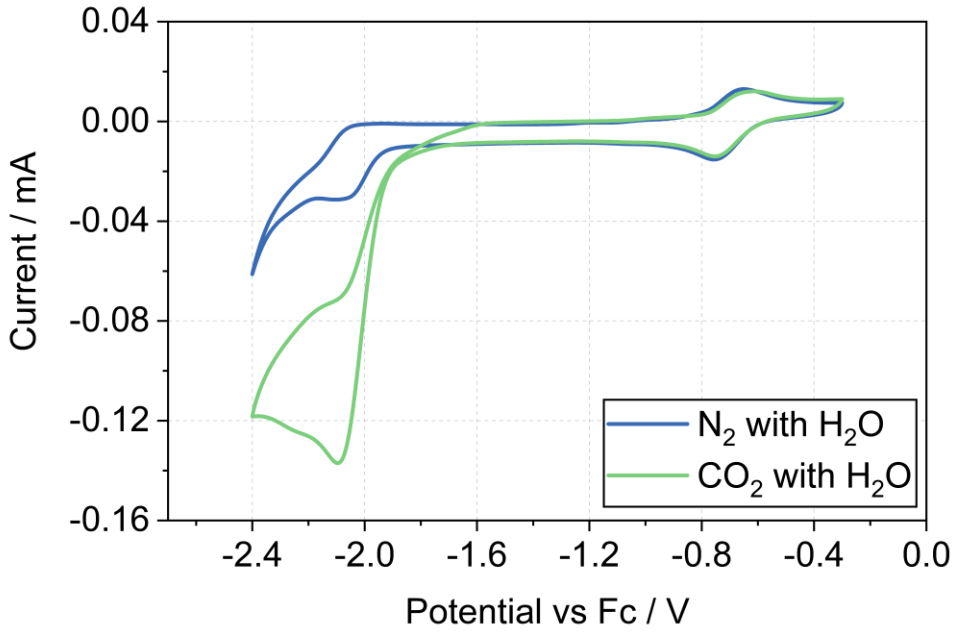

Figure 3.3 *Cyclic voltammetry of $Fe(mnt)_2^{1-}$ at a glassy-carbon electrode under N_2 in the and CO_2 in the presence a proton source (100 mV s^{-1}, second scans shown). The electrolyte was composed of 0.91 mM $(Et_4N)[Fe(mnt)_2]$ with 5.1 M H_2O and 100 mM tetrabutylammonium hexafluorophosphate ($TBAPF_6$) supporting electrolyte in acetonitrile (MeCN) solvent.*

current contribution from the oxidative back peak is still evident, suggesting a slower reaction with water than CO_2. Interestingly, the combination of a water and CO_2 resulted in a huge increase in reduction current for the second reduction. This impressive increase in current suggests the complex is undergoing a catalytic reaction with the CO_2 and water which oxidises the complex allowing it to be reduced again.

The same experiments with the other metal mnt complexes did not result in any noteworthy outcomes. The Ni and Cu complexes showed no response to the presence of CO_2, with the voltametric trace overlaying that of N_2 sparged electrolyte. The addition of water resulted in a loss of reversibility for the second reduction of the nickel complex, although no catalytic current was observed. Current crossover at more negative potentials suggests decomposition of the complex in the presence of both water and CO_2. For the copper complex, the presence of water caused a slight positive shift of the second reduction, however no effect on reversibility was noticed. The cobalt complex did show a slight increase in cathodic current when in the presence of CO_2 and water, but the response was considered catalytically negligible (Figure 3.4a). The onset of hydrogen evolution did shift more positive in the presence of CO_2; however, this is likely due to the decrease in pH associated with dissolved CO_2 reacting with water to form carbonic acid and not a result of any direct reactivity with CO_2.

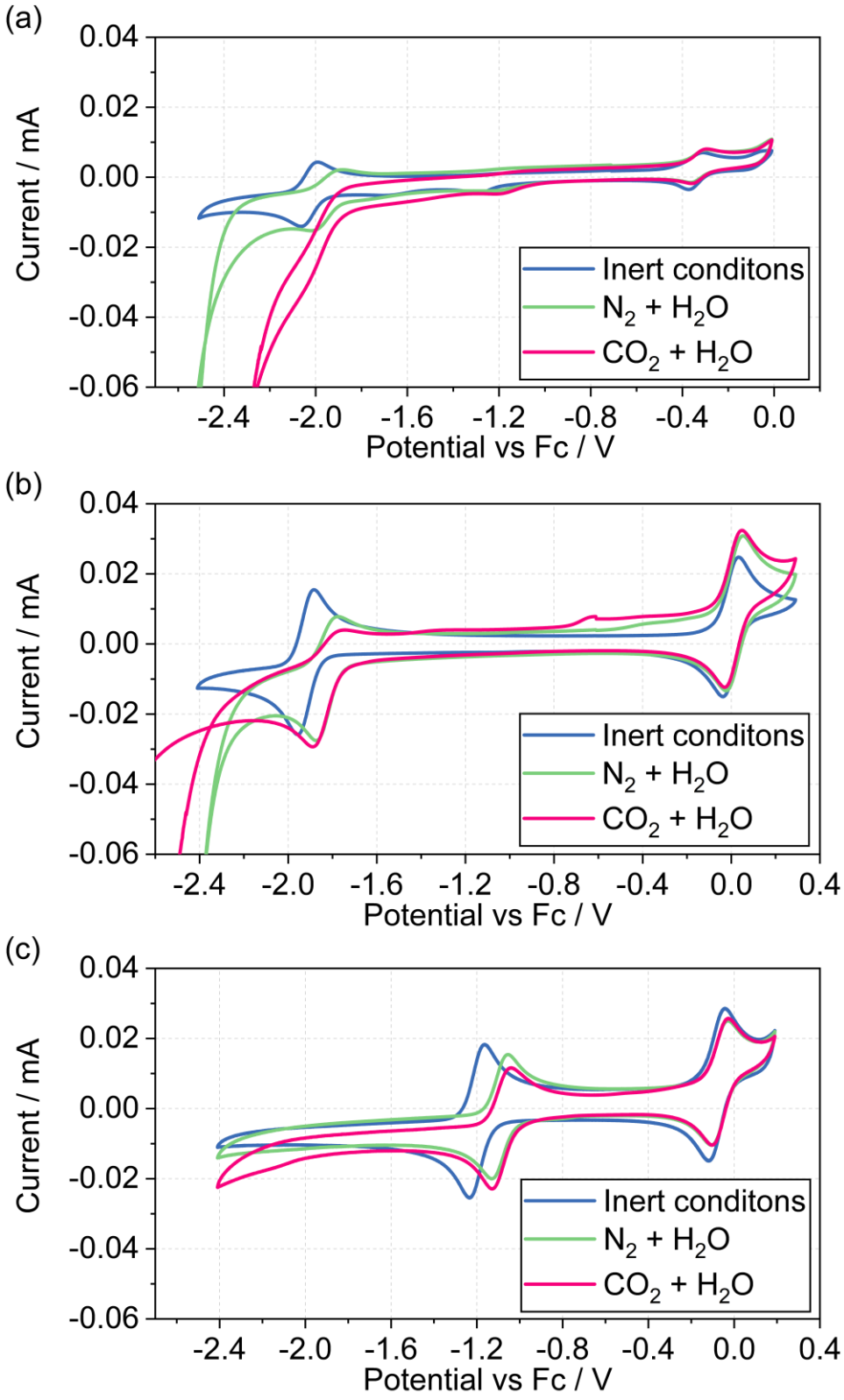

Figure 3.4 *Cyclic voltammetry of a) 0.5 mM $(Et_4N)_2$**[Co**$(mnt)_2$**]**, b) 1 mM $(Et_4N)_2$**[Ni**$(mnt)_2$**]** and c) 1 mM $(Et_4N)_2$**[Cu**$(mnt)_2$**]** in 100 mM $TBAPF_6$ MeCN electrolyte, under different conditions. Hydrous electrolytes were prepared by addition of 1 mL of H_2O to 10 mL electrolytes causing dilution of the complexes to 0.45, 0.91 and 0.91 mM, respectively, and $TBAPF_6$ dilution to 91 mM. Second scans shown at 100 mV s^{-1}.*

3.3.2 Voltammetric Characterisation of Fe mnt

Although the $Fe(mnt)_2^{1-}$ complex was first reported over 50 years ago, its electrochemistry has been essentially unreported. The complex was only briefly characterised in the previously mentioned work of Yamaguchi et al. in 2009 before the work reported by previous group members in 2019. Therefore, a more thorough voltammetric investigation was conducted here to characterise its behaviour in MeCN.

As previously reported, under inert conditions the as synthesised anionic $Fe(mnt)_2^{1-}$ species undergoes two sequential one-electron reductions to the trianionic $Fe(mnt)_2^{3-}$ oxidation state at −0.69 and −2.11 V vs Fc as shown in Figure 3.5. At potentials above 0 V vs Fc, the complex displays a large oxidation peak at 0.46 V. This lacks a symmetrical reduction peak in the expected potential range and instead a broad reduction peak is observed at −0.1 V vs Fc. This is most likely oxidative decomposition of the complex caused dissociation of the dithiolene ligands and formation of an unknown Fe(III) species.

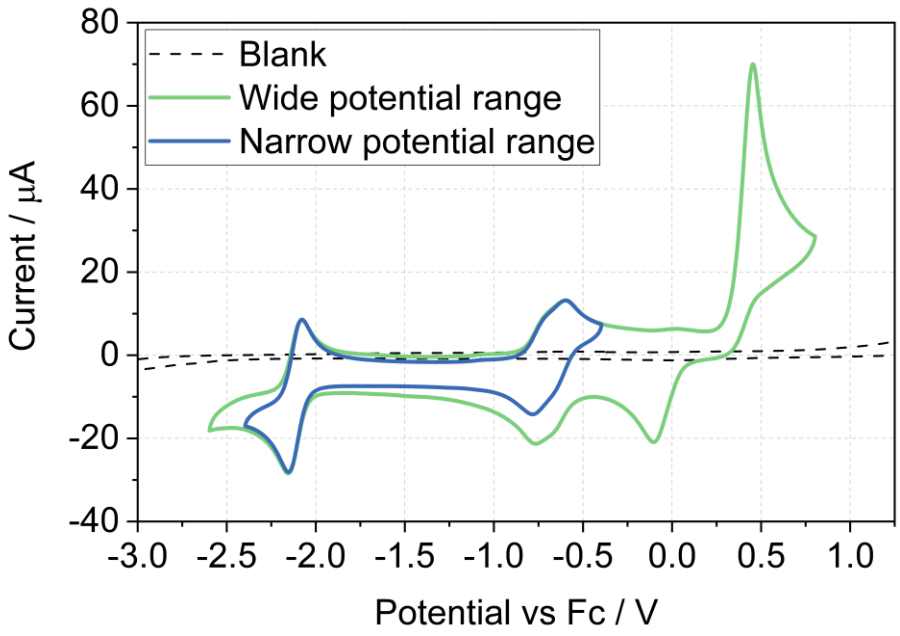

Figure 3.5 *Cyclic voltammetry of Fe mnt at a GC electrode under N_2 and in the absence of a proton source (100 mV s^{-1}, second scans shown). (a) Behaviour of $Fe(mnt)_2^{1-}$ over a range of applied potentials. (b) Peak deconvolution of the $Fe(mnt)_2^{1-/2-}$ redox couple into two diffusion-limited redox couples. The electrolyte was composed of 1 mM $(Et_4N)[Fe(mnt)_2]$ with 100 mM $TBAPF_6$ supporting electrolyte in MeCN solvent.*

Scan rate analysis was performed by Dr Craig Armstrong. The $Fe(mnt)_2^{2-/3-}$ redox couple at −2.11 V vs Fc gave a high peak current ratio around 90% and a peak-to-peak separation of 77 mV at a scan rate of 100 mV s^{-1}, with a modest increase to 100 mV at 1 V s^{-1}, indicating quasi-reversible kinetics. In contrast, the $Fe(mnt)_2^{1-/2-}$ couple shows more complicated voltammetry, illustrated in Figure 3.6. While peak separation ranged from 181 mV at 100 mV s^{-1} to 199 at 1 V s^{-1} suggesting irreversible kinetics, the current ratio remained around 90%. A closer look at the waveform reveals shoulders on the current peaks. It was proposed that this abnormal feature was a result of two convoluted couples rather than a single irreversible one. Peak deconvolution (seen in Figure 3. 6) suggested two consecutive reductions centred at −0.62 and −0.74 V vs Fc respectively, of comparable magnitude and reversibility. The integration of these combined peaks totalled to a comparable charge to the reduction centred at −2.11 V vs Fc, indicated the number of electrons transferred is equivalent and both processes are overall one electron reductions.

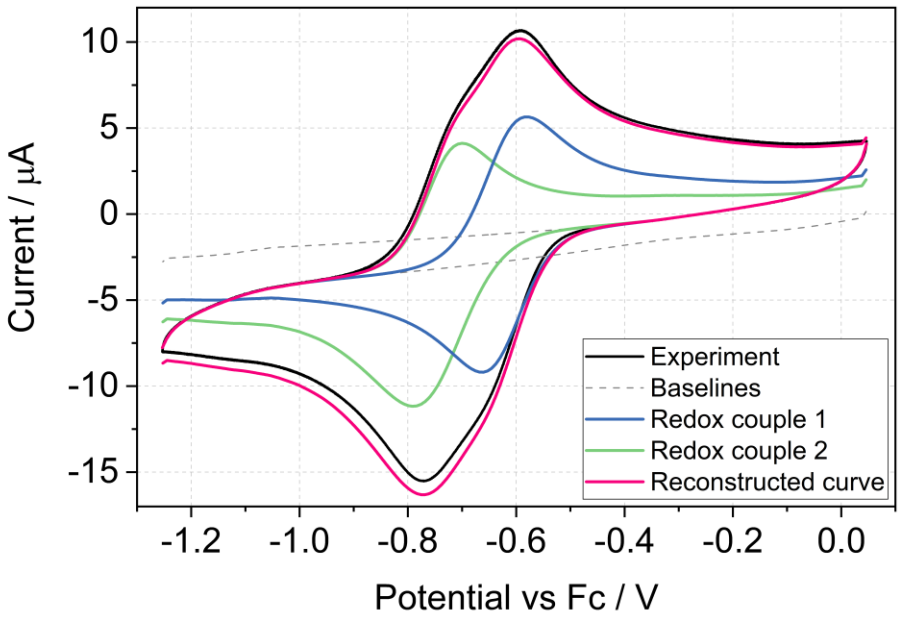

Figure 3.6 *Cyclic voltammetry of the $Fe(mnt)_2^{1-/2-}$ redox couple (black) at 100 mV s^{-1} at a GC electrode, under N_2 (second scan shown). Peak deconvolution analysis (performed by Dr Craig Armstrong) of the voltammogram into two diffusion-limited redox couples is shown. The reconstructed curve is also given as a comparison to the experimental data for quality indication. The electrolyte was composed of 1 mM $(Et_4N)[Fe(mnt)_2]$ with 100 mM $TBAPF_6$ supporting electrolyte in MeCN solvent.*

To account for this, we proposed that when dissolved in acetonitrile the Fe mnt complex exists as a dimer akin to the structure observed when in solid phase. Initially, the

$Fe_2(mnt)_4^{2-}$ dimer is reduced by a single electron to a trianionic $Fe_2(mnt)_4^{3-}$ species. This is followed by rapid dissociation of the dimer, yielding both an $Fe(mnt)_2^{2-}$ and $Fe(mnt)_2^{1-}$ species. The unreduced monomer species in then reduced at the slightly more negative potential. Because this equates to one electron per iron atom, electron stoichiometry is conserved. Overall, the proposed reactions are;

Redox couple 1:

$$[\mathrm{Fe_2(mnt)_4}]^{2-} + \mathrm{e^-} \rightleftarrows [\mathrm{Fe_2(mnt)_4}]^{3-}$$

Dimerization/dissociation:

$$[\mathrm{Fe_2(mnt)_4}]^{3-} \rightleftharpoons [\mathrm{Fe(mnt)_2}]^{2-} + [\mathrm{Fe(mnt)_2}]^{1-}$$

Redox couple 2:

$$[\mathrm{Fe(mnt)_2}]^{1-} + \mathrm{e^-} \rightleftarrows [\mathrm{Fe(mnt)_2}]^{2-}$$

Overall:

$$[\mathrm{Fe_2(mnt)_4}]^{2-} + 2\mathrm{e^-} \rightleftarrows 2\,[\mathrm{Fe(mnt)_2}]^{2-}$$

Interestingly, when dissolved in a concentrated hydrous electrolyte (5 M H_2O), the two-couple waveform is replaced by a single redox couple centred at −0.70 V vs Fc with a comparatively smaller peak separation of 128 mV at 100 mV s^{-1}. This would suggest that the presence of water coordinated with the complex results to favour dissociation of the dimer resulting in only one redox couple being observed. Conversely, the presence of 5 M 2,2,2-trifluoroethanol (TFE) as an anhydrous proton source (discussed in detail later) further increases the potential separation between these two events.

To investigate this further, voltammetry using different supporting electrolytes was conducted in the absence of any proton source (Figure 3. 8). The use of highly coordinating halide anions caused the $Fe(mnt)_2^{1-/2-}$ waveform to revert to a classical quasi-reversible redox couple exhibiting a small peak separation of 72 mV and accompanied a negative shift of ~100 mV. This result indicates coordination of halide ligands causes a similar shift of the equilibrium towards full dissociation of the dimer as seen in hydrous electrolyte. The presence of perchlorate anions resulted in the same waveform observed as observed for hexafluorophosphate, while tetrafluoroborate resulted in a similar broad waveform but absent of any shoulder peaks.

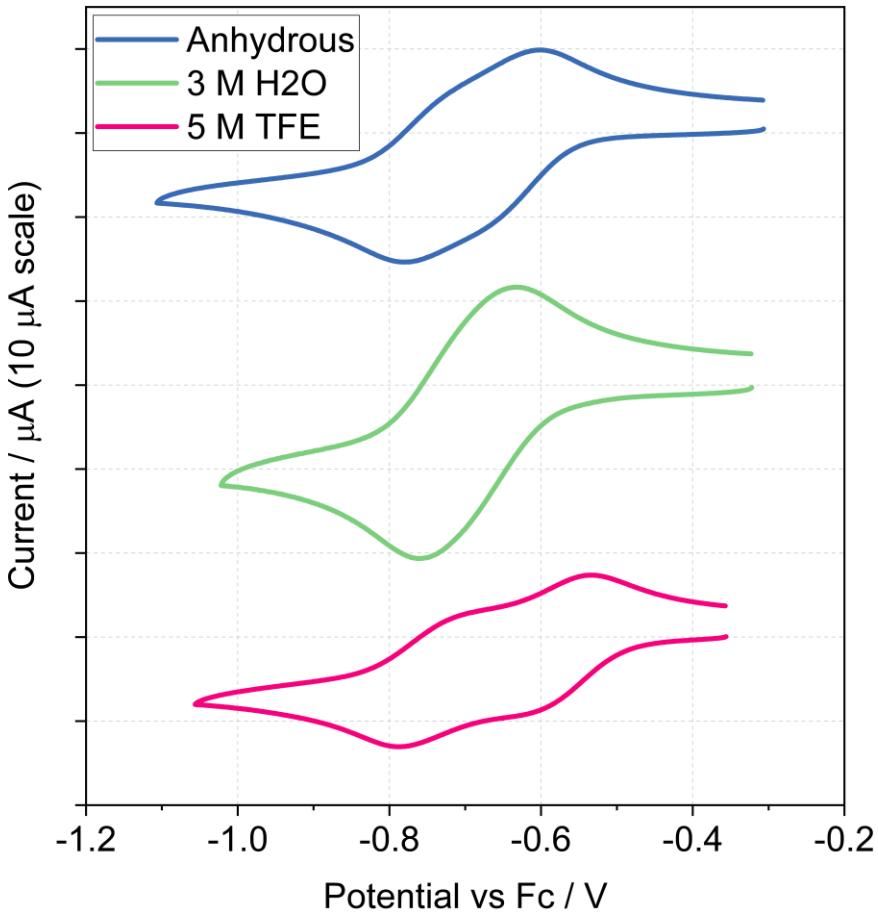

Figure 3.7 *Cyclic voltammetry of the $Fe(mnt)_2^{1-/2-}$ redox couple at 100 mV s^{-1} at a GC electrode, under N_2 (first scan shown). An anhydrous electrolyte is compared to one containing 5 M H_2O and one containing 5 M TFE. The electrolyte was composed of 1 mM $(Et_4N)[Fe(mnt)_2]$ with 100 mM $TBAPF_6$ supporting electrolyte in MeCN solvent.*

The electronic structure of the $Fe(mnt)_2$ in these solvation environments was then probed using UV/vis spectroscopy. It was found that in all electrolytes examined the iron dithiolene solution showed high intensity bands in the UV region corresponding to spin-allowed intraligand (π-π*) transitions (Figure 3. 9, 3. 10), which are commonly reported to have extinction coefficients in the 10^3 range. A lower energy peak at 450 nm was also observed for the anhydrous MeCN and in the presence of 5 M TFE, the latter being more intense. However, in the presence of 5 M H_2O or with highly coordinating halide ions, the peak at 450 nm splits into two broader peaks either side of 450 nm with much lower intensity. Evidently, there is significant change in the electronic structure associated with dissociation of the dimer in solution.

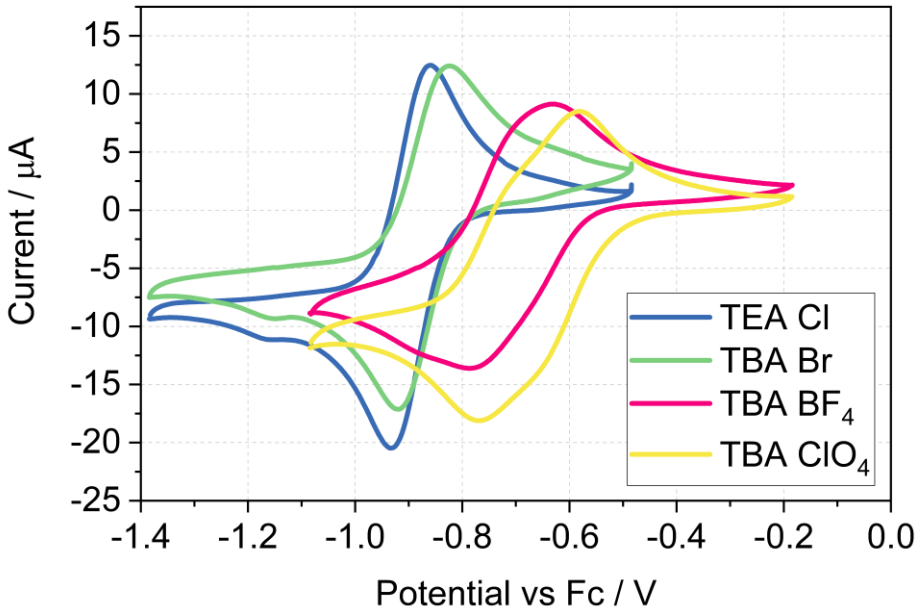

Figure 3.8 *Cyclic voltammetry of $Fe(mnt)_2^{1-}$ as a function of electrolyte composition under N_2 at a GC electrode. The electrolytes were composed of 1 mM $(Et_4N)[Fe(mnt)_2]$ with 0.1 M supporting electrolyte in MeCN. Second scans shown at 100 mV s^{-1}.*

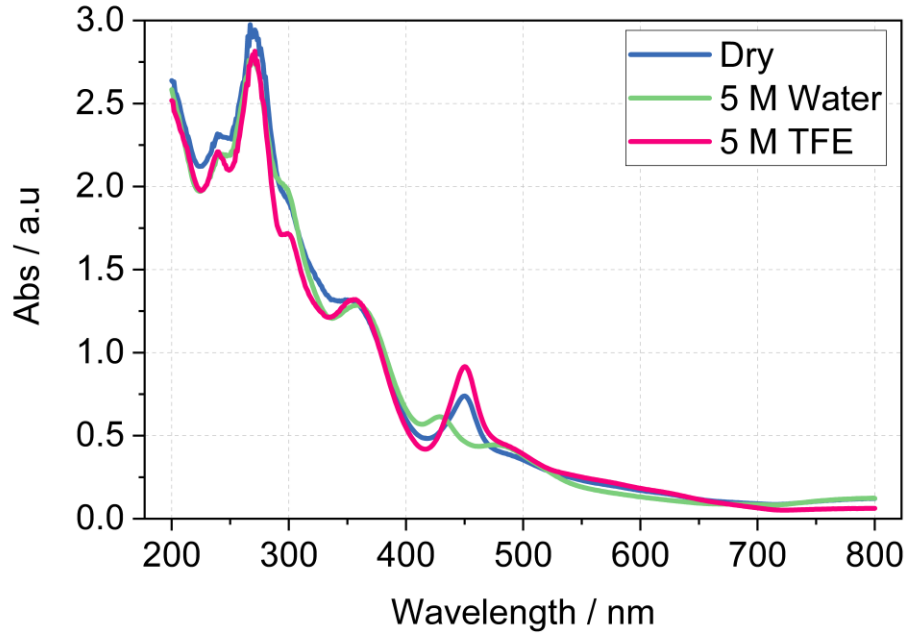

Figure 3.9 *Room temperature UV/Vis spectra of 1 mM $(Et_4N)[Fe(mnt)_2]$ with 100 mM $TBAPF_6$ in MeCN with no proton source, 5 M water, and 5 M TFE respectively.*

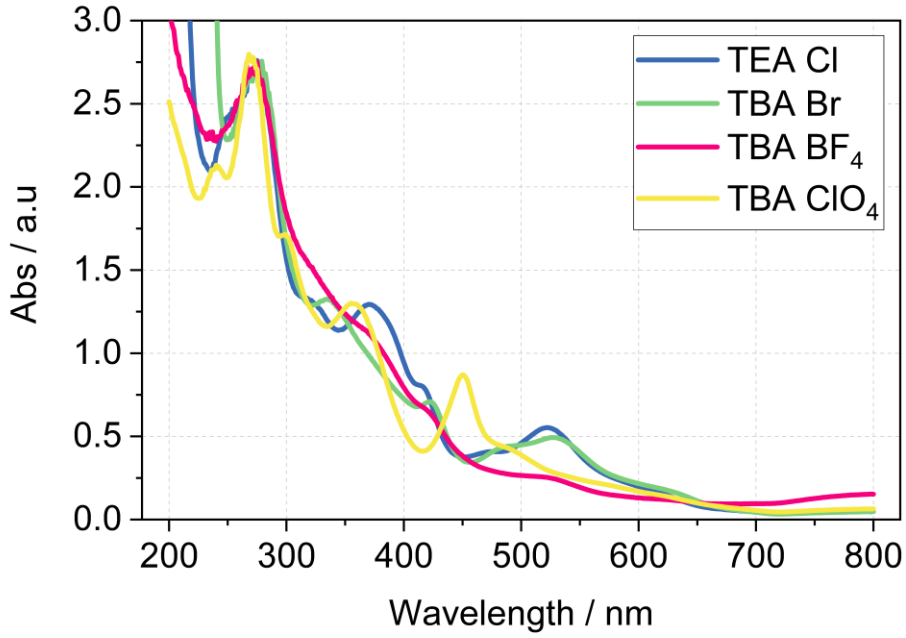

Figure 3.10 *Room temperature UV/Vis spectra of 1 mM $(Et_4N)[Fe(mnt)_2]$ with varying supporting electrolytes Et_4NCl, TBABr, $TBABF_4$ and $TBAClO_4$ respectively at 100 mM concentration in MeCN.*

3.3.3 Electrocatalytic Activity

Beyond this varied redox chemistry noted for the first reduction of the mnt complex, the true interest lies in the catalytic response to CO_2 in the presence of a proton source highlighted in Figure 3.3. As mentioned, the loss of reversibility and an order of magnitude increase in current highlight the occurrence of a homogeneous catalytic process. This is attributed to electrocatalytic CO_2R whereby the reduced $Fe(mnt)_2^{3-}$ species is rapidly chemically oxidised by dissolved CO_2 and reduced again within the interface, which results in a peak limited by CO_2 diffusion and catalytic turnover rather than $Fe(mnt)_2$ diffusion. The solubility of CO_2 in the MeCN-based electrolyte is approximately 0.3 M and far exceeds the catalyst concentration.[26] By examining the current response under N_2, the onset of HER at the electrode is observed beyond −2.25 V vs Fc. Therefore, a favourably high HER overpotential of approximately 300 mV exists under these conditions. This suggests that electrolysis conducted between −1.9 and −2.2 V vs Fc should display high selectivity towards CO_2R products and produce minimal quantities of H_2.

A brief study into the effects of water concentration was conducted to observe its contribution to the catalytic process. It was observed that even a small amount of water, 0.27 M, in the magnitude of the expected CO_2 concentration, enabled a catalytic

current. The catalytic current continued to increase until a water concentration of 5 M was reached, after which it appeared to plateau. Concentrations above this saw no further increase, indicating that proton availability plays a key role in the rate of reaction at least up to a certain point. For this reason, proton concentrations of at least 3 M were used in electrolysis experiments.

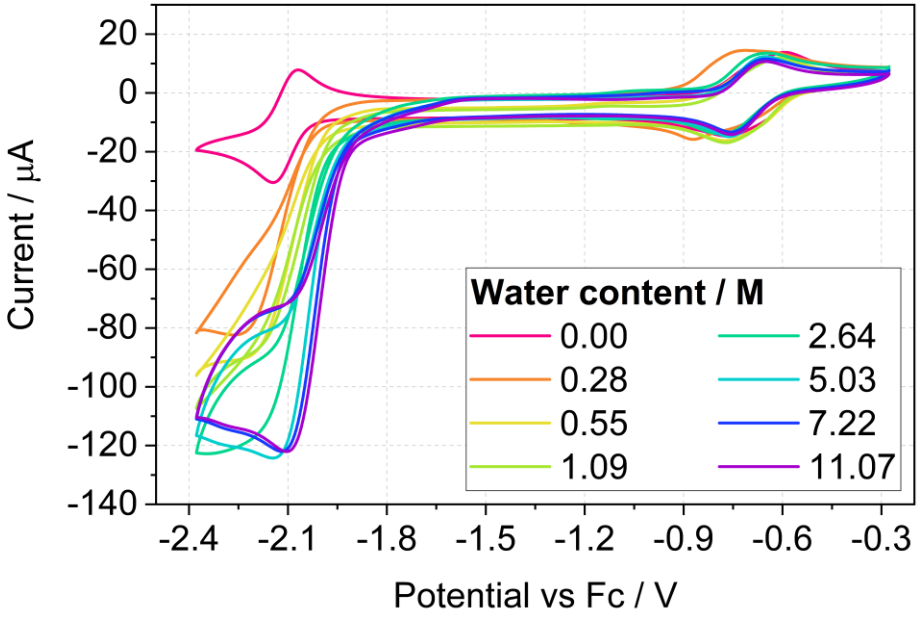

Figure 3.11 *Cyclic voltammetry of Fe mnt as a function of water content at a GC electrode under CO_2. Second scans shown at 100 mV s^{-1}. Water was added sequentially by use of a volumetric pipette resulting in partial dilution of the Fe mnt, which has been normalised in the current response.*

The catalytic activity of $Fe(mnt)_2$ was also studied using TFE which possesses a relatively low pKa of 12.46 compared to water and other alcohols. The acidic proton of TFE is significantly dissociated and therefore highly labile for protonation of catalytic intermediates. As such it is a relatively popular choice as an anhydrous proton source for CO_2R. Figures 3. 13 and 3. 14 show the HER and CO_2R catalysis in the presence of TFE across a range of concentrations. Using 0.1 and 0.5 M TFE in the absence of CO_2, the catalyst appears to behave very similarly to that observed when 5 and 10 M water are used respectively. Further increase to 1 and 5 M TFE resulted in HER onset before the second reduction of the complex, obscuring it from the voltammetry.

Upon saturating the solution with CO_2, the voltammetry in the presence of 0.1 M TFE again resembles the voltammetry when 5 M water is present. Increasing to 0.5 M TFE resulted in a modest increase in peak current and a slight positive shift in the onset of

the reduction wave. For the 1 and 5 M TFE cases, the onset of the catalytic reaction shifted further positive and the peak current continued to increase. However, the competing HER also increased in current and shifted more positive, beginning to overlap with the CO_2R peak. For this reason, TFE concentrations of ≤0.5 M appear most suitable for mitigating the HER.

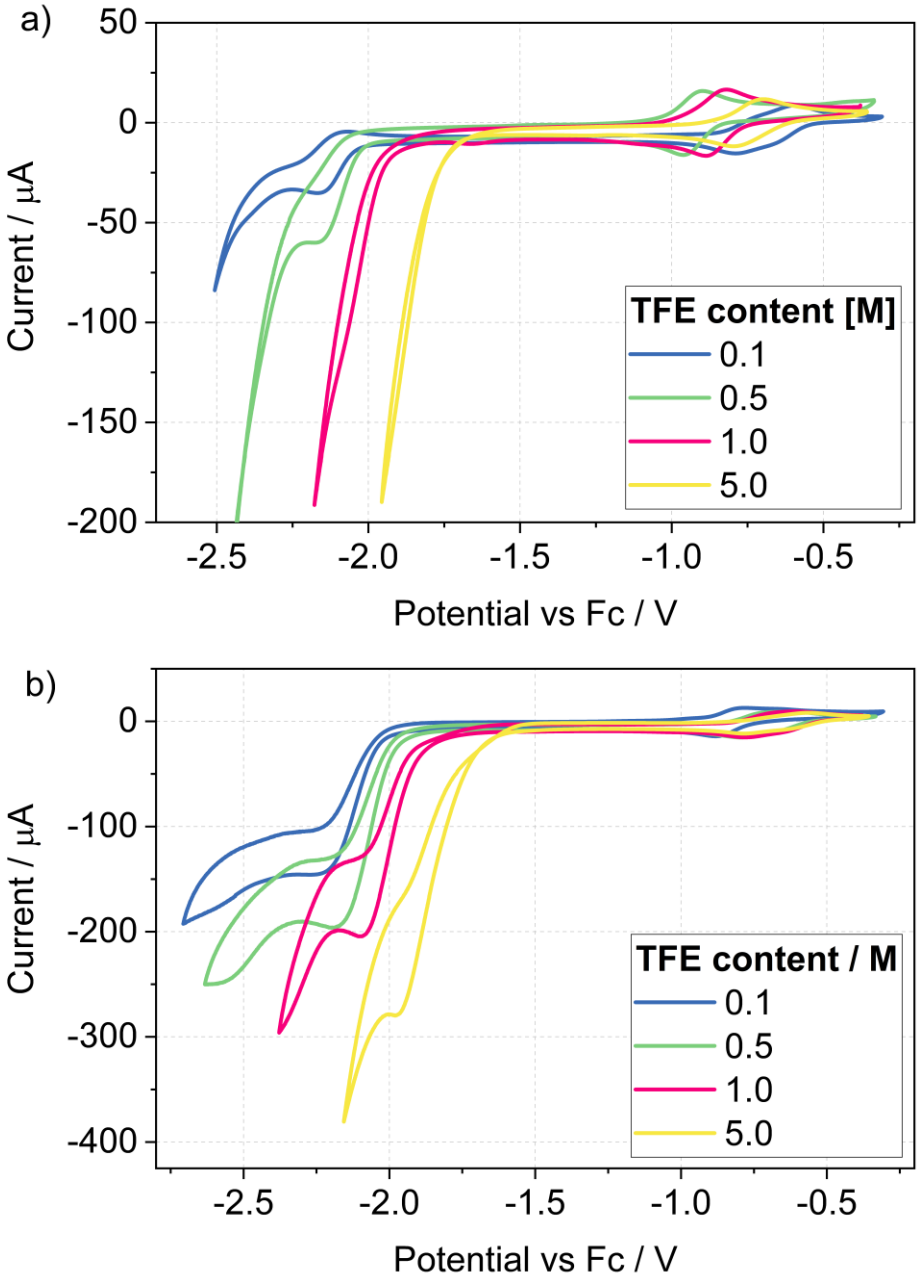

Figure 3.12 *Cyclic voltammetry of $Fe(mnt)_2^{1-}$ as a function of 2,2,2-triflouroethanol content at a GC electrode under a) N_2 and b) CO_2. Second scans shown at 100 mV s^{-1}. Each solution consisted of 1 mM $Fe(mnt)_2^{1-}$ with 100 mM $TBAPF_6$ in MeCN.*

To benchmark the potential catalytic performance of the $Fe(mnt)_2$ complex, cyclic voltammetry of the system was analysed using the approach outlined by Costentin and Savéant.[27,28] This method determines the performance of molecular electrocatalysts by means of a modified Tafel analysis that evaluates the voltammetric electrocatalytic response. It was selected as a means to get a maximum turn over frequency (TOF_{max}) for the complex independent of cell geometry and reaction conditions that normally influence bulk electrolysis studies. The technique accounts for the fact that the catalytic reaction rapidly turns over the complex at the electrode interface, rather than engaging all of the catalyst dissolved in the solution.

Here, the reaction pathway is assumed to be that of an EECC mechanism, as the catalytic wave is observed upon the second reduction while the first reduction remains reversible in the presence of substrate, yet both reductions are necessary to achieve the two-electron reduction of the CO_2. Ideally, the catalytic wave would exhibit a superimposed S-shaped trace that is independent of scan rate, however it is common for side phenomena to add diffusion limited character. Figure 3. 13 shows the scan rate analysis of the Fe dithiolene in an MeCN solution saturated with CO_2 in the presence of 0.1 M TFE as a proton source. At high scan rates diffusion limited peak shaped character dominated the trace, while at low scan rates the trace coalesced towards an S-shaped wave. This implies the catalytic reaction kinetics are moderate, such that at a high scan rate the character is limited by the diffusion of the dithiolene complex, CO_2 or proton source, but at slower scan rates a steady-state response is observed. Due to

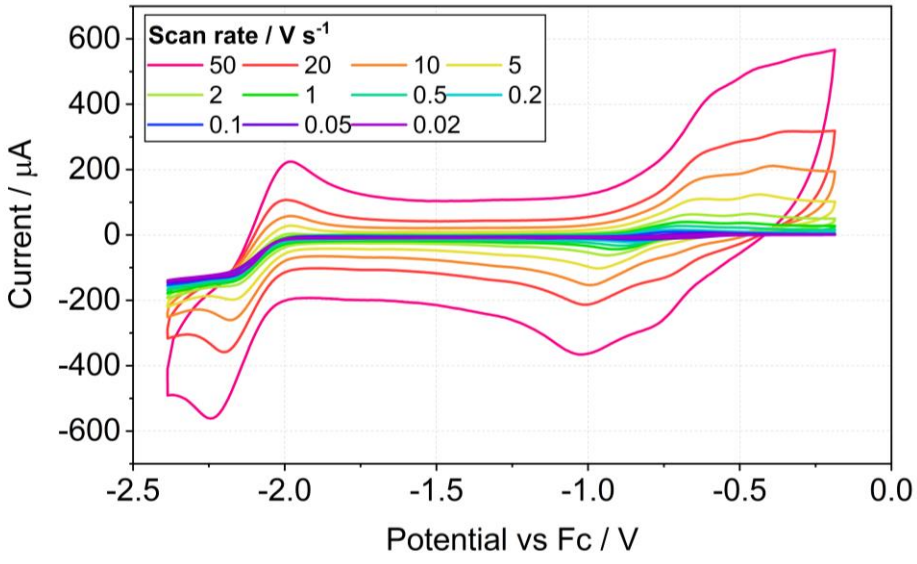

Figure 3.13 *Scan rate dependence of $Fe(mnt)_2$ at a GC electrode under CO_2 with TFE proton source. The electrolyte was composed of 1 mM $(Et_4N)[Fe(mnt)_2]$ with 0.1 M TFE and 100 mM $TBAPF_6$ in MeCN. Scan rate was varied between 50 and 0.02 V s^{-1}.*

the overlap of the HER and CO_2R processes a meaningful current plateau could not be obtained, so foot of the wave analysis (FOWA) was used to estimate the TOF_{max}.

FOWA is performed using Equation 1 by plotting the diffusion normalised current against 1 / (1 + exp[f(E−$E_{1/2}$)]) such that the gradient of this line can be used to determine k, which is equal to the TOF_{max} under these conditions.[29] As with Tafel analysis, only the gradient of the initial linear portion of the line should be used to estimate the TOF_{max}, where side phenomena including mass transport limitation are assumed to be negligible. Using this value, it is then possible to determine the TOF at zero overpotential (TOF_0) so that the performance of the catalyst can be compared fairly with other catalysts. However, this requires determining the standard potential for the specific reaction taking place, and as a transient method cyclic voltammetry offers little insight into the product(s) of the reduction and so does not entirely avoid the need for bulk electrolysis.

$$\frac{i}{i_p} = \frac{2.24 n_c \sqrt{\frac{k}{fv}}}{1+\exp\left[f\left(E-E_{\frac{1}{2}}\right)\right]} \quad (1)$$

Applying this methodology to data from cyclic voltammetry performed on a solution of 1 mM $Fe(mnt)_2$ with 0.1 M TFE and 0.3 M CO_2 at a scan rate of 0.1 V s^{-1} yields a TOF_{max} of 21.7 s^{-1}.[26] This value is of course specific to the exact reaction conditions. The rate constant k is the overall rate constant for the reduction reaction(s) and cannot be deconvoluted from the substrate concentration without knowing its involvement in the rate limiting step. This is compounded when multiple products are created, each with their own rate limiting step. A relatively low turnover frequency would explain why diffusion character dominates the CV at fast scan rates, as on these timescales only a small portion of the current is provided by catalytic cycling. A catalyst with a high turnover frequency, such as the widely reported Fe-porphyrin complexes, would possess a TOF_{max} of magnitude 10^4 s^{-1}.[10]

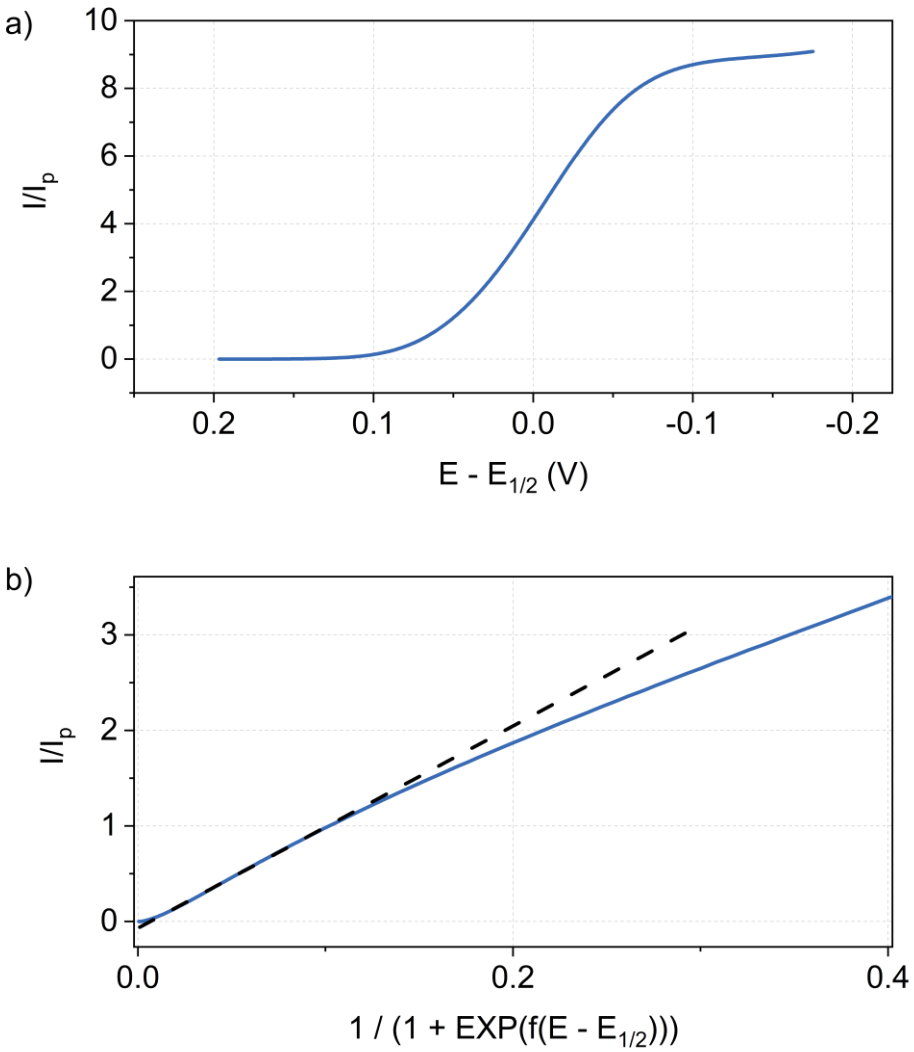

Figure 3.14 *a) Plot of the diffusion normalised peak current I/I_p vs $E - E_{1/2}$ calculated from the reduction wave of a cyclic voltammogram of CO_2 saturated 1 mM $(Et_4N)[Fe(mnt)_2]$ with 0.1 M TFE and 100 mM $TBAPF_6$ in MeCN taken at 0.1 V s^{-1}, where I_p is the diffusion limited peak current of a one-electron reduction wave of the same complex at the same scan rate under reversible conditions. b) Plot of the diffusion normalised peak current I/I_p vs $1 / (1 + EXP[f(E - E_{1/2})])$ for the system described in Figure S 21 for use in front of wave analysis. The gradient of the initial linear portion (dashed black line) can be used to determine the TOF_{max} using equation 1 as discussed in the main text.*

3.3.4 CO_2 Electrolysis Studies

To determine the products the Fe mnt catalysed CO_2R, a series of bulk electrolysis experiments were performed by Dr Craig Armstrong. Experiments were conducted on a charge passed basis of 100 C to ensure a detectable level of products, as well as to make the turnover of catalyst molecules comparable between experiments. The area of the working electrode was adjusted such that the currents were comparable, and

that each experiment took around 1.5 to 2 hours. Both 3 M water and 0.1 M TFE were explored as proton sources for the bulk electrolysis, with applied potentials of −2.36 and −2.25 V vs Fc respectively.

As the Fe mnt complex is expected to provide two-electrons per molecule for driving catalytic reactions, it was expected that only the two-electron products H_2, CO and HCOO(H) would be generated. However, the possibility of further-reduced products was not immediately ruled out. Product yields were quantified by gas chromatography and liquid phase H^1NMR. Ultimately, only H_2, CO and HCOO(H) were detected, whereas other hydrocarbons were not observed. The yields of these products are shown in Figure 3. 15, which compares both proton sources. In each case, electrolysis experiments gave low yields such that the total quantified faradaic efficiency was only 24 ± 5 % and 47 ± 4 % for H_2O and TFE respectively. Evidently, the majority of charge passed remained unaccounted.

Both proton sources favoured H_2 production over CO production. This was despite the applied potentials being chosen to avoid HER as much as possible by observing the onset potentials in the preceding voltammetry. It is therefore evident that $Fe(mnt)_2$ is an effective catalyst for HER, as noted previously.[25] Indeed, by running control experiments in the absence of CO_2, higher H_2 yields of 31 and 23 % for H_2O and TFE respectively were observed. More notable however was that using TFE as a proton source resulted in HCOO(H) as the major product at 38% yield (81% selectivity), while only a trace was produced when using water as the proton source.

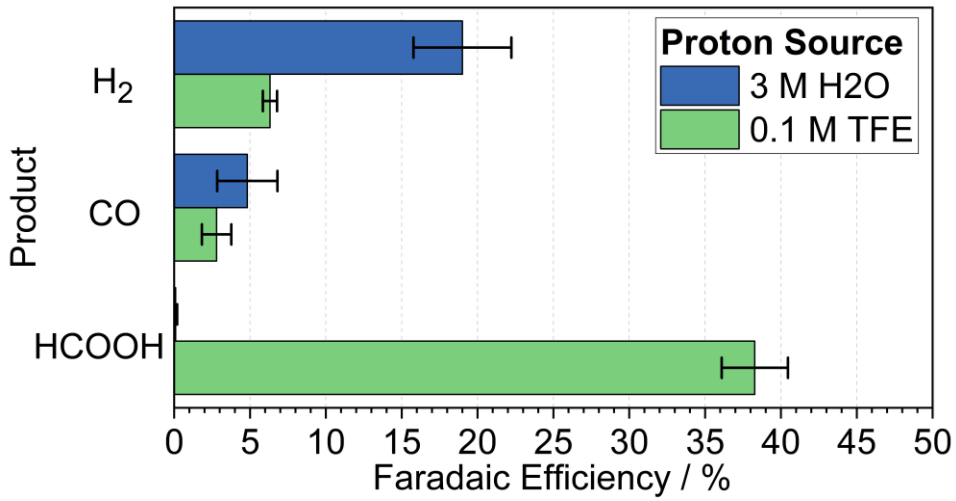

Figure 3.15 *Faradaic efficiencies of CO_2R products from electrolysis experiments using 3 M H_2O and 100 mM TFE as proton sources. Each bar represents the mean yield of the triplicate experiment. The standard deviation of each mean result is represented by error bars.*

This selectivity towards CHOO(H) when using TFE was also observed by Fogeron *et al.* for the analogous nickel molybdopterin-like dithiolene complex.[19] Here they recorded CHOO(H) yields of 60, 30, 15 and 18 % for solutions containing TFE, H_2O, methanol, and phenol, respectively. Their work showed that the product distribution was very dependent on the electrolyte acidity, which suggests that careful control of the reaction conditions my allow for improvements in both selectivity towards CO_2R products and overall yield.

3.3.5 Catalyst Stability

Over the course of the work, it was noticed that solutions of Fe mnt were prone to degradation under ambient conditions. This was most notable for the hydrous samples used in bulk electrolysis, which would degrade in only a few days. Anhydrous samples were more stable, however even these gave a degraded electrochemical response after just a few weeks. By comparison, anhydrous solutions stored in a nitrogen glove box displayed minimal degradation after more than six months. This indicated that exposure to both water and oxygen resulted in degradation of the Fe mnt complex.

Long duration voltammetry experiments (100 scans, ~1 h duration) displayed minimal degradation of the current response under both inert and catalytic conditions. These results suggest that degradation is not a result of electrochemical instability, at least on the timescale of transient voltammetry. Despite this, electrolyte degradation during CO_2R electrolysis was evident for both proton sources after the 2 h bulk electrolysis experiments. Electrolyte discolouration was observed for both protons sources, coupled with a gradual decrease in current response over the course of the experiments and the formation of precipitate. Evidently, the catalyst is not fully stable under electrolysis conditions, which is likely the result of irreversible oxidation pathways by reaction with other components of the electrolyte, including reactions with other Fe mnt molecules, water, or trace O_2. These parasitic and destructive reaction pathways are the likely cause of the relatively poor faradaic efficiency reported, where large amounts of charge are lost to this degradation.

3.3.6 Mechanistic Insights

Drawing inspiration from the existing literature, a series of mechanisms were proposed following a computational modelling study performed by Dr Craig Armstrong in conjunction with the research group of Dr Andrew Kerridge. Density functional theory calculations were employed to predict the likely reactions pathways using a lowest energy method. The conclusions of this work are discussed briefly as they pertain to

the experimentally observed reactivity. A more detailed description of how the modelling supports these conclusions can be found within the paper.

The likely pathways for the production of H_2, CO and HCOO(H) are proposed as seen in Figure 3.16. The initiation of the catalyst for all reaction pathways was considered to be two sequential one-electron reductions as shown in the preceding voltammetry. This activated state can then bind with either CO_2 or a proton to form the first reaction intermediate. The proton bound intermediate is thought to be the first step in the formation of both H_2 and HCOO(H), depending on whether it then reacts with either a further proton or CO_2. Binding with a second proton allows formation of a H−H bond and release of H_2, while hydride insertion into a CO_2 molecule results in the formation of $HCOO^-$. For the CO_2 bound intermediate, it is believed that two sequential protonations, first forming a carboxylate ligand, then resulting in C−O bond cleavage and the release of H_2O, produce a bound carbonyl ligand which is then released.

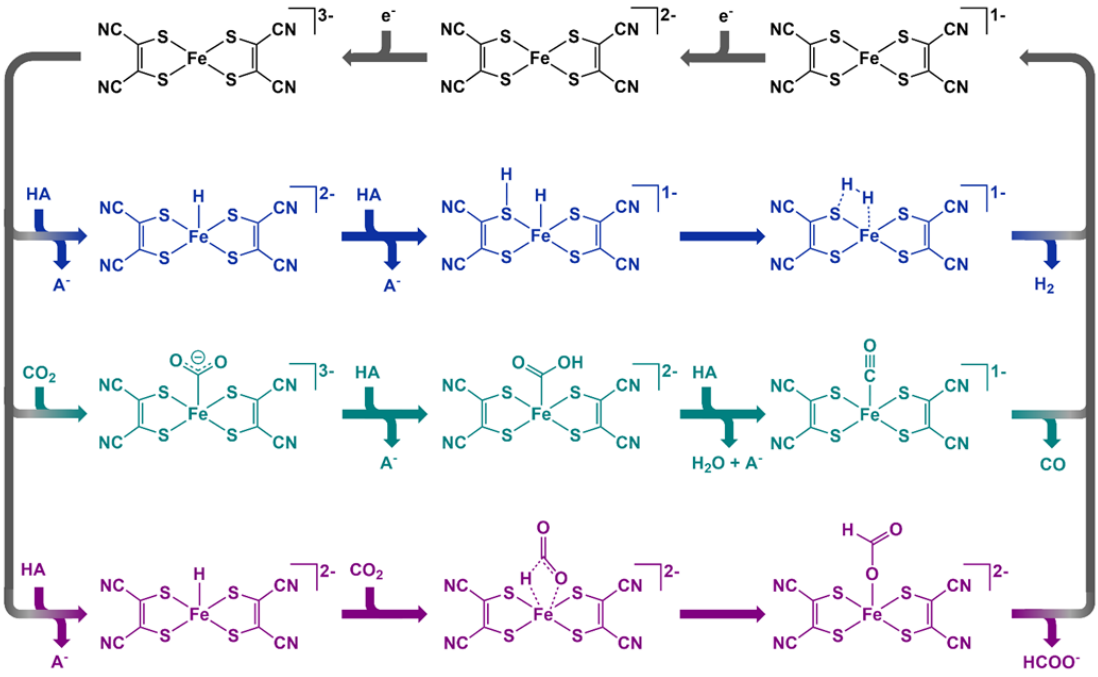

Figure 3.16 *Proposed reaction mechanisms for the production of (blue) H_2, (green) CO and (purple) $CHOO^-$. HA represents a generic proton source such as H_2O or TFE. Reproduced from Ref 1 under creative commons licence CC BY 4.0.*

3.4 Conclusions

This work presented herein has demonstrated the use of the dithiolene complex $Fe(mnt)_2$ as a homogeneous electrocatalyst for CO_2R in a simple MeCN-based electrolyte for the first time. Despite the role of iron-sulphur coordination complexes in CO_2R chemistry demonstrated in the natural world, very little research has been published thus far. The complex was fully voltammetrically characterised in the absence and presence of CO_2 and proton sources. Results indicated complex interactions of the catalyst with differing electrolyte components via coordination at the Fe-S core. Indeed, we identify interesting split-peak redox behaviour which we attribute to the existence of the dimeric $[Fe_2(mnt)_4]^{2-}$ species in solution. The prevalence of this dimer appears suppressed during catalysis, however, due to catalyst protonation and CO_2-adduct formation.

During electrolysis, the complex was only observed to produce two-electron reduction products; H_2, CO and HCOO(H). Comparing water and TFE as proton sources, the selectivity and performance was markedly different, with the catalyst displaying a comparatively higher selectivity towards HCOO(H) production when using TFE, whereas none was observed in the presence of water. DFT modelling was used to propose a catalytic mechanism, wherein the formation of an initial hydride species was identified as critical in the production of HCOO(H). The importance of proton availability in determining the reaction pathway suggests that fine tuning of the solution pH may lead to further improvement in the selectivity towards HCOO(H).

While the exploration of this novel chemistry provides an interesting contribution the existing literature, from the perspective of the overarching goal of this work to enable $DECO_2R$, mixed conclusions can be drawn. The relatively poor performance and stability of this catalyst suggests it would be difficult to find a suitable redox mediator with which to pair it. The complicated relationship between product selectivity and pH observed would likely be further impacted by the presence of another redox active species. Rather than continuing to chase novel chemistries, it was decided to concentrate on adapting previously reported catalyst materials as a starting point for determining if $DECO_2R$ is achievable. The inefficiency of CO_2R in organic solvents in general is considered unfavourable, resulting in the need for a large overpotential to drive the reaction. As such further exploration to find suitable mediators was focussed exclusively on aqueous systems.

3.5 References

1 C. G. Armstrong, M. Potter, T. Malcomson, R. W. Hogue, S. M. Armstrong, A. Kerridge and K. E. Toghill, *ChemElectroChem*, 2022, **9**, e202200610.

2 R. W. Hogue, C. G. Armstrong and K. E. Toghill, *ChemSusChem*, 2019, **12**, 4506–4515.

3 R. Francke, B. Schille and M. Roemelt, *Chem. Rev.*, 2018, **118**, 4631–4701.

4 S. Sinha, A. Sonea, W. Shen, S. S. Hanson and J. J. Warren, *Inorg. Chem.*, 2019, **58**, 10454–10461.

5 S. A. Roell, B. R. Schrage, C. J. Ziegler and T. A. White, *Inorganica Chim. Acta*, 2020, **503**, 119397.

6 S. E. Witt, T. A. White, Z. Li, K. R. Dunbar and C. Turro, *Chem. Commun.*, 2016, **52**, 12175–12178.

7 M. Daryanavard, H. Hadadzadeh, M. Weil and H. Farrokhpour, *J. CO2 Util.*, 2017, **17**, 80–89.

8 D. Ghosh, K. Kobayashi, T. Kajiwara, S. Kitagawa and K. Tanaka, *Inorg. Chem.*, 2017, **56**, 11066–11073.

9 M. Hammouche, D. Lexa, J. M. Savéant and M. Momenteau, *J. Electroanal. Chem. Interfacial Electrochem.*, 1988, **249**, 347–351.

10 C. Costentin, G. Passard, M. Robert and J. M. Savéant, *Proc. Natl. Acad. Sci. U. S. A.*, 2014, **111**, 14990–14994.

11 J. Shen, R. Kortlever, R. Kas, Y. Y. Birdja, O. Diaz-Morales, Y. Kwon, I. Ledezma-Yanez, K. J. P. Schouten, G. Mul and M. T. M. Koper, *Nat. Commun.*, DOI:10.1038/ncomms9177.

12 A. Call, M. Cibian, K. Yamamoto, T. Nakazono, K. Yamauchi and K. Sakai, *ACS Catal.*, 2019, **9**, 4867–4874.

13 J. D. Froehlich and C. P. Kubiak, *Inorg. Chem.*, 2012, **51**, 3932–3934.

14 J. Song, E. L. Klein, F. Neese and S. Ye, *Inorg. Chem.*, 2014, **53**, 7500–7507.

15 A. Sinopoli, N. T. La Porte, J. F. Martinez, M. R. Wasielewski and M. Sohail, *Coord. Chem. Rev.*, 2018, **365**, 60–74.

16 P. Krzyszowska and E. Pacholska-dudziak, *Nat. Chem.*, 2025, **7563**, 0–1.

17 R. Eisenberg and H. B. Gray, *Inorg. Chem.*, 2011, **50**, 9741–9751.

18 J. Pitchaimani, S. F. Ni and L. Dang, *Coord. Chem. Rev.*, 2020, **420**, 213398.

19 T. Fogeron, T. K. Todorova, J. P. Porcher, M. Gomez-Mingot, L. M. Chamoreau, C. Mellot-Draznieks, Y. Li and M. Fontecave, *ACS Catal.*, 2018, **8**, 2030–2038.

20 T. Fogeron, P. Retailleau, M. Gomez-Mingot, Y. Li and M. Fontecave, *Organometallics*, 2019, **38**, 1344–1350.

21 J.-H. Jeoung and H. Dobbek, *Science (80-.).*, 2007, **318**, 1461–1465.

22 B. W. Stein and M. L. Kirk, *J. Biol. Inorg. Chem.*, 2015, **20**, 183–194.

23 A. D. Read, R. E. Bentley, S. L. Archer and K. J. Dunham-Snary, *Redox Biol.*, 2021, **47**, 102164.

24 W. R. McNamara, Z. Han, C. J. Yin, W. W. Brennessel, P. L. Holland and R. Eisenberg, *Proc. Natl. Acad. Sci. U. S. A.*, 2012, **109**, 15594–15599.

25 T. Yamaguchi, S. Masaoka and K. Sakai, *Chem. Lett.*, 2009, **38**, 434–435.

26 M. König, J. Vaes, E. Klemm and D. Pant, *iScience*, 2019, **19**, 135–160.

27 C. Costentin, S. Drouet, M. Robert and J. M. Savéant, *J. Am. Chem. Soc.*, 2012, **134**, 11235–11242.

28 C. Costentin and J.-M. Savéant, *ChemElectroChem*, 2014, **1**, 1226–1236.

29 W.-C. Hsu and Y.-H. Wang, *ChemSusChem*, 2022, **15**, e202102378.

Chapter 4: Enabling Decoupled Electrochemical CO_2 Reduction to Formate

The majority of the work in this chapter is presented as published under the title 'Electrochemically Decoupled Reduction of CO_2 to Formate Over a Dispersed Heterogeneous Bismuth Catalyst Enabled via Redox Mediators' in the journal EES catalysis.[1] *Additional work relating to the wider objectives of this thesis that was not included as part of the publication has been added where appropriate and some edits have been made for clarity.*

Mediator concentrations of 8.8 mM were used with the intention of being 10 mM, however due to a mistake in the estimated molecular mass of the isolated mediator during synthesis the concentrations were lower than intended. All data has been corrected and all quoted concentrations, either 8.8 at 10 mM, are specifically mentioned.

4.1 Introduction

Herein, we propose that the electrochemical reduction of CO_2 can be decoupled from the electrode surface in the same manner as described by the work of the Girault group mentioned in the introduction.[2,3] In this instance, decoupled refers to the spatial decoupling of the electrocatalytic reaction from the electrode surface, as show in Figure 4.1c.

By applying a decoupled approach, it is hoped that the limitations of a conventional heterogeneous electrode-catalyst – *limited surface area, low concentration of CO_2 at the electrode, and the need for high electrical conductivity* – can be overcome. Study and enhancement of the ECO_2R remains a fundamentally challenging endeavour, still plagued by selectivity, activity and efficiency limitations long after its conceptualisation. From the initial work by Hori with simple monometallic electrodes in the 1980s,[4] to the latest nanostructured, highly-tailored catalysts designed with the aid of computational methods, no catalyst has managed to achieve economic viability.[5] Copper remains the front-runner, capable of producing a range of low-carbon species, most notably methane and ethylene, albeit with poor selectivity and stability.[6–8] Most other catalysts are limited to the two-electron products of formic acid or carbon monoxide.[9] It is envisioned that decoupling catalysis from the electrode surface

will widen the scope of viable catalyst materials, possibly with improved performance.

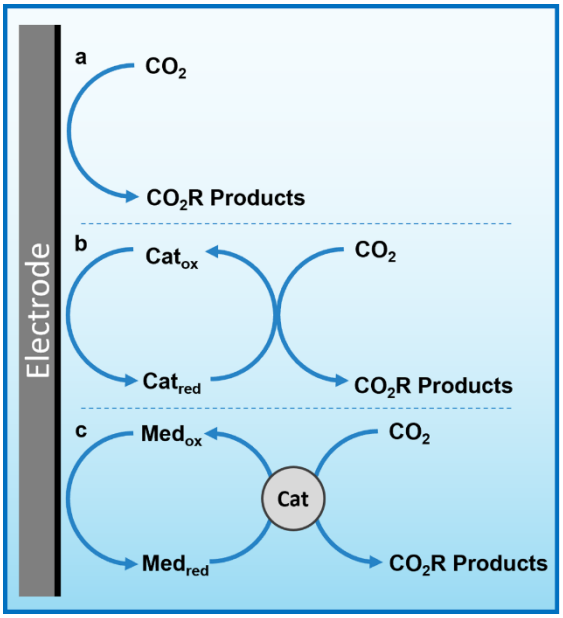

Figure 4.1 *Simplified mechanism of heterogeneous, homogeneous and redox mediated heterogeneous electrochemical CO_2 reduction. (a) Conventional heterogenous electrocatalysis, in which electrons are transferred from the electrode to CO_2 molecules on/near the electrode surface. (b) Homogeneous (or molecular) electrocatalysis, in which redox-active catalyst molecules are reduced at the electrode surface and subsequently react with CO_2 in solution. (c) Redox mediated electrocatalysis, in which a redox-active species is reduced at the electrode surface and subsequently transfers this charge and potential energy to a catalyst that then electrochemically reduces CO_2.*

Due to the complexity and relatively poor performance of ECO_2R in non-aqueous conditions highlighted in chapter 3, it was decided to switch to water based mediators and catalysts. Beyond the work presented in Chapter Three, other possible mediator systems were considered for $DECO_2R$. A brief exploration of RFB negolytes that have previously been reported for decoupled HER, discussed towards the end of Chapter One, was performed to determine if they would be suitable for DEO_2R. Aqueous species were preferred as CO_2R is most commonly reported in this medium. As previously mentioned, battery electrolytes are often most stable under either highly acidic or basic conditions.

Vanadium is the premier RFB electrolyte used in commercial systems. From a thermodynamic standpoint, the V(II)/V(III) redox couple at −0.26 V vs SHE should be able to provide enough of a driving force to enable $DECO_2R$. However, vanadium is only sparingly soluble outside of strongly acidic electrolytes. Under these conditions, it

is highly likely that hydrogen evolution will be the dominant reaction. Further, few catalysts are likely to be stable under such conditions. A few studies reporting gold and copper catalysed CO_2R around pH 2-4 in gas diffusion cells have been published,[10,11] however the overpotential required to drive the reaction is far in excess of what the vanadium couple would be able to provide.

Complexes of triethanolamine (TEA) and triisopropanolamine (TiPa) with iron are another pair of electrolytes that have garnered recent attention as RFB negolytes due to their highly negative redox potentials.[12–14] In pH 14 electrolyte, they display a redox couple just negative of 0 V vs RHE. Decreasing the pH shifts the couples more negative relative to the RHE, however the complexes quickly lose stability with at first worsening redox kinetics, followed by chemical decomposition. Starting from pH 14 solutions, 1 M HCl was added dropwise to lower the pH in increments of 1. For Fe TEa, lowering the pH gave rise to a second redox event around 400 mV more positive than the than the initial, which increased in response with number of scans. Addition of more acid to further lower the pH resulted in decomposition of the complex. Fe TiPa on the other hand at first appeared more resistant to decreasing pH, with only a small loss of reversibility as between pH 14 and pH 12. However, attempting to lower the pH further resulted in decomposition of the complex. Poor stability outside strongly basic conditions makes these complexes unsuitable for $DECO_2R$.

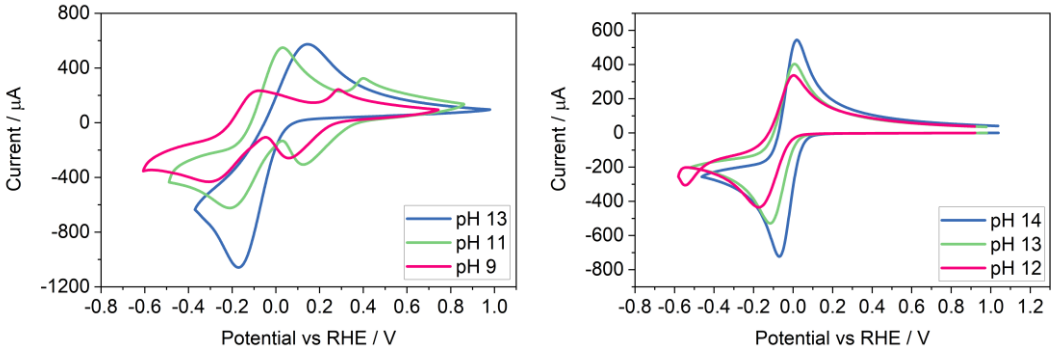

Figure 4.2 *Cyclic voltammetry of 0.1 M Fe TEA (Left) and 0.1 M Fe TiPa (Right) with varied pH. The initial pH was controlled by NaOH, with 1 M NaCl to ensure conductivity changed minimally as pH was decreased.*

Phenazines are most soluble in water at high pH, but due to being proton coupled the redox potential becomes less negative as pH is decreased into a range suitable for CO_2R. Dihydroxyphenazine (DHP) and dihydroxyphenazine carboxylic acid (DHPC) both display a redox couple slightly negative of 0 V vs RHE in 1 M NaOH electrolyte. DHP displays fully reversible kinetics, while DHPC is formally irreversible. Shifting to 1 M $KHCO_3$ electrolyte, more favourable for CO_2R, the DHP is no longer sufficiently

soluble to achieve a 10 mM solution. DHPC was soluble enough for a 10 mM electrolyte, however the shift in pH has caused a shift in redox potential such that it is now positive of 0 V vs RHE and unlikely to provide enough driving force for CO_2R or HER, although the reversibility did improve considerably.

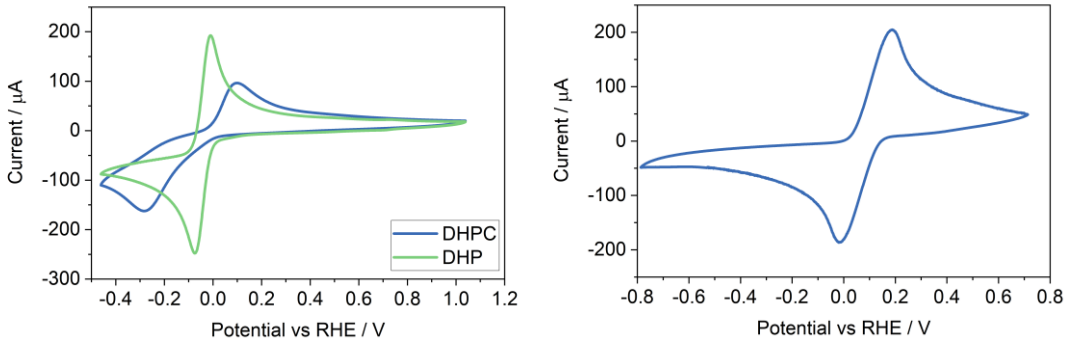

Figure 4.3 *Cyclic voltammetry of 10 mM DHP and DHPC in 1 M KOH (Left) and 1 M $KHCO_3$ (Right) respectively.*

It is clear that the best starting point for $DECO_2R$ is to find a mediator that operates at the very edge of the water potential window in near neutral pH. A uniquely promising candidate was found in the chelated chromium complex of 1,3-propanediamine-N,N,N',N'-tetraacetic acid (Cr PDTA), which is highly soluble in the near neutral pH range. As such, its use became the focus of the remaining work presented in the chapter.

4.2 Experimental

4.2.1 Chemicals and Reagents

All chemicals were used as purchased without further purification. Iron sulphate pentahydrate (97%), triethanolamine (TEA, 98%), triisopropanolamine (TiPa, 95%), 2,5-dihydroxy-1,4-benzoquinone (98%), chromium potassium sulphate dodecahydrate, sodium chloride (99%), potassium hydrogen carbonate (99.7%), potassium ferrocyanide (99%), bismuth powder (99.5%, 100 mesh), copper powder (99.5%, 100 mesh), tin powder (99.5%, 100 mesh), acetone (99%), and 1-octadecene (90% technical grade) were purchased from Thermo Fisher Scientific (Alfa Aesar, Acros Organics). 1,2-phenylenediamine (99%), 3,4-diaminobenzoic acid (97%), 1,3-propanediamine-N,N,N',N'-tetraacetic acid (99%), 1-octanethiol (98.5%), oleylamine (70% technical grade), bismuth neodecanoate, bismuth nitrate pentahydrate (99.99%), ethylene glycol (99%), and molybdenum carbide were purchased from Merck (Sigma Aldrich).

Isopropanol (99.5%) was purchased from Honeywell. Potassium hydroxide (reagent grade) was purchased from VWR. Gold mesh (99.9%, 0.06 mm diameter, 20 × 20 mm area, 82 wires per inch) and bismuth foil (99.999%, 0.25 × 10 × 10 mm) were purchased from Goodfellow Cambridge Ltd.

4.2.2 Electrochemical Methods

Electrochemical experiments were performed using a Biologic SP300 potentiostat. Voltammetric characterisation was performed in a standard three-electrode cell using a 3 mm diameter glassy carbon disk working electrode, Pt coil counter electrode and an Ag/AgCl reference electrode. Cyclic voltammetry was performed at a scan rate of 100 mV s^{-1} unless otherwise stated. Electrolyte charging was conducted in a custom flow cell (Fig. S20) with an electrode surface area of 16 cm^2, utilising GFD 4.6 SIGRACELL graphite felt electrodes heat-treated for 4 hours at 500 °C under air to improve hydrophilicity, and a fumapem® F-930 cation exchange membrane.

4.2.3 Synthesis

Solutions of Fe TEA and Fe TiPa (0.1M, 250 mL) were prepared by dissolving $Fe_2(SO_4)_3 \cdot 5H_2O$ (6.12 g) in a solution containing 3 M NaOH and 1 M NaCl, alongside excess TEA (18.65 g) or TiPa (23.91 g) respectively. The solutions were left to stir for three days to ensure complete reaction. The complexes were only stable in the highly basic electrolyte and could not be isolated.

DHP and DHPC were synthesised via a condensation reaction adapted from previously reported work.[15] For DHP, 130 mL of water was heated to 123°C under an inert atmosphere (N_2). 1.8 g of 2,5-dihydroxy-1,4-benzoquinone was aliquoted into 3 portions and added slowly during the heating of water to ensure the solute dissolves. Once the solution started to boil 1.3 g of 1,2-phenylenediamine was added to the flask and was left to reflux overnight. After reflux, the product was recovered via vacuum filtration then was washed with acetone. Finally, the wet product was dried in the oven. DHPC was synthesised by the same method, with 1,2-phenyldiamine substituted for 3,4-diaminobenzoic acid.

Potassium chromium 1,3-propanediamine-N,N,N',N'-tetraacetate was synthesised in a single step reaction from readily available precursors. 1,3-propanediamine-N,N,N',N'-tetraacetic acid (9.18 g) and potassium chromium sulfate dodecahydrate (14.48 g) were added to a round bottom flask (RBF) along with water (60 mL), and the mixture was refluxed for 2 hours. Potassium

hydroxide (6 g) was added and the mixture was stirred for a further hour, followed by dropwise addition of potassium hydroxide solution (5 M) until the mixture was fully neutralised. An equal volume of acetone (approx. 100 mL) was then added, causing a pale purple precipitate to form, which was removed by vacuum filtration. The filtrate was reduced under vacuum to approx. 60 mL and then added dropwise by pipette to ice cold isopropanol (300 mL), resulting in a pink precipitate that was collected by vacuum filtration and washed with isopropanol. CHNS elemental analysis indicated the presence of a small sulphate impurity (2-3%). Measured: (6.77% N, 31.02% C, 4.12% H, 0.22% S), expected: (6.26% N, 29.53% C, 4.51% H, 0.00% S). Isolated as a trihydrate with molecular weight of 447.38 g mol^{-1}. Successful synthesis was confirmed by comparison of UV-vis spectra and cyclic voltammetry to previously reported works.[16]

Bismuth nanospheres (hereafter referred to as Bi NS) and bismuth rhombic dodecahedron nanoparticles (hereafter referred to as Bi RD) were synthesised by methods adapted from existing literature.[17] Bi NS: Bismuth nitrate pentahydrate (4.55 g) was added to a 125 mL PTFE lined autoclave (Parr model 4748) along with ethylene glycol (37.5 mL), which was sealed and heated to 180 °C for 24 hours. The resulting nanoparticles were washed by centrifugation and redispersion in ethanol, then water three times each; and were dispersed in water (80 mL) and stored as an ink with an approximate loading of 19 g L^{-1}. Bi RDNP: Bismuth neodecanoate (720 mg) and 1-octadecene (5 mL) were added to an argon-flushed RBF and heated at 85 °C for 30 min, after which 1-octanethiol (10 mL) was injected, causing the mixture to turn yellow/brown. This was heated for a further 30 min, followed by the addition of olyelamine (10 mL) and another 30 min of heating, turning the mixture black and opaque. Once cooled, the resulting nanoparticles were washed by centrifugation and redispersion in ethanol three times. The morphology of the nanoparticles was subsequently confirmed by scanning electron microscopy.

4.2.4 Catalyst Screening

Batch decoupled reduction reactions were performed in a sealed Schlenk flask, evacuated and replenished with CO_2 five times to ensure a controlled atmosphere. The redox mediator solution was charged in the custom flow cell against an excess of $K_4[Fe(CN)_6]$ under an inert N_2 atmosphere. Once charged, the solution was saturated with CO_2 and a 20 mL aliquot was injected into the reaction vessel containing the catalyst material and was left to react with the aid

of magnetic stirring. The reaction was considered complete when the colour of the mediator solution returned to its ground state and ceased effervescing. The catalyst loading was approximately 25 mg for Bi, Cu, Sn, Mo_2C and Ni powders, 142 mg for the Au mesh, 30 mg for Bi foil, 19 mg for Bi NS, and 10-15 mg for BI RD. Between experiments, the reactor was cleaned mechanically and with concentrated acid to remove residual catalyst.

4.2.5 Product Analysis

Reduction products were analysed by a combination of gas chromatography (GC) for the gas phase and ion chromatography (IC) for the liquid phase. GC was performed utilising a Shimadzu 2030 equipped with a dielectric-barrier ionisation detector (BID) and ResTek Shin Carbon ST 80/100 column. The instrument was calibrated in the 0-1000 ppm range for the gaseous products H_2, CO, CH_4 and C_2H_4 by use of calibration gas supplied by BOC Ltd. Samples were extracted from the vessel and introduced via a gas tight syringe, typically after a 5× dilution to bring the concentrations into the calibration range. IC was performed using a Metrohm Eco IC equipped with a Metrosep organic acids column (250/7.8) and a conductivity detector. Formate concentration was determined from a calibration curve in the 0-100 ppm range by use of a 1000 ppm calibration standard purchased from Sigma Aldrich.

4.3 Results and Discussion

4.3.1 Redox Mediator Characterisation

The primary challenge in achieving DECO_2R is identifying a mediator able to provide sufficient driving force for the less-than-facile reaction. When targeting hydrogen evolution, a mediator simply needs a redox potential below 0 V vs the reversible hydrogen electrode (RHE) to provide a thermodynamic driving force, whereas most CO_2 reduction catalysts require operating potentials at least as negative as −0.7 V vs RHE to activate the reaction. Even on relatively inert carbon cloth electrodes, this is already pushing the limits of water's electrochemical stability, which makes finding aqueous species with sufficiently negative redox processes challenging, and introduces the risk of competition from hydrogen evolution. Fortunately, the wellspring of existing literature detailing FB electrolytes offers an excellent foundation from which to draw inspiration when selecting a redox mediator.

The fully chelated chromium complex of 1,3 propanediamine-N,N,N',N'-tetraacetic acid has recently been highlighted as an aqueous RFB anolyte with an unusually negative single electron reduction at E^0 = −1.2 V vs the standard hydrogen electrode (SHE) (−0.6 V vs RHE in 1 M $KHCO_3$ electrolyte), along with high solubility and long-term stability.[16] As seen in Fig. 4.4a, the complex operates at the edge of the potential window for aqueous electrochemistry at this pH (8.5), allowing for the construction of aqueous RFBs with large cell potentials, and providing a large driving force for aqueous reduction reactions when used as a redox mediator. The fully chelated nature of the complex should inhibit it from acting as a molecular catalyst, allowing it to effectively transfer charge and energy without undergoing any self-discharge reactions. Indeed, the mediator does not spontaneously discharge while saturated with CO_2, and an oxidative back-peak is visible in cyclic voltammograms of Cr PDTA saturated with CO_2.

$$Cr(III)\,PDTA + e^- \rightarrow Cr(II)\,PDTA \qquad E^0 = -1.2\,V \quad (1)$$

$$CO_2 + e^- \rightarrow CO_2^{\cdot -} \qquad E^0 = -1.9\,V \quad (2)$$

$$CO_2 + 2H^+ + 2e^- \rightarrow HCOOH \qquad E^0 = -0.61\,V \quad (3)$$

$$CO_2 + H_2O + 2e^- \rightarrow HCOO^- + OH^- \qquad E^0 = -0.43\,V \quad (4)$$

$$CO_2 + 2H^+ + 2e^- \rightarrow CO + H_2O \qquad E^0 = -0.53\,V \quad (5)$$

$$CO_2 + H_2O + 2e^- \rightarrow CO + 2OH^- \qquad E^0 = -0.52\,V \quad (6)$$

$$2H^+ + 2e^- \rightarrow H_2 \qquad E^0 = -0.41\,V \quad (7)$$

$$All\ vs\ SHE\ at\ pH\ 7$$

The combination of a large driving force and a near neutral pH gives Cr PDTA a large potential over the thermodynamic requirement (overpotential) to act as a redox mediator for ECO_2R (Equations 2-6)[18]. This driving force also easily enables hydrogen evolution (Equation 7), which acts as a parasitic competing reaction during charging, even on largely inert carbon felt electrodes and glassy carbon surfaces, and especially if trace metal impurities are present in the electrolyte. This is highlighted by the two distinct regions in Figure 4.4b. The first linear potential region between 20 and 900 s follows a shallow gradient as controlled by the ratio of Cr(II)/Cr(III) according to the Nernst equation (as the $K_4Fe(CN)_6$ is in excess it has little influence over the cell potential). The second linear region between 1000-1200 s has minimal gradient as hydrogen evolution has become the dominant electrochemical process and occurs under a steady

state. The small potential step between these two processes indicates how close to the edge of the solvent window the mediator operates. It was also noted by Robb *et al.* when reported as a flow battery negolyte that hydrogen evolution was observed on stainless steel fittings and from trace metal impurities in the electrolyte.[16]

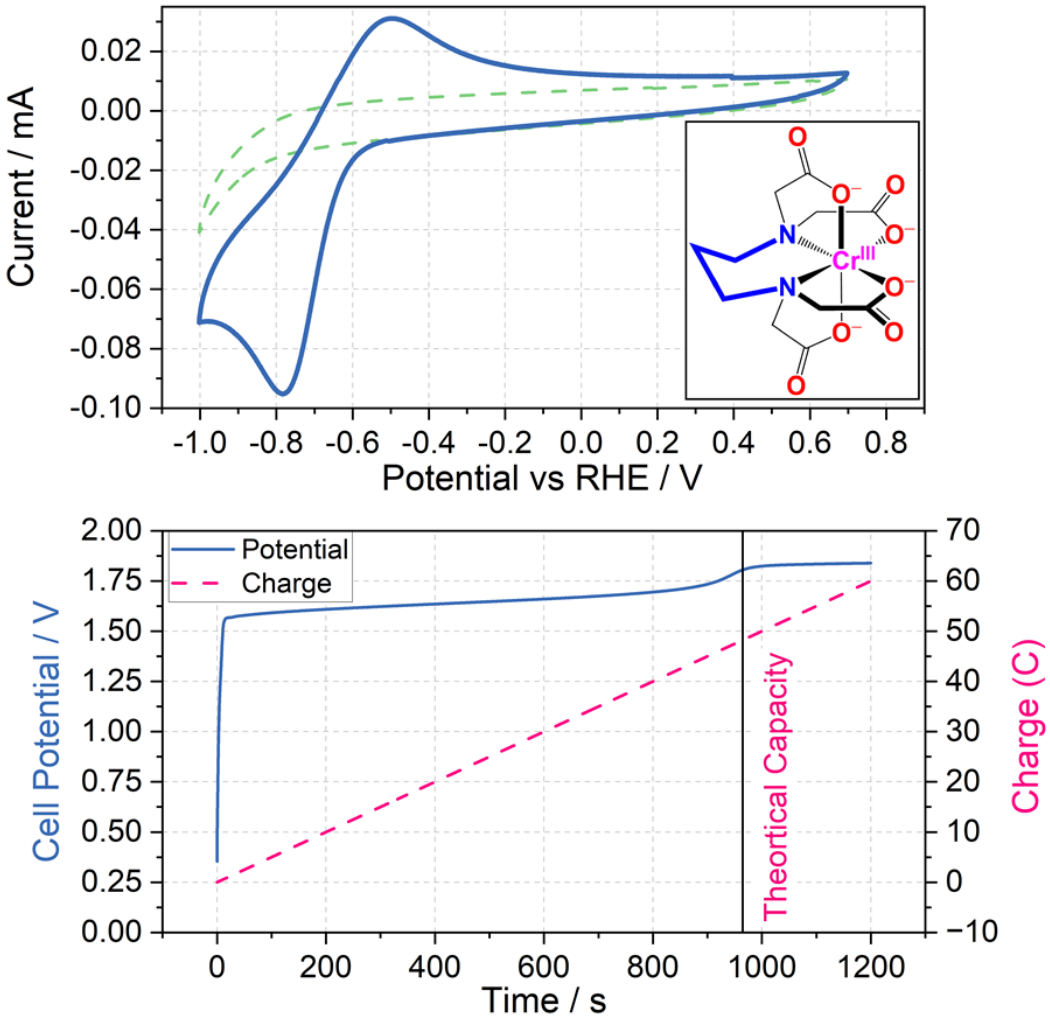

Figure 4.4 *Cyclic voltammetry and charging profile of Cr PDTA. (Top) (Main) Cyclic voltammograms recorded in 1 M $KHCO_3$ supporting electrolyte in water with (solid blue) and without (dashed green) 8.8 mM Cr PDTA using a glassy-carbon electrode (Scan rate of 100 $mV.s^{-1}$). Peak separation of 285 mV with broad peaks indicates a quasi-reversible redox process with slow kinetics. (Inset) Chemical structure of Cr(III) PDTA. (Bottom) Charging profile of 8.8 mM Cr PDTA with 1 M $KHCO_3$ supporting electrolyte against excess $K_4Fe(CN)_6$ at 50 mA (electrode surface area 16 cm^2, Sigracell GFD 4.6).*

While cyclic voltammetry of Cr PDTA on glassy carbon electrodes typically displays a large peak separation indicating poor reversibility, this is not a fundamental issue with the complex. The electron transfer is still assumed to be

an entirely outer sphere process. A wide range of chromium chelates have been reported to have similar electrochemical properties, with the PDTA ligand offering the best performance.[19] They were tested using a Hg drop working electrode, with which the Cr PDTA complex displayed fully reversible characteristics.

As mercury has many undesirable characteristics as an electrode material, an alternative with similar electrochemical performance is highly desirable. Of these, bismuth represents a promising replacement. It has been previously explored as a modification to the carbon felt/cloth electrodes commonly used in redox flow batteries.[20,21] The improved electron transfer kinetics improve the voltage efficiency, and thus the maximum power output, of the battery. This is evident in cyclic voltammetry performed using an electrode that has been deposited with bismuth (Figure 4.5), in which the complex displays fully reversible kinetics. Further, bismuth has a high overpotential with respect to hydrogen evolution, helping limit charge lost to this parasitic side reaction.[22]

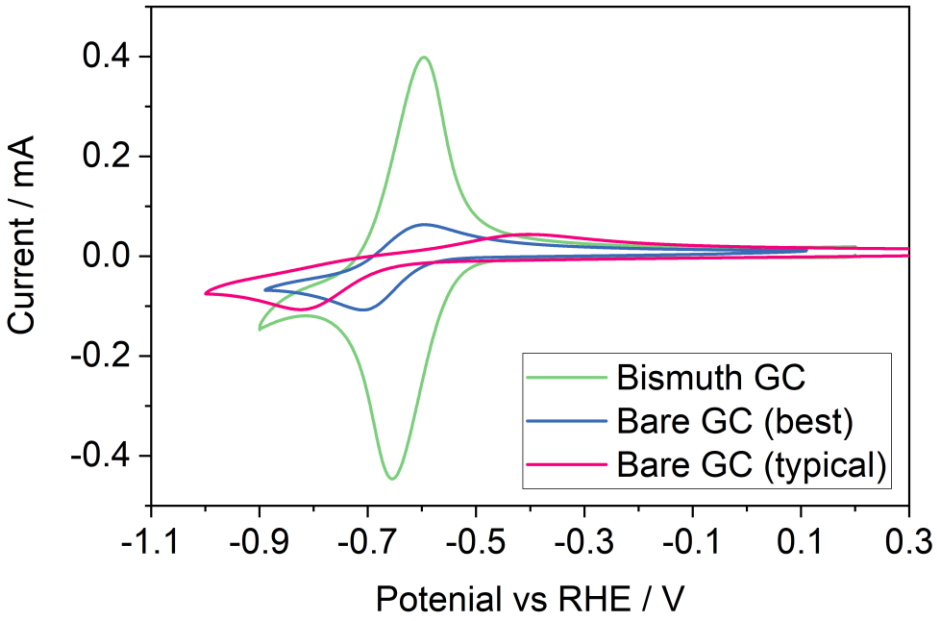

Figure 4.5 *Cyclic voltammetry of 10 mM KCrPDTA with 1 M $KHCO_3$ electrolyte performed at 100 mV s−1 in a three-electrode cell. The purple and blue traces display the typical (irreversible) and best achieved (quasi-reversible) voltammetry observed on a freshly polished glassy carbon electrode, while the green trace displays the fully reversible voltammetry observed on a bismuth modified glassy carbon electrode.*

4.3.2 Aqueous Decoupled CO_2 Reduction on Bulk Metal Catalysts

To determine the effectiveness of Cr PDTA as a redox mediator for DECO_2R, a range of simple catalysts were tested to target all possible products. As an initial proof-of-concept, inexpensive bulk metal powders were screened as catalysts using a Schlenk tube as rudimentary batch reactor to establish whether any CO_2 reduction products could be detected. Metal selection was based on the seminal systematic exploration reported by Hori.[23] Bismuth and tin powders were used to target formate production, while a reusable gold mesh was used to target CO formation. Copper powder was screened in the hope of observing further reduced products such as methane and ethylene. For comparison, molybdenum carbide and nickel powders were used as expected hydrogen evolution catalysts.

Using a fixed volume of charged mediator solution at a known concentration, the total charge passed during the CO_2 conversion can be estimated, allowing for a determination of the faradaic efficiency of each substituent product by gas and ion chromatography quantification. These results are summarised in Figure 4.6. Complete charging is signified by a colour change from the red ground state (Figure 4.9a) to the pale green reduced state (Figure 4.9b), and when the charging curve deviates from the plateau region (Figure 4.4b).

Bismuth was chosen due to its large overpotential requirement with respect to hydrogen evolution and having been previously observed to reduce CO_2 almost exclusively to formate.[24] When used as the catalyst for DECO_2R mediated by Cr PDTA, bismuth gave the highest yield of CO_2R products, with formate making up 54 ±4.7% of the observed products. The remaining 46 ± 4.7% was predominantly H_2, though trace CO was also detected. The overall faradaic yield when using bismuth was 61 ± 0.4%, with the reaction taking about 30 minutes. While Au is typically considered a good catalyst for CO production,[25] when used for DECO_2R mediated by Cr PDTA, only a small amount was observed, with a faradaic yield of just 0.6 ± 0.3%, making up about 1 ± 0.5% of the measured products. Formate accounted for another 2 ± 1% of the products and H_2 made up the remaining 97 ± 1.6%, with an overall faradaic yield of 57 ± 5.2%. The reaction took around one day to complete. While the bismuth was, along with all the other simple catalysts, a powder consisting of 150 micron or smaller particles, it is important to note that the gold mesh was by comparison

macroscopic, and as such had a much lower surface area despite the larger mass deployed (142 mg vs 25 mg).

No further reduction products were observed when using Cu powder as the catalyst, with H_2 again making up 96 ± 0.8% of the observed products. Formate constituted the majority of the remaining 4 ± 0.8%, with a trace of CO also detected, with a total faradaic yield of 56 ± 11%. The reaction appeared complete after 10 minutes. Furthermore, when left in contact for more than a few days, copper metal displaces the Cr(III) redox mediator from its chelating ligand, ultimately resulting in a deep blue solution of Cu(II) (Figure 4.7). Sn powder, which was expected to produce formate, also generated mostly hydrogen at 95 ± 0.3% selectivity along with 5 ± 0.3% formate and a trace of CO, with a faradaic yield of 69 ± 1.7%. Again, the reaction took about 10 minutes. As expected Mo_2C and Ni produced mainly H_2, at 98.5 ± 0.09% and 98.9 ± 0.08% of the observed products respectively, with overall faradaic yields of 41 ± 3.1% and 58 ± 1.4%. Molybdenum carbide was reasonably active, with discharge taking about 15 minutes, while the nickel displayed poor activity, with discharge taking approximately one day. Recently, molybdenum carbides have been explored as potential catalysts for CO_2R, both electrochemically and through hydrogenation, however minimal CO_2R products were observed when used in the Cr PDTA mediated system.[26,27]

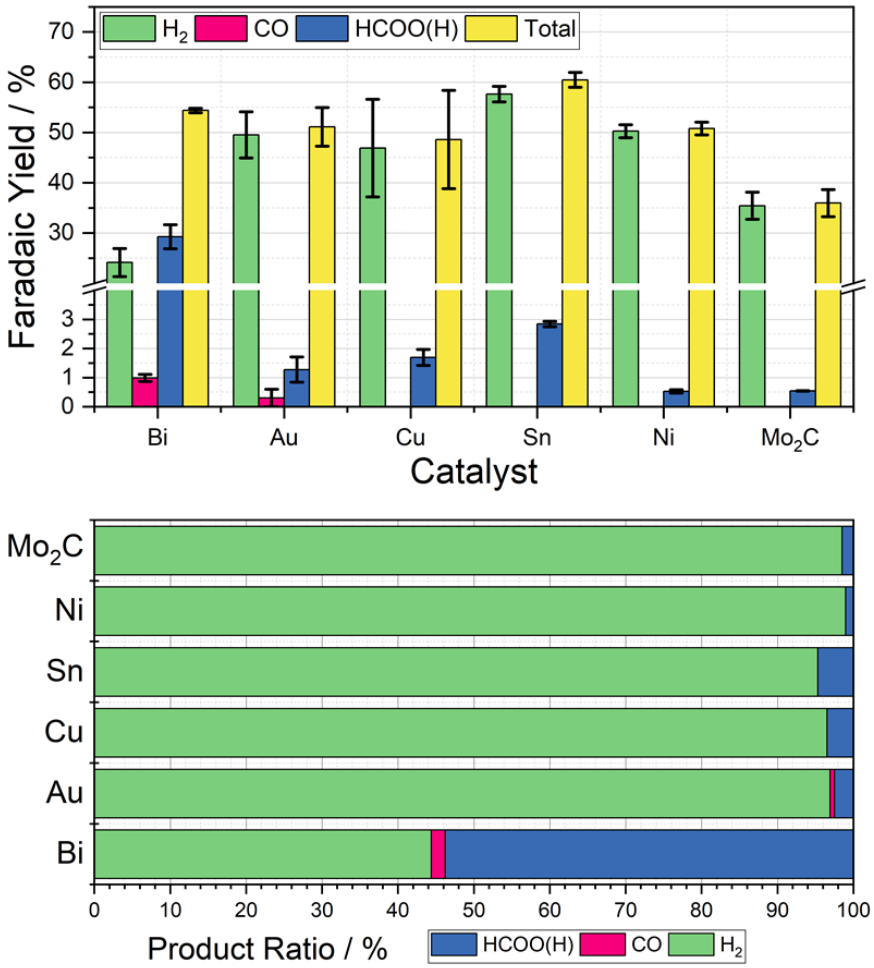

Figure 4.6 *(Top) Column chart indicating the average faradaic yields of H_2 (green), CO (pink), HCOO(H) (blue), and in total (yellow) measured when 20 mL aliquots of 8.8 mM Cr PDTA were discharged over the heterogenous catalysts Bi, Au, Cu, Sn, Ni, and Mo_2C inside a sealed CO_2 atmosphere, with error bars indicating the standard deviation within each triplicate set. (Bottom) Row chart indicating relative product ratios for Cr PDTA mediated CO_2 reduction.*

Catalyst free control reactions indicated the presence of contamination within the reaction vessel, despite cleaning with aqua regia and ultrapure water between experiments. The charged mediator should be stable under inert conditions, however it appeared to discharge very slowly over several weeks in the absence of catalyst. The mediator is expected to spontaneously reduce oxygen on contact with air, however product analysis also indicated the formation of a small amount of both H_2 (15.8 ± 2.5%) and $HCOO^-$ (4.4 ± 0.8%) as the mediator discharged passively. Compared to active catalysis, this discharge is very slow and occurred over many days, however it was envisioned that the charged mediator would be stable for long term storage as a battery

negolyte and only be discharged by the intended catalyst to maintain product selectivity. It is suspected that the discharge is caused by metal ion contamination, either from trace impurities within the electrolyte, as has been previously reported, or residual catalyst contamination within the reactor.[8,28] Under the reducing conditions, these metal ions can be deposited, creating catalytic sites to further discharge the mediator. Equally, it may not be impossible for the mediator to act as a molecular catalyst, albeit very poorly, as the chelating ligand would need to relinquish one or more coordination sites to allow coordination of the reaction intermediates. This introduces concerns when considering the possible effects on long term catalyst stability and selectivity, and raises questions about what portion of the products are truly formed on the intended catalyst compared to the contamination, especially on the less active catalysts. It is likely this contamination contributed towards the large standard deviation seen in the product selectivity of some of the catalysts tested.

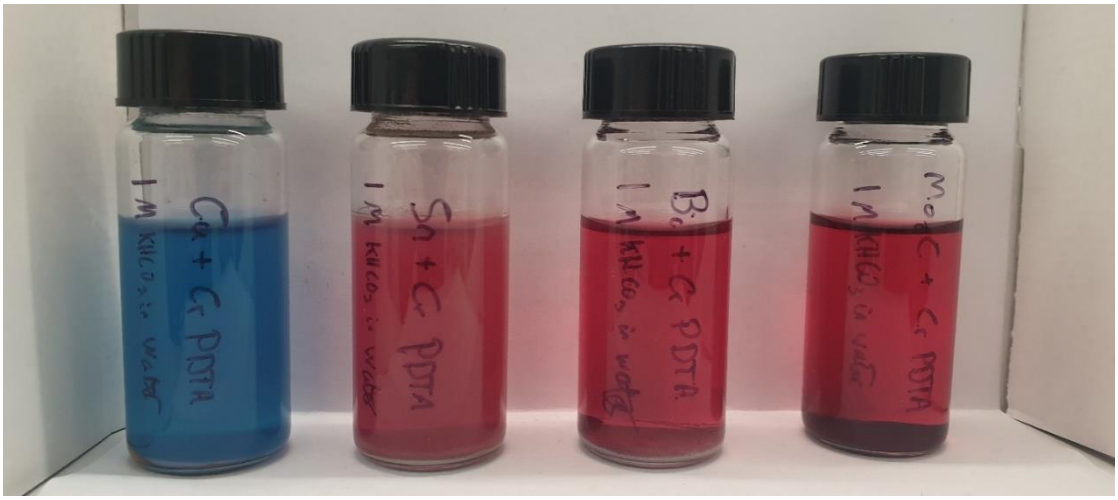

Figure 4.7 *Samples of 8.8 mM Cr PDTA with 1 M $KHCO_3$ in water with (left to right) Cu, Sn, Bi and Mo_2C powder after three months. The copper powder has displaced the chromium from the complex, resulting in a deep blue Cu(II) solution and plating the copper particles light grey with chromium. The Sn powder has plated the glass vial however the complex is unaffected. Both bismuth and molybdenum carbide underwent no visible reaction with the complex.*

4.3.3 Faradaic Losses

The faradaic yields observed were typically in the 50-60% range, indicating some inefficiency in the batch methodology whereby charge is lost to a number of unobserved processes. The first is the reduction of O_2, for which the charged mediator has considerable driving force. While care was taken to ensure the mediator remained under N_2 or CO_2 atmospheres during charging and transfer,

it is unavoidable that some charge will be lost due contact with O_2 from residual air, which was always observed in the GC analysis. Because it is unavoidable that further air exposure will occur during transfer of the same to the GC, it is unclear how much O_2 was introduced before and after mediator discharge. It also assumed that the mediator is at a 100% state of charge from the colour change and charging profile, however this is not quantitative. Furthermore, it is possible that gaseous products are lost during transportation and dilution of the samples prior to GC analysis.

A further loss of charge occurs due to a 'tax' of electrons that are required to bring the Fermi level of the catalyst in line with the electrochemical potential of the mediator solution when they are introduced, where the particles effectively behave as a series of redox couples. This has been described in detail for small nanoparticles, where the effects of quantisation result in discrete energy levels.[29] Ultimately, the number of electrons needed to shift the Fermi level will be dependent on a range of factors including particle surface area, number of atoms, and surface species including capping agents and counter ions, as well as the initial Fermi level of the particle, all of which will be unique to each material. For larger particles where the density of energy levels is more akin to bulk metal, a large but finite number of electrons will be transferred in order to bring the system into equilibrium; this assumes the particles are inert, however, as they are acting as electrocatalysts, this is not the case. Instead, a steady state will be established where electrons are transferred onto the particles at the same rate that they are used in reduction reactions. As the reaction proceeds, the Fermi level of the system will shift until there is no longer a driving force and equilibrium is reached. Exploring these effects is far beyond the scope of this initial proof of concept, and as such they are simply taken as a limitation of the batch technique used to screen the catalysts.

4.3.4 The Effect of Buffers and pH Changes

Interestingly, when the mediator solution and reaction vessel were saturated with N_2 instead of CO_2, for the purpose of control experiments, formate was still observed as a product for many of the catalysts, with bismuth powder yielding H_2 and $HCOO^-$ at faradaic efficiencies of 27 % and 7.5 % respectively; this is coupled with a large peak in the GC trace attributed to CO_2. The source of this CO_2 is the $KHCO_3$ electrolyte, which is decomposing to fulfil the equilibrium between aqueous carbonate species, releasing CO_2 which is then accessible for

reduction.[23] It is this fast exchange which makes carbonate electrolytes the favoured choice for ECO_2R, as it effectively increases the activity of aqueous CO_2 far beyond the saturation point of dissolved gas, aiding in mass transport to the catalyst surface and providing a buffering effect against localised pH change during electrolysis. Furthermore, there is growing evidence that various dissolved carbonate species are reduced at the electrode surface and contribute to the overall ECO_2R reaction.[30]

In an effort to fully eliminate CO_2 from the control experiments, the supporting electrolyte was switched to KCl. This resulted in hydrogen as then only detected product on the bismuth powder catalyst, at a faradaic efficiency of 12%. This change in electrolyte composition had no visible effect on the complex in the Cr(III) state, however once charged to Cr(II) the mediator solution exhibited a pale blue colouration (Figure 4.9d). When subsequently discharged, either by a catalyst or by air, the mediator solution no longer returned to its red colour, instead taking on a deep purple hue (Figure 4.9e). To rationalise the changes in colour, UV/Vis. spectra of the mediator were taken for the range of observed states (Figure 4.8). In its fresh red state, the mediator solution exhibits two strong absorption peaks centred around 510 and 386 nm, with molar absorption coefficients of 101 M^{-1} cm^{-1} and 75.7 M^{-1} cm^{-1} respectively. Once charged, neither the green nor blue states display absorbance peaks, but rather have broadly low absorbance above 400 nm and high absorbance below 400 nm. In its spent (purple) state, the mediator again displays two absorbance peaks, slightly redshifted as compared to the fresh solution with the longer wavelength peak much broader and lower in absorbance intensity.

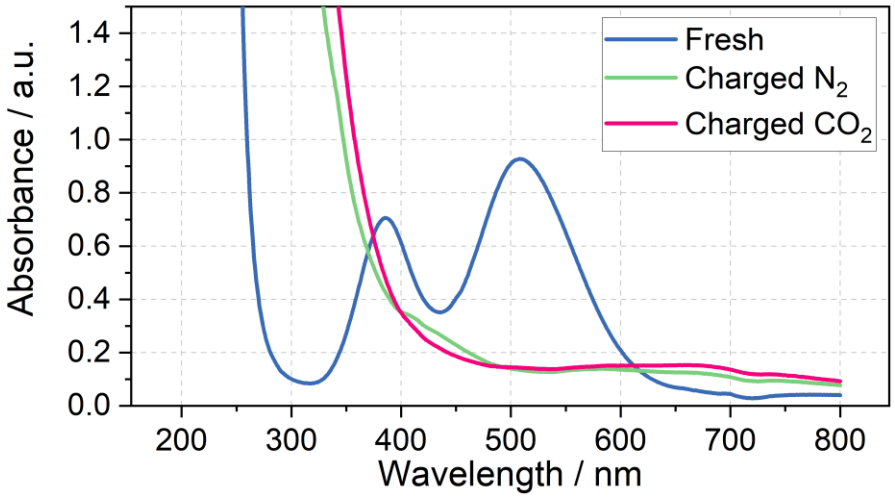

Figure 4.8 *UV/vis absorbance spectra of 8.8 mM KCrPDTA in 1 M $KHCO_3$ electrolyte as prepared and fully charged K_2CrPDTA under both N_2 and CO_2 saturated atmospheres.*

As hydroxide ions are an expected product of all reduction half reactions at a neutral pH (see Equations 4 and 6), and without any balancing oxidation, the pH of the mediator solution will increase when used in a batch reaction. Dissolved CO_2 in the form of carbonic acid will react with the produced hydroxide, limiting the pH change while consuming some of the available CO_2. In its fresh state, with 1 M $KHCO_3$ as the supporting electrolyte, the pH was around 8.5, and once charged and spent the pH increased to around 9.2, suggesting presence of the excess hydrogen carbonate is somewhat able to buffer against pH change. When 1 M KCl was instead used as the supporting electrolyte, the pH of fresh solution was 7.8, and once spent this increased to around 11. A small amount of 1 M HCl was added to return the pH to that of the fresh solution, which restored the red colouration, and the position and ratio of the peaks in the UV/Vis. spectrum to that of the fresh solution (Figure 4.9).

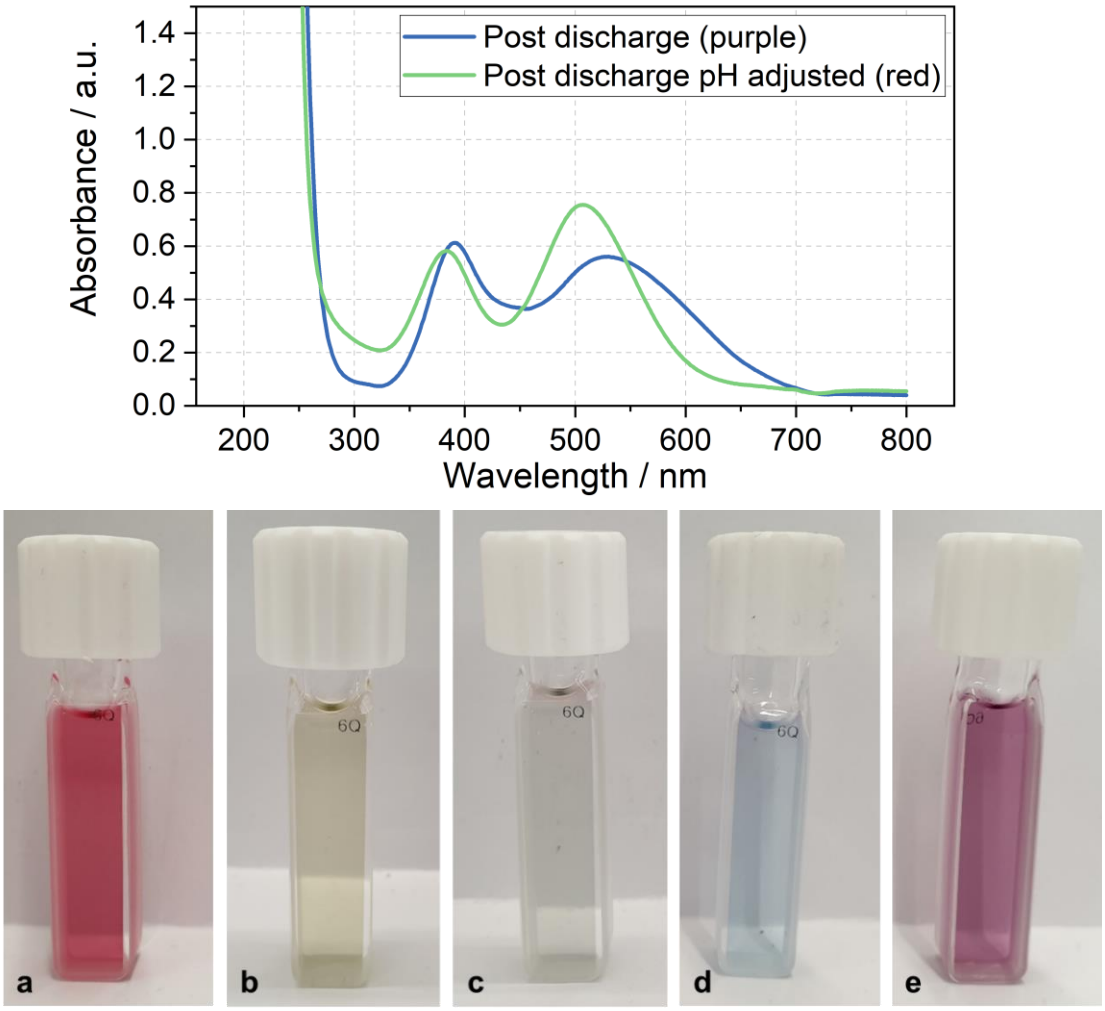

Figure 4.9 *(Top) UV/vis absorbance spectra of 8.8 mM Cr PDTA in 1 M KCl electrolyte. (Bottom) Solutions of 8.8 mM KCrPDTA. (a) Red ground state. (b) Green charged state in 1 M $KHCO_3$ under N_2. (c) Blue-green charged state in 1 M $KHCO_3$ under CO_2. (d) Blue charged state in 1 M KCl. (e) Purple ground state after discharge in 1 M KCl at pH 11.*

4.3.5 Optimised Bismuth Materials as Potential Catalysts

Having observed bismuth 100-mesh powder as giving the best yields of a CO_2R product, it was chosen as the focus in preparation of tailored decoupled CO_2R catalysts. A particularly promising material was reported by Xie et al, where they developed facet-controlled bismuth rhombic dodecahedra with a much less negative onset potential for ECO_2R compared to bulk metal, with selectivity starting at 85% and peaking at 95% across the −0.6 to −1.2 V vs RHE potential range.[17] This was compared to both Bi foil and Bi nanospheres, which they found to have selectivity starting around 60% at −0.6 V vs RHE, only increasing to 85% at −0.8 V vs RHE for the nanospheres and −0.9 V vs RHE for the bulk foil, with

both achieving a peak selectivity of around 90%. The Cr PDTA mediator operates at the lower end of this scale, where the bulk foil material only achieved a selectivity of around 60% in Xie's work, which compares well with the 55% selectivity we observed in the decoupled system when dispersed bismuth powder was deployed as the catalyst.

Both the rhombic dodecahedra and the nanospheres were synthesised using the procedures described by Xie et al. for performance comparison, with the results summarised in Figure 4. 13. The Bi nanospheres (Bi NS) were synthesised by solvothermal reduction of bismuth nitrate in ethylene glycol. Surface morphology was confirmed by SEM (Figure 4.10), where the particles were found to be uniform spheres with size ranging 50-500 nm. The bismuth rhombic dodecahedra (Bi RD) were synthesised by reducing bismuth neodecanoate with oleylamine in the presence of 1-octanethiol as a capping agent to control the shape. STEM imaging (Figure 4.10) displayed the variety of shapes consistent with rhombic dodecahedra in various orientations, and revealed a tight size distribution of 75 ± 5 nm, compared to the 200 nm particles previously reported. While the particles were smaller than intended, the XRD diffractogram (Figure 4.10) displayed the same key feature, the 104 peak slightly higher in intensity than the 110 peak.

The first nanomaterial evaluated was the Bi nanospheres. To test their performance as a catalyst for DECO_2R, 1 mL of the nanoparticle dispersion was added to the reaction vessel and dried giving an approximate catalyst loading of 19 mg. Immediately upon addition of the charged mediator solution, a large amount of gas bubbles formed, indicating very high activity, with complete discharge in less than five minutes. Formate constituted one third of the observed products, with the other two thirds being almost entirely hydrogen. The activity of these nanoparticles was much higher than that of the 100-mesh Bi powder, discharging the mediator solution more than ten times faster for a similar mass loading (19 mg vs 25 mg), as would be expected due to the huge increase in surface area. However, the increased activity is compromised by a decrease in both CO_2R selectivity (33 ± 1.2% vs 54 ± 4.7%) and overall faradaic efficiency (56 ± 5.8% vs 61 ± 0.5%). This does not compare favourably with the previously reported results from Xie *et al*, where the Bi NS slightly outperformed the bulk Bi in terms of selectivity for formate at a given potential.

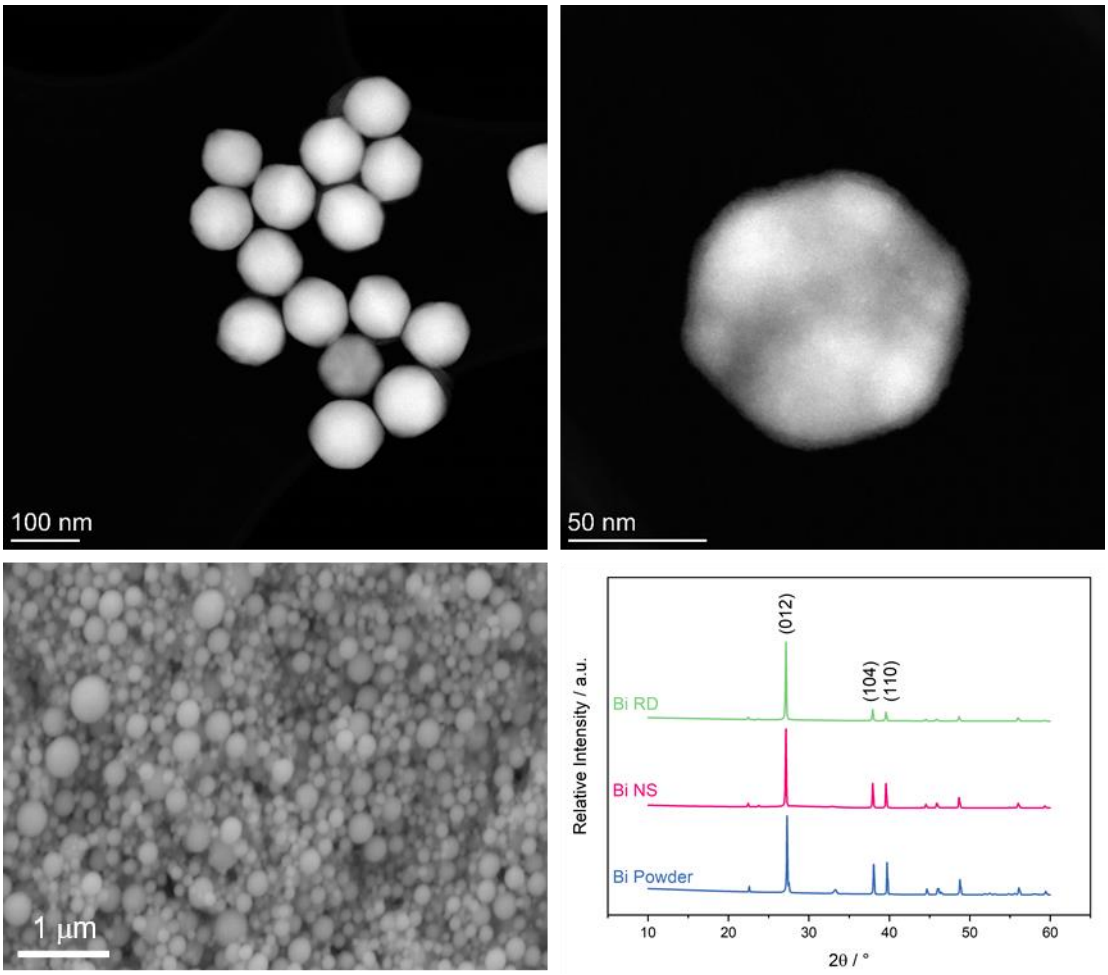

Figure 4.10 *(Top Left) STEM image of bismuth RD indicating the variety of observed shapes depending on particle orientation. (Top Right) STEM image of single bismuth RD nanoparticle highlighting the shape control by presenting a hexagonal shape. (Bottom Left) SEM image of bismuth NS, displaying a wide size distribution. (Bottom Right) XRD diffractogram indicating the relative intensity of the diffraction peaks.*

The second nanomaterial evaluated was the Bi rhombic dodecahedra (Bi RD). The catalyst was deployed in the reaction vessel by drying 0.5 mL of catalyst dispersion in the vessel prior to addition of the mediator, for an approximate loading of 15 mg. Following the addition of charged mediator solution, a small number of bubbles began to form, and, after approximately 15 minutes, the reaction appeared to be complete. Product analysis revealed a CO_2R selectivity of 87 ± 0.2%, with formate making up an impressive 85 ± 0.3% of the observed products. This is in agreement with the previously reported selectivity when the catalyst was deployed in a conventional H-cell at the same operating potential. This successfully established $DECO_2R$ as a viable technique, albeit constrained by the need for catalysts with high selectivity at relatively mild potentials. Ultimately, performance was limited by the low faradaic yield of just 51%, which

remains the biggest drawback of the batch technique. The nanoparticles did not readily disperse in water due to the hydrophobic 1-octanethiol capping agent, resulting in the formation of film like aggregations during the DECO_2R reaction. SEM imaging of spent catalyst (Figure 4.12) indicated minimal decomposition of the catalyst after the single pass of charged mediator.

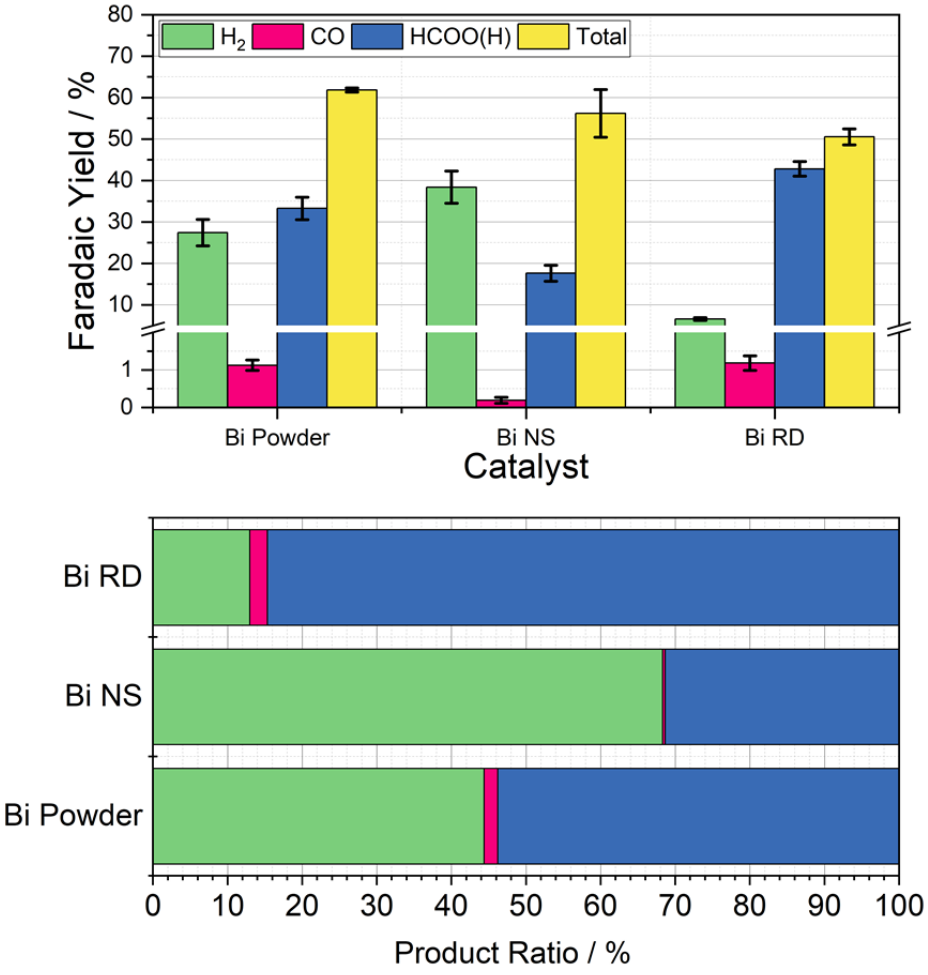

Figure 4.11 *(Top) Column chart indicating the average faradaic yields of H_2 (green), CO (pink), HCOO(H) (blue), and in total (yellow) measured when 20 mL aliquots of 8.8 mM Cr PDTA were discharged over commercial bismuth powder (50 µm), bismuth nanospheres (50-500 nm), and bismuth rhombic dodecahedra (80 nm) inside a sealed CO_2 atmosphere, with error bars indicating the standard deviation within each triplicate set. (Bottom) Row chart indicating relative product ratios for Cr PDTA mediated CO_2 reduction over the bismuth catalysts.*

As a practical macro scale catalyst, a Bi foil was evaluated in the same reaction conditions for the sake of comparison. The foil gave the lowest yield of CO_2R products out of all the Bi materials tested at just 10% of the observed products, with an overall faradaic yield of 41%. The performance of the foil was defined by

its low activity, resulting in a discharge time of around seven days, on the same timescale as the observed self-discharge.

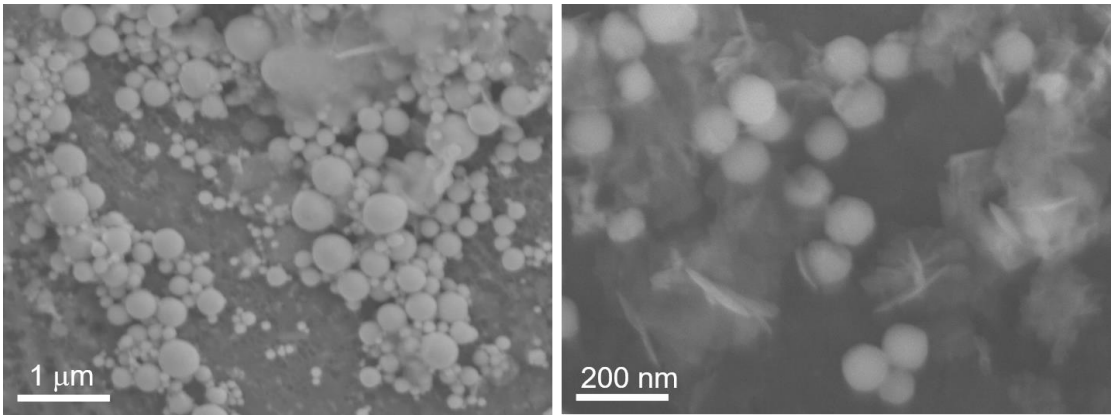

Figure 4.12 *(Left) Spent Bi NS. (Right) Spent Bi RD. Both displaying good stability from a single pass of mediator.*

4.3.6 Mechanistic Insights

As mentioned, bismuth is known to be highly selective towards formate production when used for ECO_2R as a conventional heterogeneous electrocatalyst. Bismuth, along with many other catalysts, tends to be most selective towards ECO_2R at operating potentials around and below −1.0 V vs RHE.[23] At more positive potentials, there is insufficient energy to activate the thermodynamically and kinetically demanding initial electron insertion into CO_2 (thermodynamic potential of −1.9 V vs SHE without stabilisation via a catalyst), making water reduction to hydrogen the only viable reaction, even on purportedly unfavourable catalysts.

An insufficiently negative potential is the primary reason justifying the low product selectivity observed in the $DECO_2R$ reactions, as ECO_2R is inhibited by the limited overpotential that the mediator is able to provide, resulting in low activity, leaving hydrogen as the only kinetically feasible product in most cases. As discussed, the Fermi level of the catalyst is controlled and maintained by electron transfer from the redox mediator. Assuming a fast electron transfer, the Fermi level of the catalyst will be the same as the electrochemical potential of the solution, which itself can be calculated from the Nernst equation for a given state of charge, allowing for estimation of the electrochemical potential at which the reduction reactions are occurring.[29,31] During the reaction this potential will

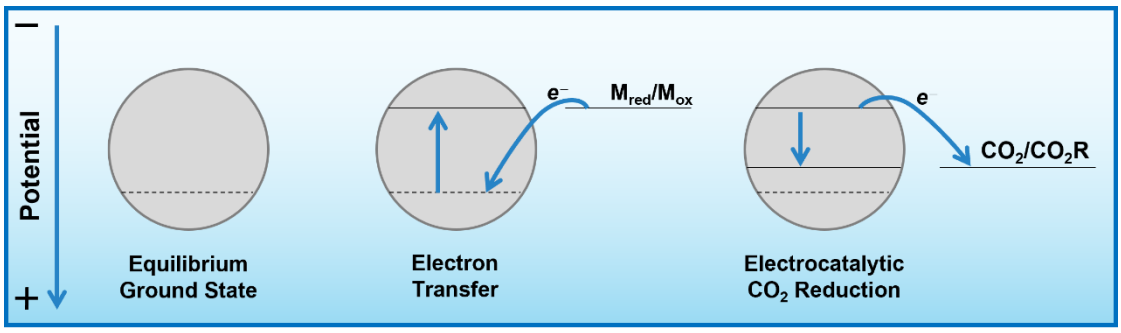

Figure 4.13 *Energy level diagram indicating the change in Fermi level of the catalyst during redox mediated ECO_2R.*

be controlled by the rate limiting reaction step; either the electron transfer from mediator to catalyst, or more likely the initial electron transfer to CO_2 by the catalyst.[32] If the electron transfer is much faster than the reduction of CO_2, the Fermi level of the catalyst will be that of the solution, while if the CO_2 reduction step is much faster, the Fermi level of the catalyst will be the thermodynamic potential required for the given product. If the rates are similar, the potential will be somewhere between these two values. As the batch reaction proceeds, the electrochemical potential of the solution will shift as the ratio of reduced to oxidised mediator changes. The potential applied by the solution, assuming ideal Nernstian behaviour, will give a window around the E^0 of the mediator of approximately 237 mV for a realistic state of charge range 1-99%.

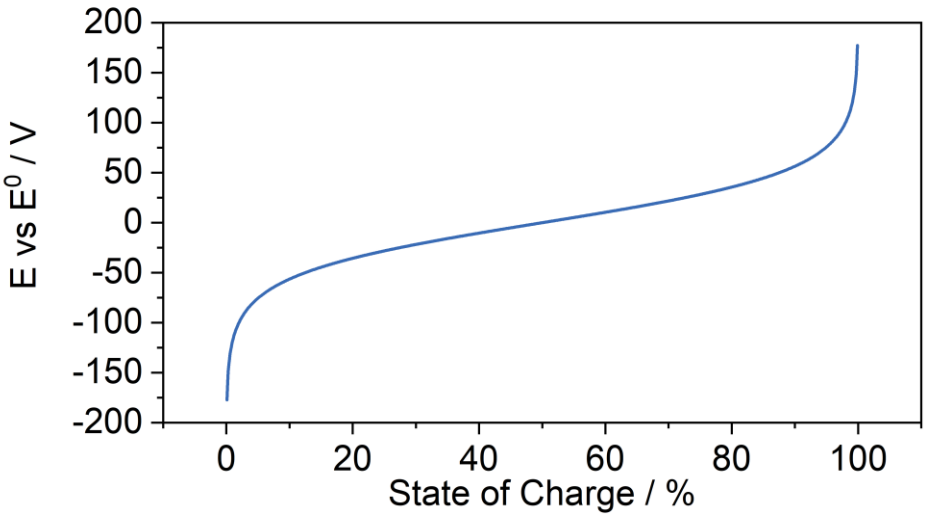

Figure 4.14 *Graph of the potential of the mediator solution relative to the standard potential of the redox couple as a function of state of charge according to the Nernst equation.*

It is proposed that Bi favours CO_2R when deployed in the decoupled reaction not because it is an especially good catalyst for ECO_2R (high operating potential and low current density compared to many other ECO_2R catalysts), but because HER is highly disfavoured. The mechanism by which Bi electrochemically reduces CO_2 is typically assumed to be a predominantly outer-sphere process in which the electron is inserted into a weakly interacting CO_2 molecule.[9,24,33–36] This reduced intermediate is not formally adsorbed on the catalyst surface, though it is retained near the surface through weak interactions with the oxygen atom(s). The resulting radical intermediate is highly energetic and will quickly react with a nearby molecule which, in typical aqueous ECO_2R conditions, is likely to be H_2O or HCO_3^-. An *OCHO intermediate is then formed, which is key to directing the catalyst selectivity towards formate as the major product. The intermediate then undergoes further reduction and $HCOO^-$ is released.

The selectivity and low overpotential requirement of the Bi RD is explained as being due to the high degree of shape control in which only two crystal facets are primarily exposed (104 and 110).[17] These facets are predicted to stabilise the *OCHO intermediate much more than the lowest energy facet (012), and are predicted to have a greater difference between the binding energies of the key CO_2R and HER intermediates. The high degree of stabilisation of the intermediates drastically reduces the activation energy needed for formate production, lowering the overpotential required for its production, thus improving selectivity by further impeding the competing HER, allowing for high selectivity over a wide potential range.

As a product, formic acid has many industrial uses, and has also been considered as an energy carrier to replace those derived from fossil fuels, both directly in fuels cells and as a hydrogen carrier.[37,38] Formate/formic acid is typically considered the end of its reduction chain, unlike the other two-electron reduction product, CO, which is considered a key intermediate in the pathways toward the further reduced products observed on copper electrocatalysts.[39] It has, however, been reported that on select catalysts, formic acid can be reduced to methanol, albeit with low current density and poor selectivity.[40–42] The primary difficulty with formate/formic acid as a product is the need for intricate separation procedures, which is further complicated in the decoupled system by the redox meditator. It is desirable for the mediator to be indefinitely reusable in a semi-closed system where only CO_2 and water are added and products are collected. Gaseous products such as H_2 and CO are optimal, as they spontaneously

separate allowing for direct extraction and purification without processing the liquid electrolyte. The same is not true for liquid products, which require invasive extraction techniques to occur as a function within the system to maintain reusability of the mediator and electrolyte. A better understanding of the mechanism in decoupled CO_2 reduction may enable catalyst design to promote the CO reduction route and deliver gaseous or highly volatile products for ease of separation.

4.4 Conclusions

Decoupled electrochemical CO_2 reduction to formate has been successfully demonstrated using a tailored bismuth catalyst, serving as a valuable proof-of-concept. The highest selectivity towards formate was 85% (FE 38%) and in all cases the competing HER contributed a significant portion of the products formed. Total faradaic yields ranged between 45-60%, indicating an inefficiency in the experimental design attributed to discharge of the mediator through unquantified pathways that remain to be identified. As discussed, the principal limiting factor for DECO_2R is the redox potential of the mediator, which is constrained by the water solvent window. Cr PDTA, with its particularly negative redox couple, is able to provide as much driving force as is practically feasible for the reaction, and when paired with a catalyst material that is selective at this low operating potential can achieve the same level of selectivity as conventional electrocatalysis.

Further opportunities include widening catalyst scope to improve selectivity and faradaic efficiency, and to enable different products (primarily CO); testing new mediators which may provide improved electron transfer efficiency, a greater driving force (more negative redox potential), and co-catalytic effects such as proton/CO_2 shuttling. Furthermore, changes in medium, such as moving to a non-aqueous environment, may improve the system by enabling use of redox mediators operating at much more negative potentials, drastically increasing CO_2 solubility and allowing greater control of proton availability to supress the competing HER. Ultimately, implementation of DECO_2R into a flow system will allow the extension of the ‘dual circuit flow battery’ to products other than hydrogen that may be more practical and /or valuable. To this end, the key challenges remain supressing hydrogen evolution and targeting products that are easily extracted.

4.5 References

1 M. Potter, D. E. Smith, C. G. Armstrong and K. E. Toghill, *EES Catal.*, 2024, **2**, 379–388.

2 V. Amstutz, K. E. Toghill, F. Powlesland, H. Vrubel, C. Comninellis, X. Hu and H. H. Girault, *Energy Environ. Sci.*, 2014, **7**, 2350–2358.

3 D. Reynard and H. Girault, *Cell Reports Phys. Sci.*, 2021, **2**, 100556.

4 Y. Hori, K. Kikuchi and S. Suzuki, *Chem. Lett.*, 1985, **14**, 1695–1698.

5 A. Somoza-Tornos, O. J. Guerra, A. M. Crow, W. A. Smith and B. M. Hodge, *iScience*, 2021, **24**, 102813.

6 Y. Hori, A. Murata and R. Takahashi, *J. Chem. Soc. Faraday Trans. 1 Phys. Chem. Condens. Phases*, 1989, **85**, 2309–2326.

7 Y. Hori, I. Takahashi, O. Koga and N. Hoshi, *J. Mol. Catal. A Chem.*, 2003, **199**, 39–47.

8 Y. Hori, H. Konishi, T. Futamura, A. Murata, O. Koga, H. Sakurai and K. Oguma, *Electrochim. Acta*, 2005, **50**, 5354–5369.

9 Y. Hori, H. Wakebe, T. Tsukamoto and O. Koga, *Electrochim. Acta*, 1994, **39**, 1833–1839.

10 M. C. O. Monteiro, M. F. Philips, K. J. P. Schouten and M. T. M. Koper, *Nat. Commun.*, 2021, **12**, 1–7.

11 M. H. Hicks, W. Nie, A. E. Boehme, H. A. Atwater, T. Agapie and J. C. Peters, *J. Am. Chem. Soc.*, DOI:10.1021/jacs.4c09512.

12 Y. H. Wen, H. M. Zhang, P. Qian, H. T. Zhou, P. Zhao, B. L. Yi and Y. S. Yang, *Electrochim. Acta*, 2006, **51**, 3769–3775.

13 C. Noh, Y. Chung and Y. Kwon, *J. Power Sources*, 2020, **466**, 228333.

14 C. Noh, Y. Chung and Y. Kwon, *Chem. Eng. J.*, 2021, **405**, 126966.

15 A. Hollas, X. Wei, V. Murugesan, Z. Nie, B. Li, D. Reed, J. Liu, V. Sprenkle and W. Wang, *Nat. Energy*, 2018, **3**, 508–514.

16 B. H. Robb, J. M. Farrell and M. P. Marshak, *Joule*, 2019, **3**, 2503–2512.

17 H. Xie, T. Zhang, R. Xie, Z. Hou, X. Ji, Y. Pang, S. Chen, M. M. Titirici, H. Weng and G. Chai, *Adv. Mater.*, 2021, **33**, 1–10.

18 W. Zhang, Y. Hu, L. Ma, G. Zhu, Y. Wang, X. Xue, R. Chen, S. Yang and Z. Jin, *Adv. Sci.*, 2017, 170275.

19 M. Hecht, F. A. Schultz and B. Speiser, *Inorg. Chem.*

20 B. Li, M. Gu, Z. Nie, Y. Shao, Q. Luo, X. Wei, X. Li, J. Xiao, C. Wang, V. Sprenkle and W. Wang, *Nano Lett.*, 2013, **13**, 1330–1335.

21 A. D. Proctor, B. H. Robb, J. D. Saraidaridis and M. P. Marshak, *J. Electrochem. Soc.*, 2022, **169**, 030506.

22 J. Greeley, T. F. Jaramillo, J. Bonde, I. Chorkendorff and J. K. Nørskov, *Nat. Mater.*, 2006, **5**, 909–913.

23 Y. Hori, *Mod. Asp. Electrochem.*, 2008, 89–189.

24 Y. Guan, M. Liu, X. Rao, Y. Liu and J. Zhang, *J. Mater. Chem. A*, 2021, **9**, 13770–13803.

25 F. Y. Gao, R. C. Bao, M. R. Gao and S. H. Yu, *J. Mater. Chem. A*, 2020, **8**, 15458–15478.

26 R. Ge, J. Huo, M. Sun, M. Zhu, Y. Li, S. Chou and W. Li, *Small*, 2021, **17**, 1903380.

27 M. D. Porosoff, X. Yang, J. A. Boscoboinik and J. G. Chen, *Angew. Chemie - Int. Ed.*, 2014, **53**, 6705–6709.

28 B. Deng, M. Huang, X. Zhao, S. Mou and F. Dong, *ACS Catal.*, 2022, **12**, 331–362.

29 M. D. Scanlon, P. Peljo, M. A. Méndez, E. Smirnov and H. H. Girault, *Chem. Sci.*, 2015, **6**, 2705–2720.

30 R. Khakpour, D. Lindberg, K. Laasonen and M. Busch, *ChemCatChem*, 2023, e202201671.

31 A. J. Bard and L. R. Faulkner, *Electrochemical Methods: Fundamentals and Applications*, John Wiley & Sons, Ltd, 2nd edn., 2001.

32 D. Reynard, G. Bolik-Coulon, S. Maye and H. H. Girault, *Chem. Eng. J.*, 2021, **407**, 126721.

33 J. P. Jones, G. K. S. Prakash and G. A. Olah, *Isr. J. Chem.*, 2014, **54**, 1451–1466.

34 B. Zhang, Y. Wu, P. Zhai, C. Wang, L. Sun and J. Hou, *Chinese J. Catal.*, 2022, **43**, 3062–3088.

35 C. W. Lee, N. H. Cho, S. W. Im, M. S. Jee, Y. J. Hwang, B. K. Min and K. T. Nam, *J. Mater. Chem. A*, 2018, **6**, 14043–14057.

36 X. Du Liang, N. Tian, S. N. Hu, Z. Y. Zhou and S. G. Sun, *Mater. Reports Energy*, 2023, **3**, 100191.

37 C. Rice, S. Ha, R. I. Masel, P. Waszczuk, A. Wieckowski and T. Barnard, *J. Power Sources*, 2002, **111**, 83–89.

38 J. Eppinger and K. W. Huang, *ACS Energy Lett.*, 2017, **2**, 188–195.

39 T. K. Todorova, M. W. Schreiber and M. Fontecave, *ACS Catal.*, 2020, **10**, 1754–1768.

40 P. G. Russell, N. Kovac, S. Srinivasan and M. Steinberg, *J. Electrochem. Soc.*, 1977, **124**, 1329–1338.

41 S. Kapusta and N. Hackerman, *J. Electrochem. Soc.*, 1983, **130**, 607–613.

42 D. Winkler, V. Dietrich, C. Griesser, N. S. Nia, E. Wernig, M. Tollinger and J. Kunze-Liebhäuser, *Electrochem. Sci. Adv.*, 2022, **2**, 1–9.

Chapter 5: Rapid Decoupled Electrochemical Reduction of CO_2 to Syngas

5.1 Introduction

Having successfully enabled DECO_2R using Cr PDTA a redox mediator in Chapter 4, the next step was to expand catalyst scope to enable other products. While formic acid is an industrially relevant compound, it has a relatively low market cap due to limited uses. As a product with a boiling point over 100°C, and as an acid that will exist as a salt at this pH, it will be very energy intensive to extract it from the mediator solution as part of a continuous process. Targeting instead gaseous products, such as CO, would allow for spontaneous product separation which would be much more practical to implement. As a product, CO offers to be much more relevant to the ongoing objective of carbon neutrality. Currently, CO is sourced from the processing of fossil fuels, and as mentioned in the introduction, can be used alongside renewably generated H_2 in the production of a wide range of hydrocarbons using the Fischer-Tropsch process.

Of the CO producing catalysts, the noble metals gold and silver tend to be the most selective and active.[1,2] Gold in particular sits atop the volcano plot for CO selectivity due to favourable binding with the key reduction intermediate *COOH, while having poor binding with the formate favouring *OCHO intermediate and the competing HER *H intermediate.[3,4] Gold nanoparticles, often supported on carbon substrates, are commonly reported to reduce CO_2 to CO with high selectivity and efficiency at relatively low overpotentials.[5–8] As such, gold based catalysts are the focus of this chapter.

Decoupled approaches to synthesis offer potential advantage in the rapid conversion of CO_2 to CO_2R to products, by optimising reaction conditions towards more favourable kinetics. However, with the use of a liquid phase redox mediator, it is imperative that the reaction products be readily separated from the reaction medium to make the process practicable. With this in mind, we sought to extend the CO_2 reduction of the preceding chapter, enabled using a Cr complex with a highly reducing redox potential of -0.6 V vs RHE and high stability in carbonate solution, to achieve only gaseous products. Specifically, the use of carbon supported gold nanoparticles with polyvinyl alcohol (PVA) capping resulted in the rapid evolution of syngas (CO and H_2), the composition of which could be varied using different amounts of PVA in nanoparticle synthesis. Furthermore, an initial assessment into scaling up the process was

performed to determine how it might compare to state-of-the-art conventional catalysis such as GDE flow cells with practical current densities above 200 mA cm^{-2}.[9]

5.2 Experimental

5.2.1 Materials

All chemicals were used as purchased without further purification. Sodium borohydride (99%), carbon black (99.9%), cetyltrimethylammonium bromide (CTAB, 99%), 4-aminothiophenol (97%), sodium chloride (99.5%) potassium chloride (99.5%), potassium hydrogen carbonate (99.7%) and methanol (99%) were purchased from Thermo Fisher (Alfa Aesar, Acros Organics). Chloroauric acid trihydrate (99.9%), ascorbic acid (99%) and polyvinyl alcohol (9000-10000 mw, 80% hydrolysed) were purchased from Merck (Sigma Aldrich). CO_2 was purchased from BOC ltd.

5.2.2 Synthesis

$KCrPDTA{\cdot}3H_2O$ was synthesised as previously reported in chapter 4.

5.2.2.1 Shape controlled Au nanoparticle synthesis

Initially, small seeds were formed by rapid reduction, in which solutions of $HAuCl_4$ (10 mM, 250 µL) and $NaBH_4$ (10 mM, 800 µL) were added to a solution of hexadecyltrimethylammonium bromide (CTAB) (100 mM, 7.5 mL). This was held at 30°C for 3 hours to ensure complete decomposition of any remaining $NaBH_4$, after which it was diluted 10x with ultrapure water. They were then grown further by adding this seed solution (5µL) to a solution comprising $HAuCl_4$ (10 mM, 200 µL), CTAB (100 mM, 1.6 mL), and ascorbic acid (50 mM, 950 µL). These nanoparticles were washed by centrifugation and redispersion in ultrapure water.

These seeds were then added to a second growth solution containing CTAB (100 mM, 0.8 mL), ultrapure water (3.95 mL), $HAuCl_4$ (10 mM, 100 µL), ascorbic acid (100 mM, 475 µL), and 4-ATP (5 mM, 0.5 µL) all mixed into the solution consecutively. 4-ATP was dissolved in DMSO while all other chemicals were prepared in ultrapure water. The final nanoparticles were washed by centrifugation and redispersion in ultrapure water ready for use.

5.2.2.2 Au/TiO_2 Synthesis

Gold on titania (2 wt.%) was synthesised according to a reported procedure. P25 titania (600 mg) was added to a solution of $HAuCl_4$ (2mM, 30 mL) in a mixture of 1:1 water:methanol (volume:volume). The mixture was irradiated with a blue LED lamp (40w) with constant stirring for 80 minutes under a continuous flow of N_2. Over this time

the initially white powder turned purple. The resulting Au/TiO_2 was collected by filtration and dried ready for use.

5.2.2.3 Au/C synthesis

In-situ PVA deposition

Gold nanoparticles supported on carbon black (20 wt.% gold) with polyvinyl alcohol capping were synthesised by a straightforward two-step synthesis according to existing literature.[5] Gold nanoparticles were initially formed by the rapid reduction of $HAuCl_4$ by $NaBH_4$ in the presence of PVA, after which carbon black was added along with NaCl to destabilise the dispersion and hasten the impregnation. The salts were then removed by centrifugation and redispersion in DI water, which was then evaporated at 50°C resulting in a fine black powder.

Residual PVA deposition

Au/C 20 wt.% was initially synthesised by rapid reduction of $HAuCl_4$ by $NaBH_4$ in the absence of any polymer. To this carbon black was added along with NaCl solution. The resulting powder was then washed and dried as above. A known amount of Au/C was then redispersed in DI water, to which PVA solution was added to produce a range of loadings. The dispersion was stirred for 4 hours, then dried overnight at 50 °C. Further samples were prepared from a commercial Au/C 20 wt.% by the same method for comparison.

5.3 Results

5.3.1 Initial Screening

Promising materials for CO_2 conversion to CO were selected from existing literature, with a focus on high selectivity at low overpotentials. As with bismuth in the previous chapter, the first gold nanostructured material chosen was promised to improve CO selectivity via shape control of the nanomaterial. Through the use of a specific thiol additive, 4-aminothiophenol, it was reported that concave rhombic dodecahedra can be synthesised, which achieved CO selectivity over 90% in the −0.5 to −0.7 V vs RHE range.[6] Attempting to reproduce this material however proved much more challenging than it appeared. Repeating the vaguely described procedure resulted in gold nanoparticles with no shape control. As shown in Figure 5.1, a variety of shapes including prisms, rods and polyhedrons were all produced. After several attempts at replicating the reported material, they were deemed too problematic to synthesise. The nanoparticles that were synthesised were tested for $DECO_2R$ regardless, with CO

making up 10% of the observed product. While still a minor product, this a huge improvement over the 1% previously observed using the gold mesh in Chapter 4.

It was decided that supported nanoparticles would be a better choice as catalysts, as it will be easier to sperate them from the mediator solution post reaction. Titania (TiO_2) is a commonly used support in heterogeneous catalysis and photoelectro-catalysis.[10] Gold on titania has been reported for a range of reactions including the oxidation of alcohols and photoelectroreduction of water. A sample of Au/TiO_2 with a 2 wt.% loading of gold was prepared by photoreduction under blue light. The powder suspension turned from white to purple as expected, and comparison of XRD diffractograms of the pristine and synthesised material displayed peaks indicating the successful deposition of gold. When deployed as a catalyst for $DECO_2R$, CO only accounted for about 1% of the faradaic yield, or about 1.5% of the observed products. Clearly this material is a poor catalyst for CO_2R, which is not entirely unexpected given the previous demonstration of gold on titania as a catalyst for photo- and photoelectro-catalytic water splitting.

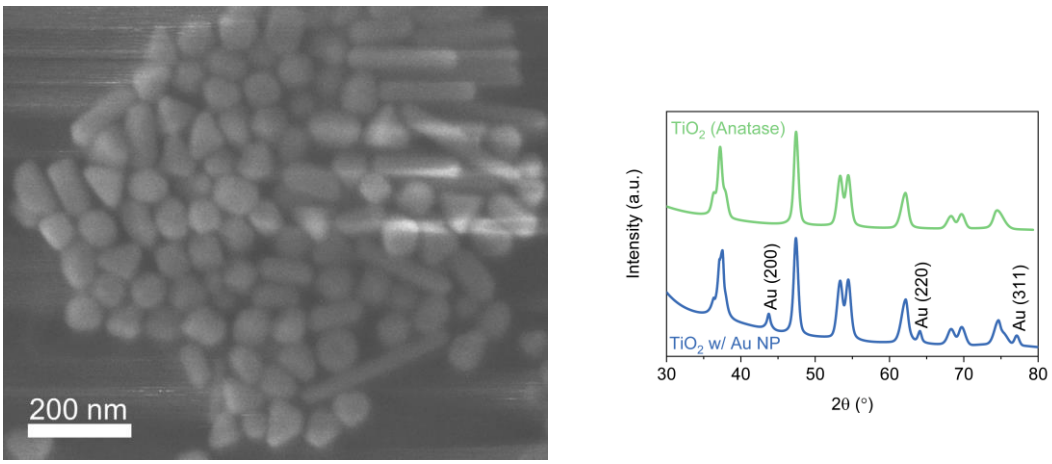

Figure 5.1 *(Left) SEM image of mixed shape nanoparticles. (Right) XRD diffractogram of pristine TiO_2 and TiO_2 with photo-deposited gold nanoparticles.*

While it was envisioned that the unique kinetics of the decoupled system would not require the catalyst/support to be electronically conductive, the vast majority of materials reported for CO_2R use conductive supports/additives like carbon black. One such material, which also utilised polyvinyl alcohol as a capping agent, was reported to have CO selectivity above 90% for the full potential range −0.4 V to −0.8 V vs RHE.[5] Synthesis proved facile, and when deployed as a catalyst for $DECO_2R$ resulted in a CO selectivity over 40%. This material was chosen as the basis for further optimisation of the $DECO_2R$ process towards gas products.

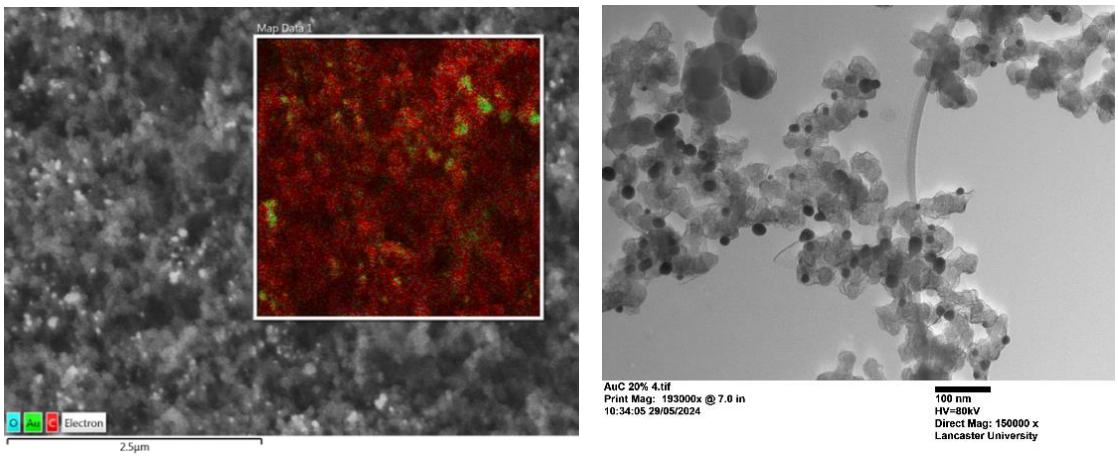

Figure 5.2 *(Left) SEM EDX of Au/C. (Right) TEM of Au/C.*

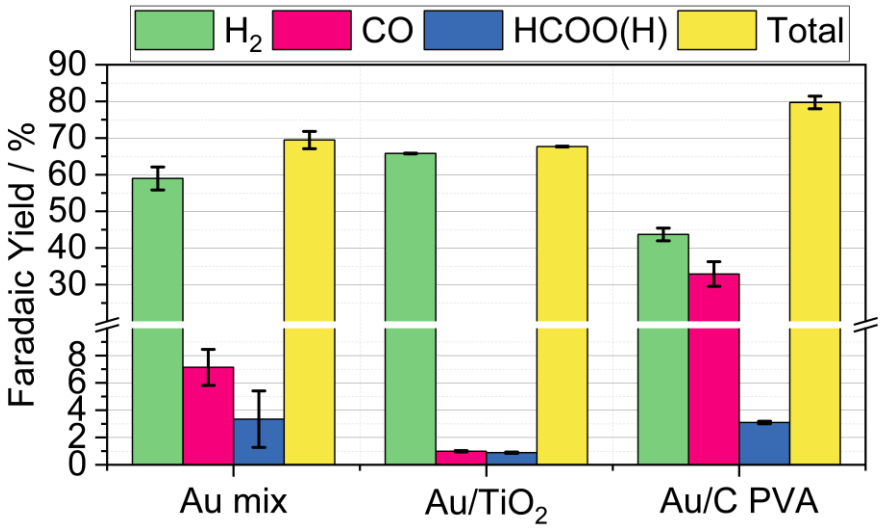

Figure 5.3 *Column chart indicating the average faradaic yields of H_2 (green), CO (pink), HCOO(H) (blue), and in total (yellow) measured when 20 mL aliquots of 10 mM Cr PDTA were discharged over the gold based heterogenous catalysts inside a sealed CO_2 atmosphere, with error bars indicating the standard deviation within each triplicate set.*

5.3.2 Controlling product ratio with PVA capping

Polymer binders are often required to ensure the catalyst remains attached to the electrode in conventional electrocatalysis, however, they often provide beneficial effects beyond improving the mechanical stability of the catalyst layer. Nafion remains the most popular choice of binder, due to its high durability and ability to conduct protons. However, recent studies have suggested than Nafion can have detrimental effects on the CO_2 reduction reaction. In some examples of copper catalysed CO_2R,

using too much Nafion binder reduced selectivity towards the preferred C_2 product ethylene, in turn increasing the proportion of H_2, and to a lesser extent CO, produced.[11]

Despite the popularity of Nafion, many alternatives have been explored.[12] The chemical effects of binders can typically be classified into two main categories based on their functionalisation; hydrophobic and hydrophilic. The way this functionality interacts with the catalyst surface can influence product selectivity by either stabilising or destabilising the competing reaction intermediates. For the case of the gold catalysed reduction of CO_2 to CO, it was found that the CF_2 groups in the hydrophobic binders PTFE and PVDF improved CO selectivity primarily by destabilising the adsorbed hydrogen intermediate, while the hydrophilic binders PVA and PAA improved CO selectivity by also stabilising the adsorbed CO_2R intermediate.[13] At the lower end of the overpotential range between −0.5 V to −0.7 V vs RHE all the binders, except PAA, resulted in similar performance within error. Only at the higher overpotentials up to −1.0 V vs RHE was a categorical improvement observed, in which the hydrophobic binders were notably more selective towards CO than the hydrophilic ones.

As it is currently employed however, $DECO_2R$ does not require the use of binders for mechanical stability. That however does not mean that the beneficial effects of these polymers on the chemical environment cannot be exploited. Having successfully achieved CO as a major product using PVA to improve selectivity, a further exploration on the effects of the PVA loading was performed. It was previously reported that increasing the amount of PVA coverage on the catalyst further improved CO selectivity during bulk electrolysis experiments performed at a relatively mild potential of −0.4 V vs RHE. A series of PVA loadings between 0 and 30 wt.% were prepared by increasing the amount of PVA present during nanoparticle formation. The % PVA quoted is the wt.% of PVA added to the solution compared to the total weight of gold and carbon.

High resolution STEM imaging of the PVA free material was compared to the 15% PVA material, which indicated the presence of PVA during nanoparticle formation resulted in a narrower range of particle sizes. Further, the dispersity of the gold over the carbon is much higher when PVA was present. For the PVA free sample, large patches of carbon free of gold nanoparticles were observed, while for the 15% PVA sample, very little carbon free of gold was observed. This can be rationalised by the observation that gold nanoparticle impregnation occurred much more rapidly in the sample free of PVA than in samples that contained PVA. The rapid impregnation likely resulted in poor dispersity because the hydrophobic carbon could not be mixed in fast enough, while

nanoparticles capped with PVA were captured more slowly, allowing for the carbon to be thoroughly mixed during impregnation.

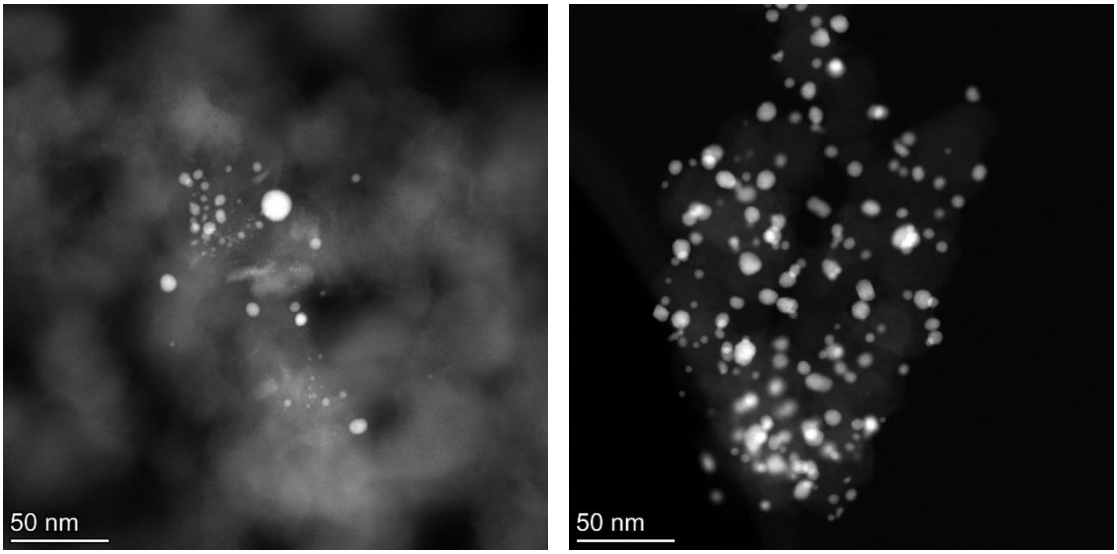

Figure 5.4 *(Left) STEM of Au/C without polymer capping. (Right) STEM of Au/C 15% PVA in-situ deposition*

5.3.3 Electrochemical Characterisation and Conventional Performance

To test the material against what had previously been reported, it was prepared for conventional electrode voltammetry and bulk electrolysis. The PVA loading of the material used in these tests was 7.5 wt.%. Linear sweep voltammetry with 1 M KCl supporting electrolyte displays a clear diffusion limited peak in the presence of CO_2, suggesting good activity and selectivity for CO_2R. Reduction appeared to be onset around −0.3 V vs RHE, becoming diffusion limited at −0.7 V vs RHE. The peak was less defined in $KHCO_3$ electrolyte, however a clear shift in onset potential and increase in current plateau was observed when switching from N_2 to CO_2 atmosphere. LSV performed in electrolyte containing 10 mM Cr PDTA displayed no clear current response as a result of its presence, however the overlap in potential is a good indication that $DECO_2R$ is energetically favourable.

Bulk electrolysis in a conventional H-cell was performed using the Au/C 15% PVA across a range of applied potentials close to that which the mediator could be expected to provide. Results indicated a reasonably high selectivity for CO, although not as high as previously reported.[5] The highest selectivity was observed at −0.656 V vs RHE, with CO making up 90% of the observed products. The observed current density was however much lower than the previously reported 98.6 mA cm^{-2} at −0.77 V vs RHE, at only 2.50 mA cm^{-2} at −0.756 V vs RHE. Hydrogen was the only observed side product

of the reaction. The use of Nafion binder proved necessary for stability of the catalyst layer and could not be omitted, the presence of which may affect catalyst performance.

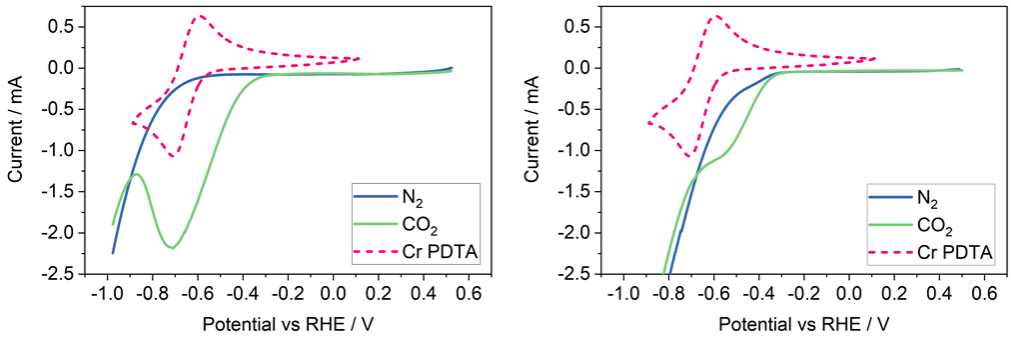

Figure 5.5 *Linear sweep voltammetry of Au/C 15% PVA catalyst drop cast onto a glassy carbon electrode with Nafion binder, under N_2 and CO_2 atmospheres. The potential was swept from positive to negative at a rate of 100 mV s^{-1} in a three-electrode cell. The supporting electrolyte was 1 M KCl (Left) and 1 M $KHCO_3$ (Right) respectively.*

Table 5.1 *Results of conventional H-cell ECO_2R using Au/C 15% PVA cast onto a glassy carbon plate working electrode of area. Potentials are referenced vs RHE assuming a pH of 7.5 for CO_2 saturated 1 M $KHCO_3$. Drop casting was achieved using a Nafion binder with a catalyst to binder ratio of 9:1 and a density of 1 mg cm^{-2}.*

Applied potential (V) vs RHE	%FE (H2)	%FE (CO)	TFE	% FE of CO	FE(CO)/ FE(H2)	Total Charge passed (C)
-0.856	16.51	59.49	76	78	3.6	6.226
-0.756	15.78	63.87	79.65	80	4.0	4.957
-0.656	8.04	70.66	78.7	90	8.8	3.646
-0.556	23.2	67.53	90.73	74	2.9	2.723

5.3.4 Mediated Reduction

The series of catalysts was then deployed for $DECO_2R$ by the same batch method used in the preceding chapter. Starting with Au/C catalyst prepared in the absence of PVA, a CO selectivity of just 21.0% was observed. The addition of even a small amount of PVA during nanoparticle synthesis, just 2.5 wt.%, jumped the CO selectivity up to 47.0%, effectively producing a syngas of about 1:1 H_2:CO. Doubling this to 5.0 wt.% pushed CO selectivity to 52.3%, and this trend continued linearly up until 15 wt.% PVA, at which point the CO selectivity was 70.1%, producing a syngas of around 1:2 H_2:CO. Further increasing the PVA content saw a slight decline in CO selectivity, falling back

to 66.7% of the observed product. Faradaic efficiency remained in the low to mid 80% range for the lower wt.% samples, while it began to fall at 15 wt.% to just over 70%, then even lower at just below for the 30 wt.% sample. A small amount of formate was consistently produced, which is not attributed to the gold catalyst as none was observed in the conventional H-cell testing.

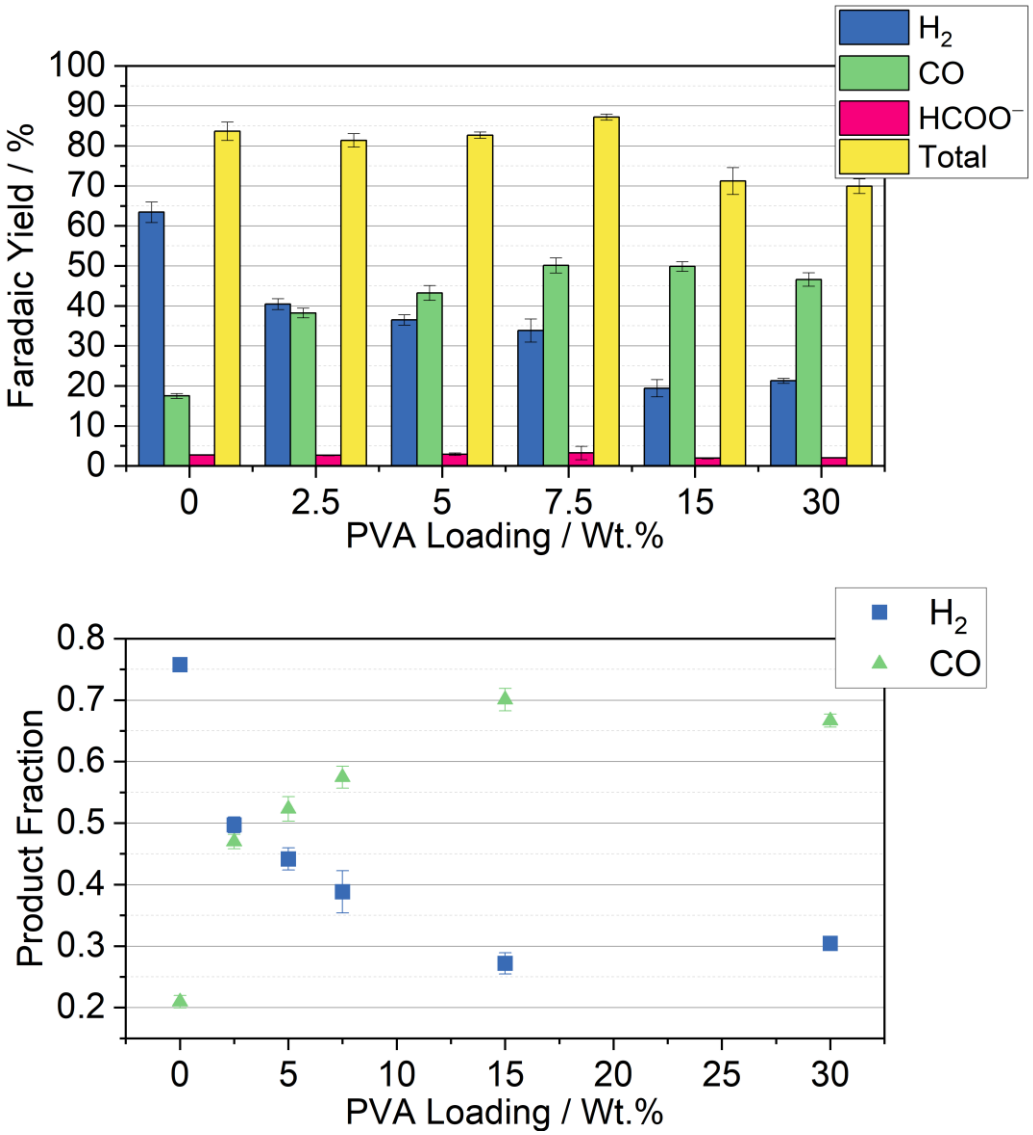

Figure 5.6 *(Top) Column chart indicating the average faradaic yields of H_2 (green), CO (pink), HCOO(H) (blue), and in total (yellow) measured when 20 mL aliquots of 10 mM Cr PDTA were discharged over the Au/C PVA heterogenous catalysts inside a sealed CO_2 atmosphere, with error bars indicating the standard deviation within each triplicate set. (Bottom) Fraction of the observed products provided by H_2 and CO across the range of PVA loadings.*

5.3.5 Residual PVA Deposition

As an alternative method of catalyst preparation, a further series of materials were prepared in which the PVA was added after the impregnation of the gold nanoparticles onto the carbon. These materials were all prepared form the same batch of Au/C. The addition of PVA by this method had a similar effect for the first two PVA loadings tested as the material where the nanoparticles were formed in the presence of PVA. Further increasing the loading however resulted in no further improvement in CO selectivity, where all the loadings gave approximately the same 1:1 H_2:CO ratio within error.

A further set of samples were prepared from a commercial Au/C catalyst material by the same method, with the same gold loading as the materials prepared in house. The addition of PVA to this material resulted in no real improvement of CO selectivity within error, however.

Table 5.2 *Faradaic yields and product selectivity observed using the residually capped Au/C PVA catalysts.*

Au/C Catalyst	**Overall Faradaic Efficiency (%)**	**Product ratio (% of observed products)**		
		H_2	CO	$HCOO^-$
Commercial Au/C no PVA	77.80 ± 0.8	75.95 ± 2.66	20.33 ± 2.72	3.72 ± 0.21
Commercial Au/C 2.5% PVA	77.86 ± 2.0	74.88 ± 4.89	22.33 ± 4.75	2.79 ± 0.16
Commercial Au/C 7.5% PVA	77.42 ± 1.1	76.18 ± 2.33	21.03 ± 2.34	2.79 ± 0.10
In-house Au/C				
0% PVA	83.7 ± 2.3	75.8 ± 1.2	21.0 ± 1.0	3.3 ± 0.19
2.5% PVA	77.5 ± 1.7	52.46 ± 2.09	44.29 ± 2.36	3.25 ± 0.30
5.0% PVA	75.7 ± 0.21	44.02 ± 2.95	53.03 ± 2.95	2.95 ± 0.06
7.5% PVA	81.96 ± 0.53	46.22 ± 0.79	49.44 ± 0.90	4.34 ± 0.12
10.0% PVA	80.02 ± 1.5	47.42 ± 0.62	48.76 ± 0.75	3.82 ± 0.23
15.0% PVA	81.8 ± 01.1	47.47 ± 2.48	48.35 ± 2.62	4.18 ± 0.15

5.3.6 Towards Continuous and Rapid Conversion

In the existing screening method, only a small amount of the total CO_2 is consumed during reduction, even if 100% faradaic efficiency was observed. Assuming a typical flask volume of 170 mL, the headspace volume after mediator injection would be 150 mL. Assuming a molar volume of 24.0 L mol^{-1} at 20 °C and atmospheric pressure, this would result in 6.25 mmol of CO_2 gas in the headspace. The solubility of CO_2 in water is approximately 37 mM under one atmosphere of pressure, adding a further 0.74 mmol of CO_2, for approximately 7 mmol of total CO_2 available. 20 mL of 10 mM mediator is able to provide 0.2 mmol of electrons, and assuming only two-electron reduction products are observed, would allow for the conversion of 0.1 mmol of CO_2, or 1.43% of the total available. Scaling the mediator concentration up to 0.1 M would now result in the total possible CO_2 conversion being 14.3 %. Quantification of products for this level of conversion would present considerable challenge due to saturation of the chromatography column and detector.

Further, because there is no counterbalancing half reaction in the batch system, the pH will be increased relative to the total number of electrons transferred. Whether by the intended catalysis or parasitic side reaction such as with trace oxygen, the result of most of the possible reactions will include the formation of hydroxide anions. These will alter the pH of the electrolyte over time; however, this will be balanced to a degree by reaction with dissolved CO_2 in the form of carbonic acid, resulting in the further consumption of the available CO_2 to carbonate anions.

In an effort to determine if the DECO_2R reaction can be practically scaled up, the concentration of the mediator was increased. At this concentration, CO_2 mass transport and its overall availability is now likely to limit the reaction. To alleviate this, the system was modified with a continuous flow of CO_2 through the electrolyte. This has the added benefit of allowing for semi-continuous measurement of product concentration in the outflowing gas. The concentration of CO and H_2 in the outflowing gas was measured every 15 minutes until the mediator was fully depleted. Completion was determined by a combination of colour change and the return of the O_2 peak from trace air contamination introduced into the flow cell that could not be eliminated. While the mediator still possesses charge, oxygen will be reduced, lowering the observed peak area in the GC trace. This will reduce the overall faradaic efficiency of the observed products.

5.3.7 Online Analysis

Online batch $DECO_2R$ was performed using a round bottom flask as a makeshift reactor as described in Chapter 2. In the first instance, 48 mL of 0.1 M Cr PDTA mediator were injected into the reactor, which contained 2 mg of the Au/C 15% PVA catalyst found to give the best CO selectivity of the materials tested. This would allow for a theoretical total of 2.4 mmol of two-electron products, which if gaseous would occupy a volume of 57.6 mL at room temperature and pressure. A continuous flow of CO_2 was passed through the reactor at a rate of 10 $mLmin^{-1}$, after which its composition was analysed by GC every 15 minutes. The gas was collected in a Tedlar® gas sampling bag, and its final composition was checked for comparison.

Figure 5.7 shows how the composition of the outflowing gas changed over the course of the experiment. The yield predicted from the area under the graph was 24.92 mL of H_2 and 19.07 mL of CO, out of the possible 57.6 mL for a total FE of 76.37%. The yield found by measuring the concentration of gasses in the Tedlar® bags however was much higher, at 47.65% FE for H_2 and 41.30% FE for CO (TFE: 88.95%). Product selectivity was estimated at 56.6% and 53.6% towards H_2 for the two analysis methods.

Assuming the reaction was complete in 120 minutes, the time it took for the O_2/N_2 ratio to return to that of air, then the current of the experiment was 64.3 mA, or the current

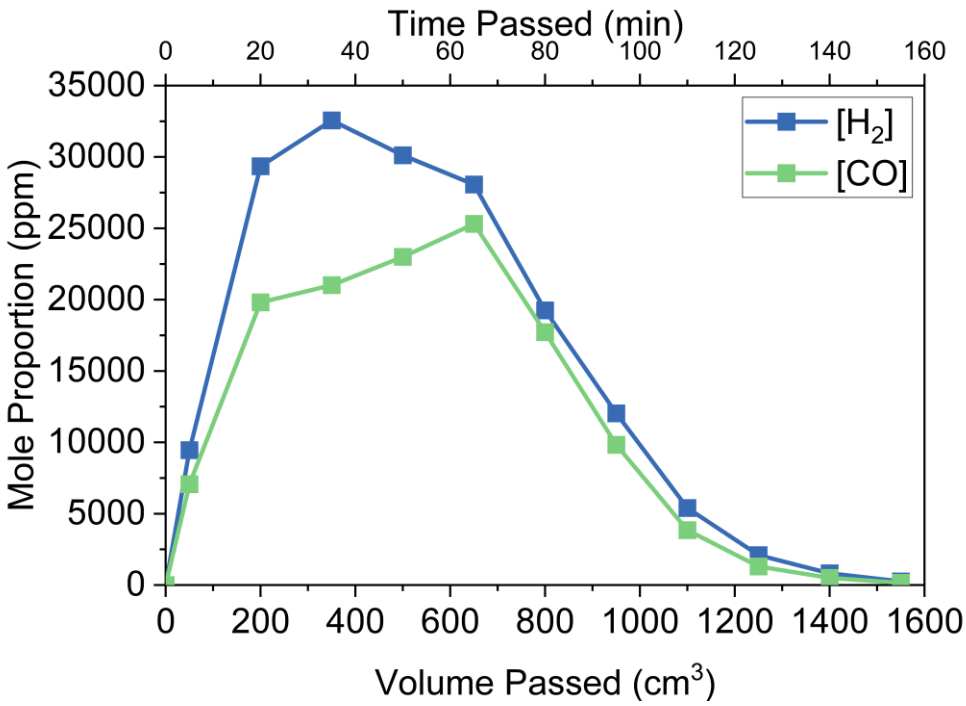

Figure 5.7 *Concentration of the reduction products H_2 and CO in the outflow gas during continuous online reduction of CO_2 using the Au/C 15% PVA catalyst with 20 mL of 0.1 M Cr PDTA mediator.*

density was 32.2 mA mg^{-1}. In this instance, current is approximated as the rate at which the capacity of the mediator is depleted. When multiplied by the observed faradaic efficiency, this would make the product specific current density 28.7 mA mg^{-1}.

The experiment was then scaled up even further, now using 20 mL of 0.5 M Cr PDTA mediator for a total possible 5 mmol of two-electron products, or gaseous volume of 120 mL. Again, the discharge took an average of 120 minutes, however due to the increase in overall charge passed, the average current density is now higher at 67.0 mA mg^{-1}. The amount of CO produced was consistent, at around 8.4 ± 0.1 mL, and out of a total possible volume of 120 mL, an average FE of 7%. The amount of H_2 produced was on the other hand much less consistent, at 63.4 ± 19.6 mL, for an average FE of 53%. While the overall profile of product formation was largely similar between experiments, the maximum production rate varied considerably due to the difference in H_2 produced. The adjusted current density based on the observed yields would instead be 40.2 mA mg^{-1}. The amount of formate produced was consistent, accounting for about 1.2% of the FE across the set.

5.3.8 Kinetic Considerations

The voltage profile during the discharge should remain largely similar regardless of concentration, as it should be controlled by the ratio of Cr(II)/Cr(III) rather than the total amount. Depending on what is limiting the reaction rates, or 'current', changing the concentration could have different effects. If active sites remain the limiting factor, then production rate will not increase with concentration, however if charge delivery was the limiting factor, then it will increase. Of these scenarios, different effects on product selectivity may also be observed. If active sites were the limit and the 'current' does not change with concentration, then it would be unlikely product selectivity would change. If on the other hand charge delivery was limiting, even if only up to a point, and because multiple competing products are observed, then increasing concentration will alter the reaction dynamics in such a way that changes the relative rates of the competing reactions. As a considerable difference in selectivity was observed when increasing from 0.1 to 0.5 M mediator, this is likely to be the case.

The only feasible limits to the HER, because water is the solvent, are active sites and rate of charge delivery. However, the CO_2R is also limited by the availability of CO_2 at the catalyst surface. From the limited exploration presented within this work, it is clear that the decoupled system is still severely limited by the transport of CO_2. The high selectivity observed in conventional H-cell electrolysis could be due in part to the very low number of active sites and thus low current, even when using nanoparticle

catalysts. They are arranged on a 2-dimensional surface and usually require a binder, meaning only a small number of the active sites will be exposed to the electrolyte. In this conventional system, charge delivery is effectively not limited (small effects from resistance are expected but can be compensated). In the decoupled system, it is likely the amount of exposed active sites is magnitudes higher, so with active sites no longer the limit, the product ratio is controlled by the transport of charge via the mediator and CO_2.

5.3.9 Comparison to Conventional Systems

A brief reproduction of the conventional H-cell electrolysis with continuous CO_2 flow for same catalyst material was performed for comparison with the previously reported performance.[5] Controlled potential bulk electrolysis was performed at −0.7 V vs RHE, the approximate operating potential of the redox mediator, for a duration of 30 minutes. The selectivity for CO averaged 94% across the triplicate set, however the current density was just 3.2 mA cm^{-2}. This is compared to the previously reported value of 98.6 mA cm^{-2}, the only difference being the use of a glassy carbon plate instead of the carbon paper used by the original authors.

The ‘current density’ observed in the decoupled system was an order of magnitude higher that what was observed when the same material was used in a conventional H-cell, however this came at the cost of selectivity. As catalyst density was 1 mg cm^{-2} in the conventional testing, the current density mg^{-1} used in the decoupled system is considered a fair comparison to the current density cm^{-2} traditionally reported. While still short of the 200 $mAcm^{-2}$ benchmark of the state-of-the-art GDE systems, this initial exploration leaves considerable room for optimisation which may allow the decoupled system to compete favourably with conventional systems, especially considering the much more relaxed constraints on reactor design without the need for conventional membrane electrode assemblies, and may improve the limited carbon conversion efficiency reported in typical GDE systems.

5.3.10 CO vs Syngas as a Product

As a CO_2R product, CO would primarily be considered as an intermediate in the production of a wide range of chemicals by reaction alongside H_2.[14,15] For this reason, the direct production of syngas in not necessarily a concern when comparing to systems that produce almost exclusively CO. Depending on the ratio of H_2/CO, the syngas can be used for a wide range of reaction including the synthesis of methanol and ethanol, as well as the aforementioned Fischer-Tropsch process. Indeed, the only drawback is that direct water splitting can be achieved at much lower overpotentials

than those that are needed to produce CO, which would lower the energy efficiency compared to producing syngas by mixing separately produced H_2 and CO from single product processes.

5.4 Conclusion

Overall, the concept of $DECO_2R$ reported in Chapter 4 was successfully extended to the production of CO. The use of PVA as a capping agent for gold nanoparticles proved highly effective in boosting selectivity towards CO at the modest reduction potential provided by the Cr PDTA mediator. By varying the amount of PVA, a range of CO/H_2 ratios were obtained. The highest faradaic yields observed for $DECO_2R$ approaching 90% indicated that the poor faradic yields reported in Chapter 4 are not an inherent issue with the decoupled process. A brief exploration into scaling up the decoupled process by increasing mediator concentration found that current densities approaching state of the art systems can be realised, however the delivery of CO_2 still appears to be the limiting factor, with higher mediator concentration resulting in a lower selectivity towards CO. Regardless, as a first example of $DECO_2R$ as an alternative to conventional electrolysis, the work herein has demonstrated considerable promise.

5.5 References

1 S. Zhao, R. Jin and R. Jin, *ACS Energy Lett.*, 2018, **3**, 452–462.

2 F. Y. Gao, R. C. Bao, M. R. Gao and S. H. Yu, *J. Mater. Chem. A*, 2020, **8**, 15458–15478.

3 J. T. Feaster, C. Shi, E. R. Cave, T. Hatsukade, D. N. Abram, K. P. Kuhl, C. Hahn, J. K. Nørskov and T. F. Jaramillo, *ACS Catal.*, 2017, **7**, 4822–4827.

4 A. Bagger, W. Ju, A. S. Varela, P. Strasser and J. Rossmeisl, *ChemPhysChem*, 2017, **18**, 3266–3273.

5 L. Ma, W. Hu, Q. Pan, L. Zou, Z. Zou, K. Wen and H. Yang, *J. CO2 Util.*, 2019, **34**, 108–114.

6 H. E. Lee, K. D. Yang, S. M. Yoon, H. Y. Ahn, Y. Y. Lee, H. Chang, D. H. Jeong, Y. S. Lee, M. Y. Kim and K. T. Nam, *ACS Nano*, 2015, **9**, 8384–8393.

7 Z. Zhuang, Y. Zhang, L. Hu, H. Ying and W. Han, *Chem. - An Asian J.*, 2020, **15**, 2153–2159.

8 M. Miola, X. M. Hu, R. Brandiele, E. T. Bjerglund, D. K. Grønseth, C. Durante, S. U. Pedersen, N. Lock, T. Skrydstrup and K. Daasbjerg, *J. CO2 Util.*, 2018, **28**, 50–58.

9 H. Rabiee, L. Ge, X. Zhang, S. Hu, M. Li and Z. Yuan, *Energy Environ. Sci.*, 2021, **14**, 1959–2008.

10 A. Primo, A. Corma and H. García, *Phys. Chem. Chem. Phys.*, 2011, **13**, 886–910.

11 P. Ding, H. An, P. Zellner, T. Guan, J. Gao, P. Müller-Buschbaum, B. M. Weckhuysen, W. van der Stam and I. D. Sharp, *ACS Catal.*, 2023, **13**, 5336–5347.

12 Y. Chae, H. Kim, D. K. Lee, U. Lee and D. H. Won, *Nano Energy*, 2024, **130**, 110134.

13 J. H. Lee, S. Kattel, Z. Xie, B. M. Tackett, J. Wang, C. J. Liu and J. G. Chen, *Adv. Funct. Mater.*, DOI:10.1002/adfm.201804762.

14 S. Hernández, M. A. Farkhondehfal, F. Sastre, M. Makkee, G. Saracco and N. Russo, *Green Chem.*, 2017, **19**, 2326–2346.

15 S. Lu, Y. Shi, N. Meng, S. Lu, Y. Yu and B. Zhang, *Cell Reports Phys. Sci.*, 2020, **1**, 100237.

Chapter 6: Nickel Cyclam as a Homogenous Catalyst for Highly Selective $DECO_2R$

6.1 Introduction

Until this point, heterogeneous catalysis had been considered as the superior choice for $DECO_2R$, primarily because there would be no way to separate the catalyst from the mediator or from the electrodes if it was dissolved in the electrolyte. However, molecular catalysts are often highly selective due to the high degree of control they have over the reduction mechanism. The majority of molecular catalyst systems are reported under non-aqueous conditions, as they are often insoluble or unstable in water, however some aqueous examples exist.

Again, simplicity was desired such that the catalyst could be low cost and easily manufactured at scale. Complexes of nickel and 1,4,8,11-tetraazacyclotetradecane (cyclam) and its derivatives are often reported to catalyse CO_2 reduction with high selectivity and minimal HER. The reaction has been reported in many electrolytes including DMF,[1] MeCN[2] and water.[3] Selectivity is typically towards CO as the only major product, however formate is also observed in some instances.[1] H_2 is also a possible product, although it is usually only observed in small amounts. Indeed, a rigorous computational study into the mechanism of ECO_2R by nickel cyclam reported that CO is by far the more energetically favourable product.[4]

The heterogeneous catalysts tested thus far for $DECO_2R$ tended to display either poor faradaic efficiency or poor product selectivity towards CO_2R. The high selectivity of homogenous catalysts may offer an approach to DECO2R that allows for much higher selectivity than has currently been achieved.

6.2 Experimental

6.2.1 Chemicals

Nickel chloride hexahydrate (98%), potassium chloride (99.5%), potassium hydrogen carbonate (99.7%), ethanol (absolute) and diethyl ether (99%) were purchased from Thermo Fisher Scientific (Alfa Aesar, Acros Organics). 1,4,8,11-tetraazacyclotetradecane (cyclam, 98%) was purchased from Merck (Sigma Aldrich). CO_2 gas was purchased from BOC ltd.

6.2.2 Synthesis

Ni(cyclam)Cl_2 was synthesised by a rapid reaction of the ligand with nickel chloride. $NiCl_2$•$6H_2O$ (1.16 g) was dissolved in ethanol (80 mL) heated to 50°C. To this, cyclam (1.0 g) was added resulting in a rapid colour charge from green to pale purple. Once cooled, diethyl ether (20 mL) was added resulting in immediate precipitation of a pale purple solid, which was collected by filtration and dried under vacuum for a quantitative yield. Successful synthesis was confirmed by comparable cyclic voltammetry to that previously reported. Elemental analysis confirms an expected molecular formula $Ni(C_{10}H_{24}H_4)Cl_2$ of an anhydrous precipitate (expected 17.0% N, 36.4% C, 7.33% H, 0% S; measured 15.9% N, 36.3 % C, 7.75% H, 0.58% S) based primarily on excellent carbon fitting.

Cr PDTA was prepared as described in the preceding chapters.

6.3 Results and Discussion

6.3.1 Nickel Cyclam Electrochemistry

The electrochemical characteristics of nickel cyclam are well reported. Under inert conditions, two reversible redox couples are observed, Ni(III)/Ni(II) at 0.81 V vs SHE and Ni(II)/Ni(I) at −1.23 V vs SHE. The Ni(II)/Ni(I) couple is usually not observed as being reversible under aqueous conditions. Upon saturation with CO_2 however, a large increase in current is observed, which is indicative of a catalytic process as explained in Chapter 3. This wave occurs at roughly the same potential as the Cr(III)/Cr(II) couple in the Cr PDTA mediator used for $DECO_2R$ throughout this work. This excellent potential overlap suggests that the two complexes could be paired together for homogeneous co-catalysis as described in the introduction. Cyclic voltammetry of a electrolyte containing both Cr PDTA and Ni cyclam gave no clear indiaction of a cocatalytic process due to the poor reversibiltiy of the Cr PDTA voltammetry on glassy carbon.

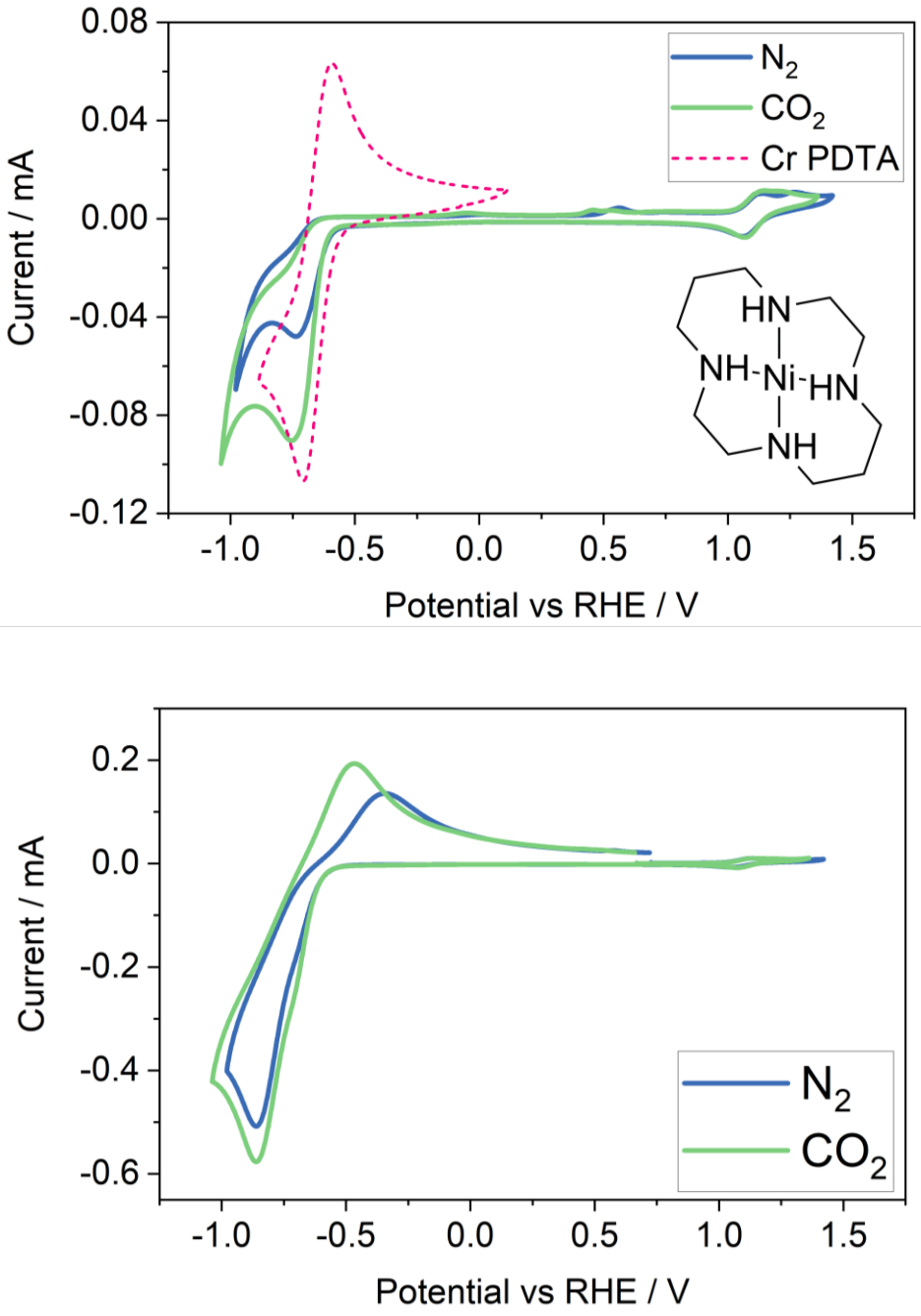

Figure 6.1 *(top) Cyclic voltammetry of 1 mM Ni(cyclam)Cl_2 in 1 M $KHCO_3$ under N_2 (blue) and CO_2 (green) atmospheres, using a glassy carbon working electrode at a scan rate of 100 mVs^{-1}. Potential has been referenced against RHE using pH value of 8.5 for the N_2 saturated electrolyte and 7.5 for the CO_2 saturated electrolyte. Cyclic voltammetry of 10 mM Cr PDTA (dashed pink) is overlayed to show the overlap in potential of the two species. The structure of Ni cyclam is inset. (bottom) Cyclic voltammetry of 0.9 mM Ni(cyclam)Cl_2 and 45 mM Cr PDTA in 1 M $KHCO_3$ under N_2 (blue) and CO_2 (green) atmospheres, using a glassy carbon working electrode at a scan rate of 100 mVs^{-1}. Potential has been refenced against RHE using pH value of 8.5 for the N_2 saturated electrolyte and 7.5 for the CO_2 saturated electrolyte.*

6.3.2 DECO_2R with Cr PDTA

Ni cyclam was tested as a catalyst for DECO_2R using Cr PDTA as a redox mediator. A 10 mL aliquot of 20 mM charged Cr PDTA was added to a Schlenk flask containing 10 mL of 2 mM Ni cyclam for a total of 20 mL of electrolyte containing 10 mM Cr PDTA mediator and 1 mM Ni cyclam catalyst. This provides enough electrons for 5 turnovers of the catalyst assuming only two-electron products.

The composition of the supporting electrolyte was varied, maintaining 1 M [K^+] but changing the counter ion between Cl^- and HCO_3^-. This had considerable effect on both the overall faradaic efficiency of the reaction and the individual product selectivity. The catalyst was most selective towards CO (77%) when 1 M $KHCO_3$ was used as the supporting electrolyte, however a significant portion of HCOO(H) was still produced, more than was expected based on the product selectivity reported in the existing literature. Replacing a portion of the HCO_3^- with Cl^- resulted in a significant improvement in faradaic efficiency, however the reaction became even less selective, producing even more HCOO(H). HER still constituted only a small portion of the faradic efficiency. Fully replacing the HCO_3^- with Cl^- saw even higher faradaic efficiency, with HCOO(H) becoming the major product and HER now contributing a considerable amount of the faradaic efficiency. Control reaction conditions indicated that no CO_2R products are observed when there is no source of CO_2, instead a moderate amount of HER occurs very slowly compared to the rate of discharge during CO_2R, around 10x slower.

As mentioned, formate was not expected to be observed as a product, certainly not as a major product. Further, HER was not expected to contribute such a large portion of the products under CO_2R conditions as it did in the 1 M KCl experiment. A report into the effects of using different buffers in the supporting electrolyte during CO_2R found that both activity and selectivity towards CO varied considerably between buffers.[5] The authors proposed that both the size and charge of the buffer species resulted in changes to the secondary coordination sphere of the complex, promoting or demoting the reaction pathways to the various products. This is evident the results presented herein, where using a bicarbonate buffered electrolyte promoted the selectivity of CO.

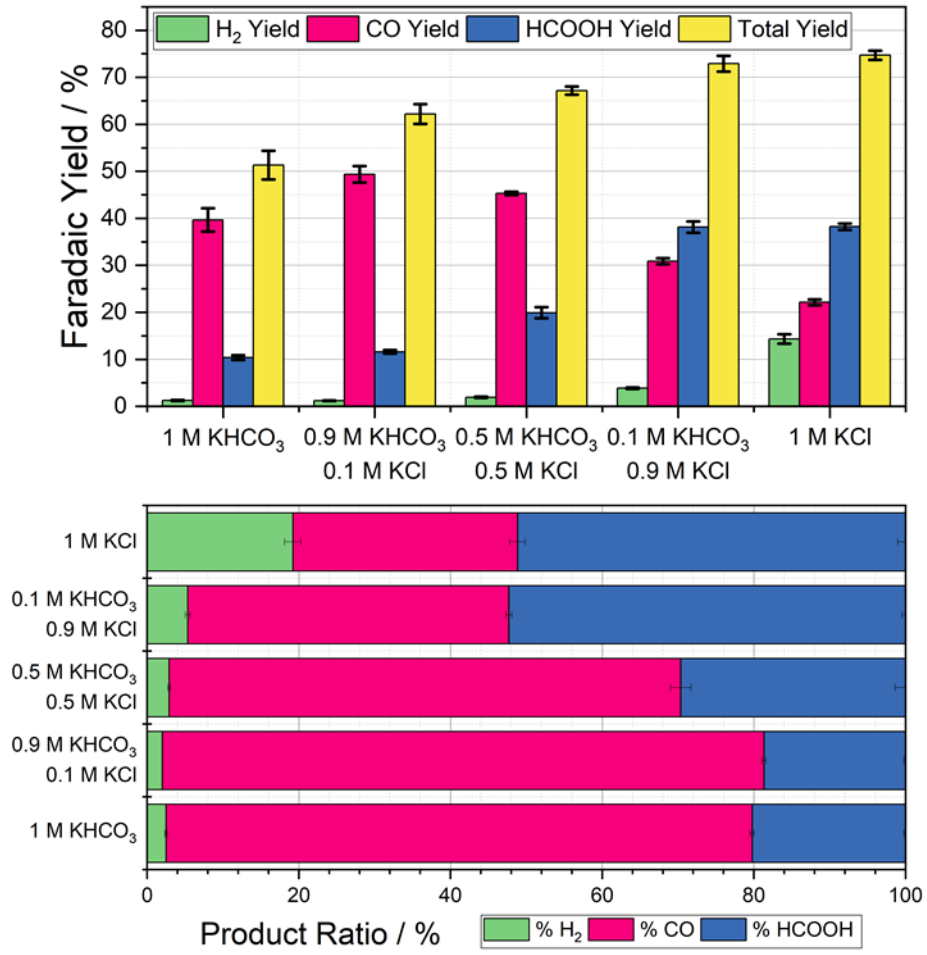

Figure 6.2 *(Top) Chart indicating the faradaic yield towards H_2 (green), CO (pink), HCOOH (blue,) and in total (yellow) for $DECO_2R$ using 1 mM Ni cyclam as a homogeneous catalyst and 10 mM Cr PDTA as a redox mediator with various combinations of $KHCO_3$ and KCl supporting electrolyte. (Bottom) Bar chart indicating the relative selectivity's towards H_2 (green), CO (pink), and HCOOH (blue) for the faradaic yields reported above.*

6.3.3 Flow Cell Test

A preliminary test employing Ni cyclam as the catalyst in the online analysis flow reactor was performed with increased mediator concentration. Using the same volumes as in the stationary experiment, but with 0.1 M Cr PDTA mediator to provide enough electrons for 50 catalyst turnovers. A continuous flow of CO_2 at 10 mL min^{-1} was bubbled through the reactor and into the injection loop of the GC, where the composition of the gas was measured every 20 minutes.

Figure 6.4 shows how the concentration of products in the outflowing gas evolved over time. The concentration of both CO and H_2 increased over the first hour of electrolysis,

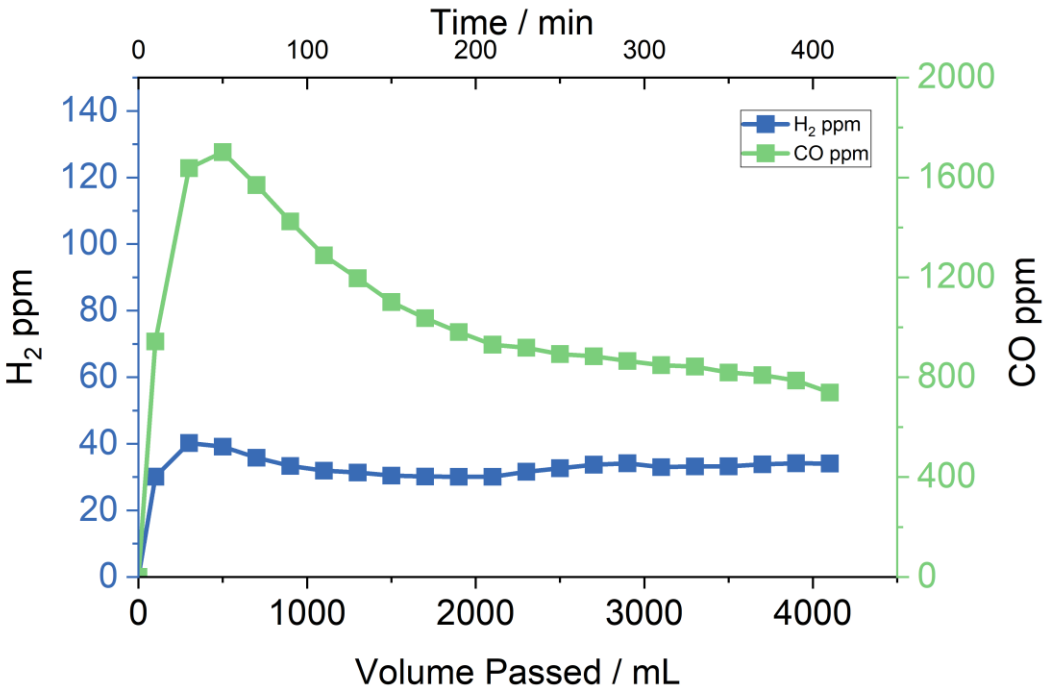

Figure 6.3 *Graph of the H_2 and CO concentration in the outflowing gas from the online reactor as a function of time and volume passed. The electrolyte consisted of 100 mM Cr PDTA and 1 mM Ni cyclam with 1 M $KHCO_3$.*

peaking at 1700 and 40 ppm respectively. H_2 concentration remained between 30 and 40 ppm for the following 6 hours of online analysis, while the CO concentration decayed to 1300 ppm after just one more hour, and to 740 ppm after the full 7 hours. The total amount of CO and H_2 produced over the 7 hours was 4.32 and 0.134 mL respectively. This can be approximated to a peak production rate of 17 µL of CO per minute, or 10.5 µL per minute for the full 7 hours. The final composition of the headspace of the RFB was found to contain an additional 1.04 and 0.0744 mL of CO and H_2 respectively, for total productions of 5.36 and 0.208 mL. This can be equated to faradaic yields of 22.3% and 0.87%, with a further 5.75% yield of HCOOH in the electrolyte. This gives selectivity's of 3%, 77%, and 20% for H_2, CO, and HCOOH, which matches well with the results obtained from the lower concentration batch reaction. The faradaic yield however was much poorer, at only 29% compared to the 51% observed at the lower concentration.

It has been suggested that the rate of catalytic turnover for Ni cyclam is limited by the formation of nickel carbonyl species that deactivate the catalyst.[6] The observed faradaic yield of just 29% may indicate that the catalyst is being deactivated before it can complete the 50 turnovers. There was no visible deterioration of the electrolyte, however voltammetry may indicate whether the Ni cyclam has been consumed during the reaction.

6.4 Conclusion

A brief exploration into using Ni cyclam as a homogeneous catalyst for $DECO_2R$ with Cr PDTA as a redox mediator has been demonstrated. The high selectivity of the molecular catalyst resulted in the highest selectivity towards ECO_2R reported in this work, with hydrogen evolution accounting for just 3-5% of the observed products when using $KHCO_3$ as the supporting electrolyte. Unfortunately, this was coupled with a relatively low faradaic efficiency ranging from 50-75% compared to the 85% achieved using Au/C nanoparticles in chapter 5. An interesting observation was found in that using KCl as the main supporting electrolyte resulted in a switch in selectivity from CO to HCOOH, which is not typically seen as a major product using Ni cyclam. Scaling up the reaction to increase the total charge passed saw a further decrease in the faradaic efficiency, suggesting that the catalyst may be deactivated by side reactions during $DECO_2R$.

Regardless, the work presented offers a novel contribution to the emerging field of redox mediated co-catalysis. Future work in determining the kinetics of the reaction and understanding the observed catalyst deactivation offer immediate opportunities in expanding on the brief exploration presented herein.

6.5 References

1 J.-P. Collin, A. Jouaiti and J.-P. Sauvge, *Inorg. Chem.*, 1988, **27**, 1986–1990.

2 J. D. Froehlich and C. P. Kubiak, *Inorg. Chem.*, 2012, **51**, 3932–3934.

3 M. Beley, J. P. Collin, R. Ruppert and J. P. Sauvage, *J. Chem. Soc. - Ser. Chem. Commun.*, 1984, **2**, 1315–1316.

4 J. Song, E. L. Klein, F. Neese and S. Ye, *Inorg. Chem.*, 2014, **53**, 7500–7507.

5 C. R. Schneider, L. C. Lewis and H. S. Shafaat, *Dalt. Trans.*, 2019, **48**, 15810–15821.

6 J. D. Froehlich and C. P. Kubiak, *J. Am. Chem. Soc.*, 2015, **137**, 3565–3573.

Chapter 7: Conclusions and Outlook

7.1 Conclusion

Chapter 3 reports a detailed study into the electrochemical performance of metal dithiolene complexes as homogeneous catalysts for ECO_2R. Metal dithiolene complexes are not commonly reported for catalysis despite being well known for having unusual redox activity owing to the non-innocent nature of the dithiolene ligands, as well as the frequency of metal sulphur cores as the active sites of many enzymes. In this work, it was found that the iron dithiolene complex of maleonitriledithiolate was catalytically active towards the reduction of CO_2 in the presence of a proton source such as water or TFE. Only the 2-electron reduction products CO and HCOOH were observed, with product selectivity showing a strong dependence on proton source. Only trace HCOOH produced when using water, meanwhile using TFE resulted in HCOOH as the major product. A significant amount of HER as a parasitic side reaction was observed with both proton sources.

Despite this, poor long-term stability and the unfavourable acetonitrile solvent made further work with the Fe mnt complex undesirable, and as such it was not used for $DECO_2R$.

Chapter 4 begins by describing the initial search for a suitable mediator for $DECO_2R$. After considering a range of battery negolytes that have previously been used to decouple HER, the chelated chromium species Cr PDTA was found to be uniquely promising due to its high solubility and stability in the pH range 7-9 most suitable for ECO_2R. This species displays a particularly negative redox event in near neutral aqueous media at −0.6 V vs RHE, providing nearly the maximum possible overpotential to enable $DECO_2R$ while still being practical to charge as an RFB negolyte. Using a range of basic metal catalysts to target different CO_2R products, it was found that HCOOH was the most accessible using bismuth powder as the electrocatalyst. The selectivity towards HCOOH was further enhanced using shape-controlled bismuth nanoparticles, resulting in a selectivity of over 85%.

Chapter 5 continues the exploration of $DECO_2R$ using Cr PDTA, this time extending product scope to CO. Using carbon supported gold nanoparticles capped with varying amounts of PVA, a range of syngas mixtures were produced from 4:1 to 1:2 H_2:CO. The concentration of the mediator was scaled up to allow for higher CO_2 conversion and continuous production using a CO_2 flow. This was coupled to online GC analysis such that the rate of product formation could be determined. From some preliminary

experiments, it was found that increasing the concentration had a negative effect on selectivity towards CO. Further, at the highest mediator concentration tested (0.5 M), the faradaic efficiency observed was much lower than when lower concentrations (0.1 M) were used.

Chapter 6 reports a brief exploration of using a Ni cyclam catalyst alongside the Cr PDTA mediator. Returning to the principles of homogeneous co-catalysis discussed in the introduction where mediators were used to boost the turnover of homogeneous catalysts, Cr PDTA was used to reduce the Ni cyclam in solution, where it then reacts with CO_2. Interestingly, both CO and HCOOH were observed as the major product depending on whether $KHCO_3$ or KCl was used as the primary supporting electrolyte. Ni cyclam is typically reported to favour CO, however it has also been reported to produce HCOOH in some cases. It is more commonly reported in non-aqueous electrolytes such as MeCN or DMF, and typically using a Hg working electrode, however unlike most homogeneous ECO_2R catalysts it is also soluble in water and remains selective. Indeed, using Ni cyclam resulted in the highest observed selectivity towards ECO_2R of any catalyst tested in this work, with H_2 making up less than 3-5% of the observed products under most conditions.

Overall, the work presented herein has successfully realised the concept of $DECO_2R$. Through the use of Cr PDTA as a reversible redox species with a particularly negative redox potential as a reducing agent, CO_2 was reduced to either formate or CO highly selectively on bismuth and gold catalysts respectively, albeit with competition from the HER. Unfortunately, no further reduced products such as CH_4 or C_2H_4 were observed, and the mediator proved incompatible with metallic copper typically used to target these products. Further work will be required to fully understand whether using the decoupled approach is truly beneficial for the kinetics of ECO_2R in the way envisioned. Developing practical and reproducible techniques to probe the kinetics of the reaction remains the primary challenge.

The decoupled approach offers an interesting alternative to conventional ECO_2R. This work has shown that a redox mediator can be used as a charge transport vector to decouple ECO_2R from the electrode surface. While only partially realised in this work, the approach allows for reactor design in which the catalyst does not need electrical continuity and its conductivity should not influence the potential at the electrode surface. While certain kinetic limitations at the electrode may be lessened by using a redox mediator, it will still introduce its own drawbacks. If electron transfer is not facile, the potential at the electrode surface may not reflect the potential of the mediator in

solution, and if charge cannot be delivered to the catalyst as quickly as it is being consumed, it will still limit the reaction more than the mass transport of CO_2, even though the mediator concentration may well be much higher than the CO_2 solubility limit.

Ultimately, the biggest drawback of $DECO_2R$ likely remains the limited potential it can provide. ECO_2R at practical current densities in conventional electrolysers is often achieved by applying a large cell voltage, sacrificing energy efficiency to somewhat overcome kinetic limitations. This approach cannot be used for $DECO_2R$. Applying a larger cell voltage during mediator charging will increase the rate at which it is charged, however this energy will be lost once the charge is transferred to the mediator. Regardless, the approach still allows for the charging step and the catalytic step to be optimised separately, such that the electrolytic cell can be optimised for mediator charging without regard for the mass transport of reactants and products, and the catalyst chamber can be optimised for the catalytic reaction without the need for electrical conductivity.

7.2 Considerations for Future Work

7.2.1 Kinetic studies

The next step in developing $DECO_2R$ is to explore the kinetics of the of the reaction to determine its limitations. Beyond measuring rate by continuous quantification of the products, the state of charge of the mediator can be used to measure the rate of electron transfer.

The first possible way to achieve this is through a continuous open circuit potential measurement between the potential of the solution at an inert electrode interface and a reference electrode as the decoupled reaction proceeds. The measured potential can be used to determine the state of charge of the mediator following the Nernst equation. At 50% state of charge, when the concentration of charged and discharged mediator is equal, the potential measure should be the standard potential determined in the prior voltammetry. As the difference in concentrations change in magnitude, the measured potential should change to reflect this. Practically speaking, as state of charge is increase from 1% to 9%, the measured potential should increase by 59.2 mV, then again from 9% to 50%, 50% to 91% and 91% to 99%. Overall, an observable potential window of about 240 mV should exist between almost full charge and discharge.

A second method of measuring state of charge, for a mediator such as Cr PDTA which exhibits considerable change in electronic absorbance between the charge and

discharged states, is UV/vis spectroscopy. Using the Beer-Lambert law, a calibration can be set up such that the state of charge can be determined from the measured absorbance. Because this response will be linear rather than the logarithmic nature of the Nernst potential, and would not be susceptible to a drifting reference potential, it offers a more robust response for mediator systems with appropriate optical properties. Indeed, both methods are frequently used in flow battery research.[1]

While state of charge measurements can offer useful information about the kinetics of the mediator, it is important to also consider the products of the reaction. Throughout the work, 100% faradaic efficiency was never observed, and as such determining reaction rate from state of charge alone will not accurately predict the rate of product formation. Coupling the decoupled experiment to online product quantification, as investigated briefly in Chapters 5 and 6, is crucial to understanding how the rate of product formation, along with product selectivity, changes over time. Further, comparing product selectivity with state of charge measurements may allow for a greater understanding on how the potential applied by the mediator on the catalyst influences product selectivity as the reaction proceeds.

7.2.2 Scaled up reactor

Alongside a greater understanding of the kinetics, it is also important to consider the practicality of scaling up the process. Within this work, the catalyst has always been deployed dispersed through the mediator, however it is envisioned that catalyst will be deployed in a fixed reactor as either part of continuous flow system wherein the mediator is charged in an electrolytic cell and discharged in the reactor simultaneously under a steady state regime, or as part of a charge-discharge sequence as in a typical RFB. Akin to flow batteries where power and capacity can be scaled independently, the same will be true of a decoupled reactor where the rate of mediator charging and product formation can be scaled independently by changing the size of the electrolytic cell and the reactor bed respectively. Achievable current density for the charging of the Cr PDTA mediator within an electrolytic cell has previously been reported as high as 100 mA cm^{-2} with minimal side reactions.[2]

Development of a suitable fixed bed reactor is the immediate next step in realising $DECO_2R$. The relaxed engineering constraints compared to conventional electrolytic cells have the potential to allow for a more flexible system. As mentioned, the primary benefit is no longer needing electrical continuity or conductivity. The only concerns are mass transport of mediator, reactant and product. As in conventional systems, CO_2 delivery is likely to remain the limiting factor in reactor design. Catalyst implementation

however is much less constrained. It was found that nanomaterial play a crucial role in enabling the level of selectivity towards CO_2R products required for a commercially relevant system. These could in theory be attached to any number of typical fixed bed support such as beads, gauzes or zeolites. Additionally, the reactor bed could be further functionalised to increase CO_2 concentration at catalyst interface such as through the use of the cyano-functionalised zirconium metal organic framework recently reported to trap CO_2 at the electrode surface.[3]

7.3 References

1 S. E. Waters, B. H. Robb, S. J. Scappaticci, J. D. Saraidaridis and M. P. Marshak, *Inorg. Chem.*, 2022, **61**, 8752–8759.

2 B. H. Robb, J. M. Farrell and M. P. Marshak, *Joule*, 2019, **3**, 2503–2512.

3 S. Mukhopadhyay, M. S. Naeem, G. Shiva Shanker, A. Ghatak, A. R. Kottaichamy, R. Shimoni, L. Avram, I. Liberman, R. Balilty, R. Ifraemov, I. Rozenberg, M. Shalom, N. López and I. Hod, *Nat. Commun.*, 2024, **15**, 1–14.